

Technische Universität München
Max-Planck-Institut für extraterrestrische Physik
Garching bei München

**High energy emission
of jet sources**

Eugenio Bottacini

Vollständiger Abdruck der von der Fakultät für Physik der Technischen Universität München zur Erlangung des akademischen Grades eines

Doktors der Naturwissenschaften

genehmigten Dissertation.

Vorsitzender: Univ.-Prof. Dr. A. J. Buras
Prüfer: 1. Priv.-Doz. Dr. J. Greiner
2. Univ.-Prof. Dr. F. von Feilitzsch

Die Dissertation wurde am 29.09.2008 bei der Technischen Universität München eingereicht und durch die Fakultät für Physik am 03.11.2008 angenommen.

to Marianna

Abstract

In this thesis I have conducted different multiwavelength campaigns on blazars triggered through AO proposals of the INTEGRAL mission and ToOs of other missions. Ground based observation facilities completed the campaigns. Through out the obtained strict simultaneous data I discuss, until now unobserved long-term spectral features, and new emission mechanism at work in blazar jets. I performed also an accurate background modeling of IBIS, the imager on board the INTEGRAL satellite, based on cross-correlation method. I obtain improved statistics on the images and an overall better sensitivity is achieved.

Zusammenfassung

In dieser Doktorarbeit habe ich an verschiedenen Blazaren mehrere Multifrequenz-Kampagnen durchgefuehrt, die durch INTEGRAL AO Proposals und weiteren ToOs von anderen Missionen ermoeeglicht wurden. Weitere Beobachtungen mit Bodenteleskopen haben die Kampagnen vervollständigt. Durch die strikt simultanen Daten eroertere ich, bis jetzt unbeobachtete langzeitige spektrale Eigenschaften, und neue Emissionsszenarien in Blazar Jets. Weiters habe ich ein genaues Hintergrundmodell, welches sich auf die Cross-Korrelations-Methode stuetzt, fuer IBIS, dem bildgebenden Instrument an Bord des Satelliten INTEGRAL, erstellt. Ich erreiche bessere statistische Resultate der Bilder und eine insgesamt bessere Sensitivitaet.

Table of Contents

1	High Energy Astrophysics	11
1.1	Introduction	11
1.2	A little history	12
1.3	Imaging techniques at high energies	15
1.3.1	X-ray telescopes.....	16
1.3.2	Focusing X-rays by reflection	16
1.3.3	Detecting the X-rays.....	17
1.3.4	Coded masks detectors.....	18
1.3.4.1	Coding phase.....	20
1.3.4.2	The point spread function	20
1.3.4.3	The autocorrelation function	21
1.3.4.4	Detection significance.....	22
1.3.5	Decoding techniques for coded mask telescopes.....	23
1.3.5.1	Cross correlation	23
1.3.5.2	Maximization methods	24
1.4	The INTEGRAL mission	25
1.4.1	SPI.....	26
1.4.2	IBIS	27
1.4.2.1	PICSIT	28
1.4.2.2	ISGRI	28
1.4.3	JEM-X	29
1.4.4	OMC	30
2	The Blazar AGN Subclass	31
2.1	Introduction	31
2.2	AGN Paradigm	33
2.2.1	Radio Galaxies vs Blazars	39

2.2.2	Observational evidences supporting the FR I/BL Lac and FR II /Quasar association	41
2.2.3	Doppler boosting	41
2.3	The Blazar sequence and its validity.....	42
2.3.1	The Blazar SED	42
2.3.2	The Blazar sequence	44
2.3.3	Validity of the Blazar sequence.....	45
2.4	The Extragalactic Background Light (EBL)	45
2.4.1	What is EBL?	45
2.4.2	Measuring the EBL	47
2.5	The state of the art and outlook	49
3	Software development and improvement of ibis standard code	51
3.1	Introduction	51
3.2	OSA standard software	54
3.2.1	Data flow	54
3.2.2	The data.....	54
3.2.3	The software.....	55
3.2.4	Image statistics.....	56
3.3	Software improvement.....	59
3.3.1	Data selection and screening.....	59
3.3.2	Shadowgram correction	60
4	INTEGRAL observation of gamma-ray Blazars	69
4.1	INTEGRAL OBSERVATIONS OF THE GAMMA-RAY BLAZAR 3C 279 DURING THE 'DEEP EXTRAGALACTIC SURVEY'	69
4.1.1	Introduction.....	69
4.1.2	Observations	71
4.1.3	Data analysis.....	72
4.1.3.1	High-energy observations	72

4.1.3.2	Optical observations.....	73
4.1.4	Results.....	73
4.1.4.1	Deep Extragalactic Survey.....	73
4.1.4.2	Combined results.....	75
4.1.5	Discussion.....	78
4.2	PKS 0537-286, the high red-shift FSRQ, giving new insights into the jet physics.....	81
4.2.1	Introduction.....	81
4.2.2	The source.....	83
4.2.3	Observations.....	83
4.2.3.1	X-ray observations.....	87
4.2.3.2	Optical to UV observations.....	88
4.2.4	Timing analysis.....	88
4.2.5	X-ray and hard X-ray spectra.....	91
4.2.5.1	Single spectra.....	91
4.2.5.2	Joint X-ray and hard X-ray spectra.....	92
4.2.6	Spectral energy distribution.....	94
4.2.6.1	Data.....	94
4.2.6.2	SED modeling.....	96
4.2.7	Discussion.....	98
4.2.7.1	Optical data.....	98
4.2.7.2	X-ray spectra.....	98
4.2.8	Conclusions.....	102
4.3	INTEGRAL observations of the blazar Mrk 421 in outburst.....	106
4.3.1	Introduction.....	106
4.3.2	Observations.....	108
4.3.2.1	INTEGRAL observations.....	109
4.3.2.2	VLBA observations.....	112

4.3.2.3	Observation with the Metsähovi radiotelescope.....	112
4.3.2.4	KVA observations.....	113
4.3.2.5	RXTE observations	114
4.3.2.6	Swift/XRT observations	114
4.3.2.7	Swift-BAT observations.....	115
4.3.2.8	Whipple obsrvations	115
4.3.3	Results of the timing analysis	116
4.3.4	The lightcurves.....	117
4.3.5	Rise-time analysis.....	118
4.3.6	Variability analysis.....	122
4.3.7	Time-lag analysis.....	124
4.3.8	Correlation analysis.....	126
4.4	Results of spectral analysis.....	127
4.4.1	Spectral fits.....	127
4.4.2	X-ray luminosity	131
4.4.3	Hardness ratios.....	131
4.4.4	Multiwavelenght spectrum νF_{ν}	136
4.4.5	Model fits.....	136
4.5	Discussion and conclusions	139
5	Conclusions	147
5.1	Conclusions and outlook	147
6	Bibliography	151

Chapter 1

1 HIGH ENERGY ASTROPHYSICS

1.1 Introduction

Already in the sixties Schmidt (Schmidt, 1963) observed and studied the object 3C 273 what then would be called Quasar (quasi-stellar) due to its star-like appearance and what then would become part of the most studied class of objects in the last decades, the Active Galactic Nuclei (AGN). A general accepted definition of AGN is that these are central regions or nuclei of galaxies where energetic phenomena take place which cannot be attributed clearly and directly to stars. The unequivocal evidence of their connection with extragalactic scales and cosmological distances (Schmidt, 1963) led AGN studies to become interdisciplinary and interesting for a variety of astronomical branches. I'll present here the results from observational facts and I'll stretch out the individual aspects approached during the jet like source studies presented in the main part of this

work. The treatment of today's theoretical and observational knowledge on AGN is not the aim of this chapter. I also would like to point out that only AGN were taken in account in the present thesis. Considering other jet-like sources like Gamma Ray Bursts (GRB) would certainly fill the pages of further thesis.

1.2 A little history

In order to detect X-rays of cosmic origin it is necessary to put the detectors above the atmosphere, which is opaque to that radiation. The penetrating power of the X photons increases with their energy. 3 keV photons can be detected only onboard stratospheric rockets above 80 km from ground while 30 keV photons penetrate the atmosphere to 35 km and can be detected with instruments flying on balloons.

An X-ray is an electromagnetic radiation quantum which is 1000 times more energetic compared to visible light. If X-ray photons originate, like most of the optical one in astronomy, in thermal processes, then the temperature of the object producing the X-rays must be thousands times the temperature producing the visible light. Looking for X-ray sources means looking for objects having temperature around million degrees, very different from most stellar objects.

The first technical breakthrough which permitted the exploration of the electromagnetic window observable only from space was the German military war surplus of World War II, the V-2 rocket. Using these stratospheric rockets Herbert Friedman of the Naval Research Laboratory in Washington DC and collaborators were able to detect X-rays from the Sun in 1949. The science payload of the rocket were Geiger counters. Based on these measurements and on the sensitivity of those instruments available at that time it was possible to deduce that if the celestial object emitted with the same power as the Sun than, considering the distances, it would be necessary to have detectors 100.000 times more sensitive than those available in the 1960's. So it is not surprising that only few felt encouraged to open this window even though the detection of the X-rays from the Sun.

Driven by theoretical speculations of Phillip Morrison at MIT (Massachusetts Institute of Technology) and Giuseppe Cocconi, which anticipated the possible

existence of X- and γ -ray sources (Morrison, 1958), (Cocconi, 1960) millions of times brighter than stars, a small group of scientists of the American Science and Engineering Corp. (AS&E), a private research firm in Cambridge, composed by Riccardo Giacconi, Herbert Gursky, Frank R. Paolini and Bruno B. Rossi at MIT projected an experiment for the observation of cosmic sources having the official aim to detect X-rays produced by the interaction of the cosmic particles transported by solar winds with the surface of the Moon. The possibility to get information from the surface of the moon tracked the attention and the experiment was financed due to the interest of the USA on the moon in those years. In October 1961 the experiment was launched but the ports of the rocket which protected the detectors did not open. This to mark the difficult conditions in which these pioneers of the high energy astrophysics carried out their research. The second attempt (Giacconi, Gursky, Paolini, & Rossi, 1962) was performed at White Sands in Mexico on June 18th, 1962. An Aerobee rocket brought three Geiger counters in orbit; two of them were working properly. No X-ray photons from the moon were detected but the historical discovery of the first cosmic X-ray source Sco X-1 and the cosmic diffuse X-ray was made. The first X-ray image of the Moon was obtained 28 years later on June 29th, 1990 by ROSAT X-ray telescope (Schmitt, 1991). Fluorescent X-rays produced on lunar surface originate from X-ray light emitted from the Sun's corona.

After this first discovery the importance of X-ray astronomy grew rapidly. In 1963 the X-ray emission of Crab Nebula, the remnant of a Supernova (SNR) exploded in 1054 and seen at Chinese court, was observed. On December 12th 1970, after a series of balloon and rocket flights which carried instruments, UHURU the first satellite dedicated entirely to the observation of the sky in X-ray band was launched from Kenya. The most urgent questions to be solved were: 1) What are the X-ray sources? 2) How many of them do exist? 3) What spacial distribution do they have? 4) How to compare the X-ray sky with the optical and radio counterpart? In order to answer these questions it was key to determine the precise position of the source all over the sky at a given flux limit (survey) and then identify them through cross-correlation with known optical and radio sources. Figure ... shows the survey maps done by the two X-ray missions UHURU and HEAO-1.

At even higher energies, in the γ -ray domain, the instruments used for photon detection are very different (see Chapter 1.5). They are very heavy and of big dimensions. The Earth's atmosphere is opaque to the γ -rays, which undergo Compton scattering processes (see Fig. 1.1). The detectors are carried at high

altitude by balloons or onboard satellites and suffer for the high background that contaminates the photon counts. Above 100 MeV, outside the atmosphere, bright sources exhibit a flux of just $10^{-6} \div 10^{-5}$ photons $\text{cm}^{-2} \text{s}^{-1}$ compared to several hundred photons $\text{cm}^{-2} \text{s}^{-1}$ in the X-ray domain.

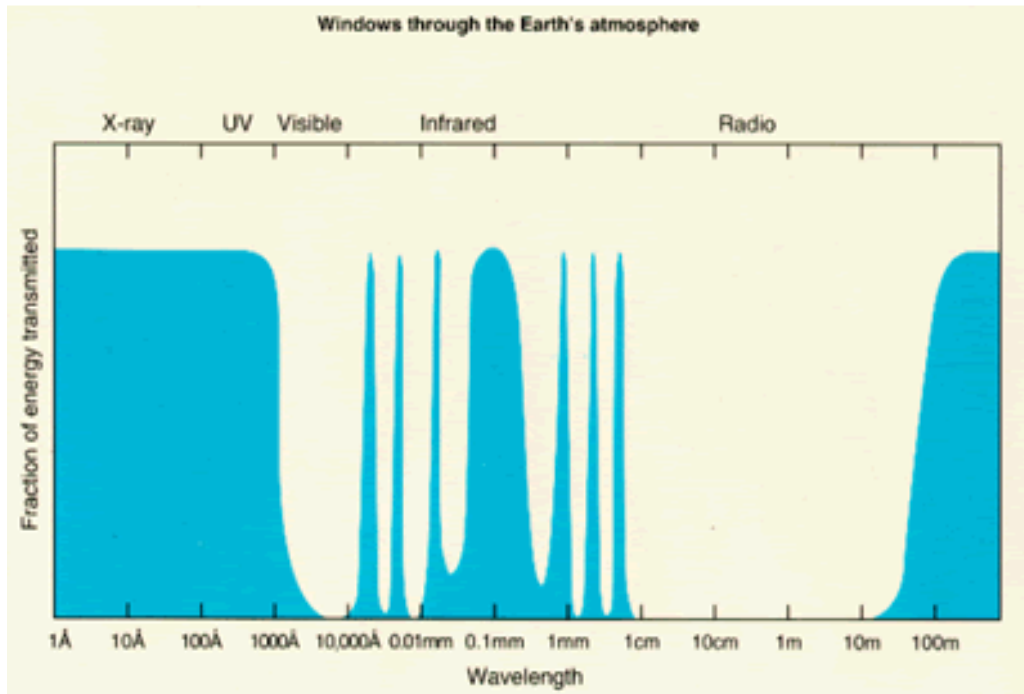


Figure 1.1: Absorption through the Earth's atmosphere.

Moreover, the γ -flux produced by the interacting cosmic rays with air atoms is 10^5 times higher than the source flux.

The instrument onboard the OSO-3 satellite, launched in March 1967, permitted to discover the galactic plane as an intense γ emitter. The flux could be spatially resolved by a scintillation counter flying with SAS-2. The direction of the photons could be determined with 1.5° accuracy. It was possible to constrain the flux from the galactic plane within a narrow area in latitude and a peak, the area of major flux, was centered in the galactic center. Also the pulsars in Crab and Vela region were found to be γ -sources. COS-B, also carrying a scintillation counter, was orbiting for seven years. Despite the low fluxes, the long integration

time on several sources permitted to outperform the previous observations. In addition to an accurate map of the flux distribution of the galactic plane, COS-B discovered 25 sources (see Fig. 1.xx). Some of them could be identified with known sources. One was found to be 3C 273. In 1991 the Compton Gamma Ray Observatory (CGRO) was launched. The satellite was orbiting until June 4th, 2000 and observed the Universe in the 30 keV - 30 GeV band. It was possible to map the Milky Way using the ^{26}Al γ -ray line and to find the isotropic distribution of the GRBs. One of the science highlights was the discovery of the blazar AGN subclass as a primary source of the highest cosmic γ -rays by EGRET. With its four instruments allowing simultaneous observations in optical, soft- and hard X-rays and γ rays, INTEGRAL (INTErnational Gamma Ray Astrophysics Laboratory) is contributing to the understanding of the emission processes of these type of objects. In addition to the point source studies, the mission addresses the distribution of heavy elements (^{26}Al , ^{60}Fe) in our Galaxy and the regions where positrons and electrons annihilate. Also AGILE, an Italian mission launched in April 2007, focuses on blazars. Thanks to its sensitivity of $4 \cdot 10^{-9}$ ph cm⁻² s⁻¹ above 400 MeV for one year of observation the GLAST-LAT should detect more than thousand blazars. Such a large blazar sample will enable detailed populations studies. The LAT large field of view (2.4 sr) together with the scanning observing mode will provide a uniform exposure of the sky, providing a constant monitoring of the source population and allowing flares alerts.

1.3 Imaging techniques at high energies

This section describes briefly the main elements important for the imaging techniques at high energies. The overlap between X-rays and γ -rays domain is somehow wide. Usually the range from a few tens to a few hundreds of keV suffers from having no clear definition. This is the domain where the coded mask imaging technique rules over the focusing one.

INTEGRAL, the international γ -ray mission described in section 1.4, is carrying three instruments using coded mask imaging techniques. We therefore will focus on these instruments.

1.3.1 X-ray telescopes

Photoelectric absorption is the effect chosen in order to detect X-rays. The incident photon deposits its energy on a precise location on the detector. This event is encoded by the electronics tagging the deposited energy, location on the detector and time giving rise to the following analysis possibilities respectively that are spectroscopy, imaging, lightcurve studies (also polarization).

The first step in the X-ray sky imaging was done with collimators which restrict the field of view of the detector to a small portion of the sky by blocking out the radiation from unwanted directions. Nowadays the focusing optics are used for X-rays imaging techniques. In this case the photons are focused on a small area on the detector plane, thus background is downscaled by many orders of magnitude. Basically the source to be observed is limited only by the photons emitted by the source itself. Due to the focusing capabilities, detectors such as CCDs or calorimeters are used which enhance the overall performances.

1.3.2 Focusing X-rays by reflection

High energy photons at X-ray wavelength are effectively absorbed by mirror surfaces. Metal surfaces are capable of reflecting these photons if very small reflection angles (a few degrees or less) are used. Telescope designs of this type are called grazing incidence telescopes, and they have been used in astronomy starting from 1970's. Total external reflection occurs, away from any absorption edges, up to critical angle given by:

$$\theta_c = \sqrt{4\pi N_e r_0 \lambda^2}$$

where N_e is electron density of reflecting material, λ is wavelength of X-rays and r_0 is classical radius of electron (Aschenbach, 1985). The grazing angle is directly proportional to wavelength (thus inversely to energy of X-rays) and to the electron density, which is proportional approximately to the atomic number of the surface material.

Wolter type 1 mirror systems use reflections from two surfaces. The first is a parabolic mirror concentrating off-axis photons, while the second one brings them to the focal plane being a hyperbolic mirror (see figure 1.2). Several pairs of

parabolic and hyperbolic mirrors can be nested to increase the collecting area and thus the sensitivity. This technique reaches good angular resolution, but a narrow energy range (e.g. Chandra: 0.5'' angular resolution and 0.1 - 10 keV energy range). The grazing angle limits the field of view to approximately 1° . This can be enlarged by the usage of a special configuration of the mirrors, named Lobster-eye (Angel, 1979).

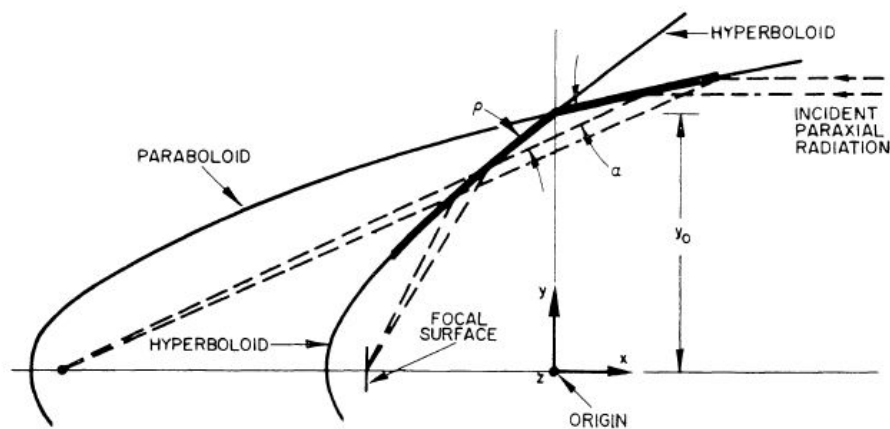


Figure 1.2: Schematic cross-section of Wolter type 1 mirror system hosting a hyperboloid and paraboloid mirrors. Adapted from (Giacconi, R.; et al., 1969).

1.3.3 Detecting the X-rays

By interacting with an absorbing material X-rays liberate charges which carry the information of the absorbed photon. In calorimeter detectors, the absorbed radiation causes a temperature gradient which is converted into electrical signal by a thermometer. Scintillator (like the detectors used for PICsIT, see section 1.4.2.1) instead convert the absorbed photon energy into light that is measured by a photodiode. In some detectors the charged particles produced by the incident radiation are collected directly in order to generate an electrical signal at the read output of the detector. This signal is amplified and processed by the front-

end electronics in order to obtain the information about energy, incident direction and arrival time.

Most X-ray detectors use CCDs based on semiconductors. These materials produce very efficiently the charge carriers due to photoelectric absorption when exposed to X-ray radiation. The charges are stored in capacitors. During readout the charges are moved to other capacitors and processed. At this point the detector is ready to store another set of charges generated by incident photons.

1.3.4 Coded masks detectors

When, due to intervening limits of the reflecting materials, the high energy photons cannot be focused anymore, the coded mask instruments take over. This is actually the energy range starting from 80 keV.

Imaging the sky above these energies is not any more a biunivocal relation between direction of incident photon and position of the detection in the focal plane, but it requires several steps. First the direction of the incoming photons is encoded before detection then the encoded observation has to be decoded in order to reconstruct the sky image. These two-step imaging methods are referred to as multiplexing techniques. Multiplexing techniques can be temporal or spatial (Caroli, E.; et al., 1987). As an example for the former case we can take in account a collimator moving across the sky containing an X-ray source. The count-rate of photons is a function of time. The position of the source along the scanning direction is given by the position of the maximum of the function, while the flux is given by the function's height. Spatial multiplexing detectors are referred to as coded mask telescopes. These instruments make use of a coded aperture (plate of transparent and opaque elements to photons within a certain energy range) that modulates the incident radiation from the sky (coding phase). The position sensitive detector (divided physically or logically into pixels) on the bottom of the telescope records the modulated signal. The shadow pattern of the mask, cast onto the detector from an X-ray source in the sky, should be linearly independent from the shadow cast by a source from any other direction. This means that the shadow pattern from an incident direction must be unique. As shown in figure 1.3 left panel, the incident direction of the photons from a source can be reconstructed later.

A basic parameter determining the telescope's performance is the field of view (FOV). As figure 1.3 right panel illustrates, this parameter depends on the linear

size of the coded mask and detector and on the distance between these two (inverse proportional). Therefore we have the fully coded field of view (FCFOV) where the complete source radiation recorded on the detector plane is modulated by the mask (100% coded). While in the case of the partially coded field of view (PCFOV) only a part of the source's radiation is modulated on the recording detector. Depending on the coding fraction usually the PCFOV is indicated at a certain % level.

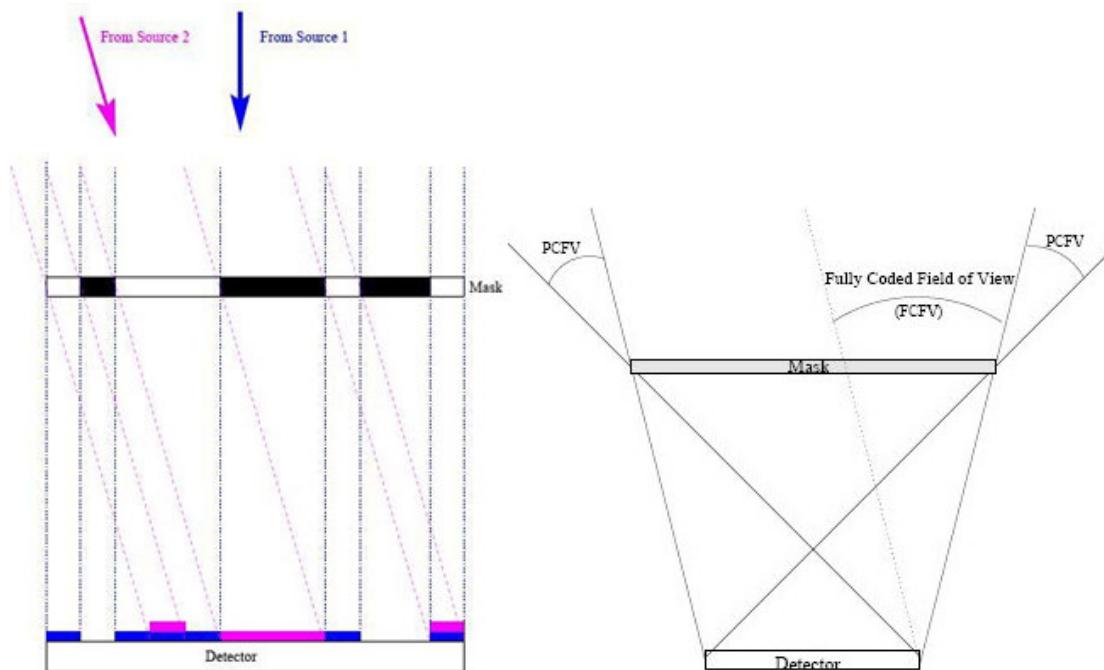


Figure 1.3: Left panel: Working principle of coded mask telescopes. The shadow generated by two sources at infinite distance are shown. One is on-axis and the other is at the edge of the FOV. Right panel: The concept of fully coded and partially coded field of view is shown. It is evident that these parameters depend on the detector and mask linear sizes and the distance between them.

Each detector pixel records the sum of the signals from different combinations of directions or 'sky pixels' (and background).

1.3.4.1 Coding phase

In coded mask instruments the detector plane image is not a replication of the object as in conventional optical systems. The sky image is encoded through the coded mask. Representing the mask with an array M of 1 (transparent elements) and 0 (opaque elements), the detector array D (information recorded in the detector) is given (Fenimore & Cannon, 1978) by convolving the sky image S by M plus the unmodulated background term of the array B :

$$D = M * S + B.$$

Based on this equation, an array G must be found such that the recorded information can be deconvolved (recovered):

$$S' = G * D = G * (M * S) + G * B.$$

It is evident that the goodness of the image reconstruction is dependent of the coded mask (M), the decoding function (G) and the background noise of the detector (B). Ideally, for a perfect imaging system $S = S'$, and the final image is identical to the initial object. To get this G the deconvolution array must be such that $G * M = \delta$ function and simultaneously $G * B$ as close as possible to 0. If both conditions are met the system is called a perfect imaging system. If this is not the case, then additional noise spikes, known as side-lobes, are present in the deconvolved image. Both conditions cannot be totally met (Skinner & Ponman, 1994). Moreover it is fundamental that, apart the unique shadow pattern for each incident direction, the similarities between the patterns should be as poor as possible. This is in order to be able to distinguish between the incident directions without ambiguities.

1.3.4.2 The point spread function

The response to a point-like source (point spread function - PSF) of a coded mask telescope is the worst imaginable when compared to conventional imaging

systems. The PSF is not just blurring, but it fills the whole detector plane (see figure 1.4). This means that every point in the image is affected by the noise from the whole detector plane. This affects also the flux. The noise coming from each pixel contributes to the flux error of a source, since a single source illuminates the whole detector plane.

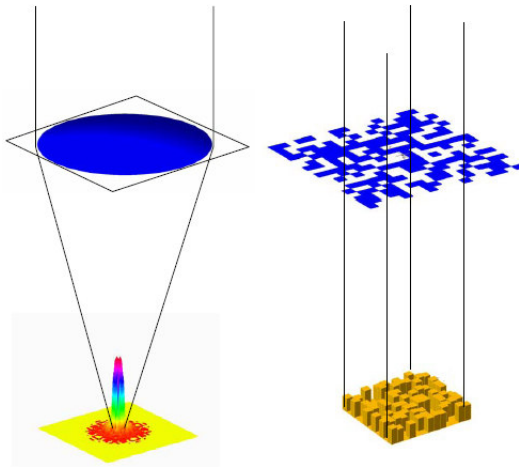


Figure 1.4: Comparison between a idealised focusing system with its PSF (left) and a coded mask imaging system (right) (Skinner, 2004). In the latter case, the projected shadow of one single point-like source supposed at infinite distance, is subject to the noise of each single pixel of the whole detector.

1.3.4.3 The autocorrelation function

For coded mask instruments the system PSF depends on the instrumental design and the decoding algorithm. On the other hand the autocorrelation function (ACF) is obtained by correlating the matrix defining the mask pattern with itself, and depends therefore only on the mask itself. This property is used in order to compare the imaging properties of different coded apertures. The ACF is computed starting only from the mask pattern. This is done by assuming the mask to be uniform (all opaque or all transparent) outside the coded field, or by assuming the mask pattern to be repetitive (cyclic ACF). In the case of mosaicked

mask pattern the latter is particularly useful. Assuming a $m \times n$ rectangular mask M the basic and cyclic ACFs can be derived as follows:

$$\text{ACF: } A_{i,j} = \sum_{k=1}^{m-(i-1)} \sum_{l=1}^{n-(j-1)} M_{k,l} M_{(i+k),(j+l)}$$

$$\text{cyclic ACF: } A_{i,j} = \sum_{k=1}^m \sum_{l=1}^n M_{k,l} M_{(i+k) \bmod m, (j+l) \bmod n}$$

For most mask patterns, the ACF side-lobes are not flat and thus high frequency noise is superimposed. By applying a balanced correlation (Fenimore & Cannon, 1978) the ACF can be flattened. The mask array M is multiplied not with M itself but with a modified M' :

$$\text{balanced ACF: } A_{i,j} = \sum_{k=1}^{m-(i-1)} \sum_{l=1}^{n-(j-1)} M_{k,l} M'_{(i+k),(j+l)}$$

$$\text{where: } M'_{i,j} = \begin{cases} 1 & \text{for } M_{i,j} = 1 \\ \frac{-\rho}{1-\rho} & \text{for } M_{i,j} = 0 \end{cases}$$

ρ being the open fraction of the mask.

The intrinsic noise of the coded mask, called the *coding noise*, is given by the ACF side-lobes. The mask must be designed to limit this effect.

1.3.4.4 Detection significance

The detection significance of a source is simply the ratio between source's signal and noise. It is the significance with which a source can be detected above

the background (usually 5σ). Assuming an ideal PSF (delta function), where ρ is the open fraction, S_1 is the considered source and ($S_2 \dots S_N$) are the intensities of the other sources in the FOV, B the sky background and b the detector background, the signal-to-noise ration is given (in 't Zand, 1994):

$$\frac{S}{N} = \frac{S_1}{\sqrt{\frac{S_1+b}{\rho} + \frac{B+\sum_{i \neq 1} S_i+b}{1-\rho}}}$$

1.3.5 Decoding techniques for coded mask telescopes

Coded mask telescopes encode the radiation from the sky. Decoding the recorded information is needed in order to reconstruct the sky image. The decoding techniques are applied to images for deconvolution.

1.3.5.1 Cross correlation

If switching to the matrix notation the equation in section 1.3.4.1 can be solved by finding a matrix $G = M^{-1}$ (which is the aperture itself), where the rows of M must be linearly independent in order that its inverse is not singular. If the entries in M^{-1} are small then the following conditions are approximately satisfied:

$$G * M = \delta \quad \text{and} \quad G * B \simeq 0$$

This condition can be met using the above exposed balanced ACF, being coincident with the PSF. G can be represented by a sliding template of the mask pattern. The number of counts per second recorded in the detector is function of the spatial coordinated of the incident photons (from the point-like source). The cross correlation of recorded data with the sliding template has a triangulare shape. The position of the maximum of the triangle is the position for which data pattern and template are in phase, and thus it provides the position of the source in the sky. As discussed in section 1.3.4.3, if the ACF (and therefore the PSF) does not have flat side-lobes, this will result in systematic errors referred to as coding noise.

1.3.5.2 Maximization methods

The cross correlation method takes in account only the effect of the mask in the signal modulation. A more complete way is to consider the following equation:

$$D_{k,l} = \sum_{i,j} S_{i,j} \varphi_{k,l}^{i,j} + B_{k,l}$$

where φ is a function giving the fraction of the flux coming from the sky pixel i,j seen by the detector k,l . It includes also factors that affect the signal such as transparency, detector efficiency, etc.

When cross correlation is not used, then iterative decoding methods are used to compute the source distribution on the sky. The maximization methods use the above described equation to estimate the sky vector S making use of iterative approximation in order to determine the solution most consistent with recorded data. The first iteration requires an input model of the sky distribution \hat{s}_0 folded through the instrumental response functions in order to model the expected detector count rates \hat{c}_0 . \hat{c}_0 would result from the model of the sky \hat{s}_0 . A new estimate of the sky model \hat{s}_1 is computed by the algorithm which compares the expected count rates \hat{c}_0 with the one measured C . Successive iterations lead these algorithms to a value of \hat{s}_i which yields to \hat{c}_i that is in good agreement with C . The convergence of the iterations is strongly dependent on the method used to evaluate the goodness of the fit between \hat{c}_i and C , and thus the evolution of the sky model from \hat{s}_i to \hat{s}_{i+1} .

The maximum likelihood (Dempster, A.P.; et al., 1977) method is used to compute the estimators iteratively. It looks for the sky model \hat{s} making the observed measurement C most likely. Therefore \hat{s} is the estimation that maximizes the likelihood. This method can be applied to Gaussian and Poisson statistic. Formally the solution of the maximum likelihood is the same as the one obtained by cross correlation in absence of noise.

The maximum entropy method looks for the most uniform sky map consistent with the recorded data. It is obtained by defining an entropy function and maximizing it. The uniform sky distribution is a priori information which is not evaluated in the maximum likelihood.

1.4 The INTEGRAL mission

INTEGRAL (INTErnational Gamma-Ray Astrophysics Laboratory) (Winkler, C.; Courvoisier, T.J.-L.; Di Cocco, G.; Gehrels, N.; et al., 2003) was selected by ESA (European Space Agency) as medium-size scientific mission of its program Horizon 2000. Mission participants are all member states of ESA plus the United States, Russia, Czech Republic and Poland. The mission operations centre responsible for satellite control is located at ESOC in Germany. The INTEGRAL Science Operations Centre (ISOC) at Noordwijk, the Netherlands, provides the observation plan, and Switzerland hosts the centre for the scientific data, the INTEGRAL Science Data Centre (ISDC). INTEGRAL was the first space observatory that can simultaneously observe objects in gamma rays, X-rays, and visible light. Its principal targets are violent explosions known as gamma-ray bursts, powerful phenomena such as supernova explosions, and regions in the Universe thought to contain black holes. The satellite was launched on October 17th, 2002 from Baikonur, Kazakhstan.

It carries four co-aligned scientific instruments. The two main experiments IBIS (Imager on-Board the INTEGRAL Satellite) and SPI (SPectrometer on INTEGRAL) are dedicated to observation in the hard X-ray and γ -ray ranges with fine spatial and spectroscopic resolutions. The main targets are point and diffuse γ -ray sources within our galaxy and extragalactic fields. Also regions where nucleosynthesis takes place are of interest. At soft X-rays the two X-ray monitors JEM-X (Joint European X-ray Monitor) 1 and 2 are complementary to the two previous instruments. OMC (Optical Monitoring Camera) is a small optical telescope with V-filter.

Data from all four instruments are processed simultaneously from most observations. These allow determining the morphology of the source. It is also essential to understand the flux variations over time of the source, in order to determine the underlying physical mechanism.

Two stations ensure the satellite follow-up: Redu in Belgium and Goldstone in California. Hence, the whole orbit is covered. The telemetry packets are then sent to the Mission Operation Centre (MOC) located in Darmstadt (Germany). The INTEGRAL ground segment is divided in two parts: the operation and the science. The INTEGRAL Science Operation Centre (ISOC) (located at ESTEC at the beginning and since 2005 at ESAC) is in charge to call for proposals and to provide an observation plan to the MOC. The INTEGRAL Science Data Centre (ISDC) (located at Versoix near Geneva) receives the telemetry data and processes them before

releasing the processed data to the community. An archive of all the data is maintained at ISDC. The ISDC also provides the Offline Science Analysis package that allows an interactive analysis of the INTEGRAL data. A Quick-Look Analysis (QLA) is also operated at ISDC that allows getting images per pointing of the X-ray sky approximately three hours after its observation. Therefore, unexpected interesting events can rapidly be checked and the community alerted.

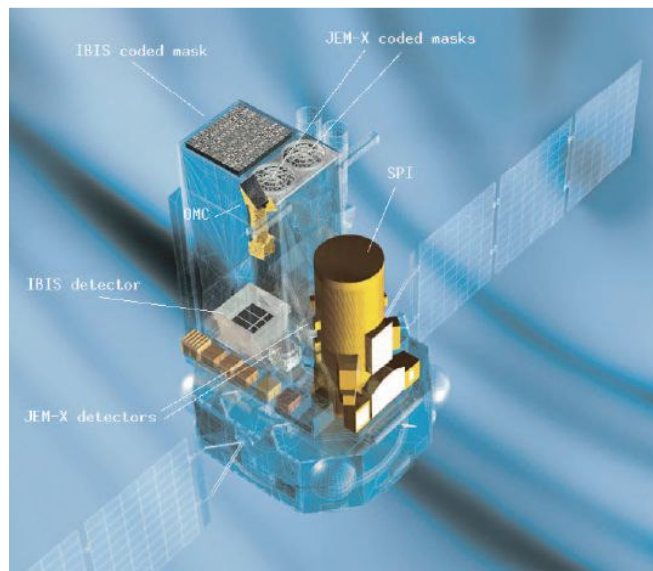


Figure 1.5: The INTEGRAL satellite and its instruments adapted from (Winkler, C.; Courvoisier, T.J.-L.; Di Cocco, G.; Gehrels, N.; et al., 2003).

1.4.1 SPI

The operative range of SPI (Vedrenne, G.; Roques, J.-P.; Schoenfelder, V.; et al., 2003) is between 20 keV and 8 MeV. It is the main instrument for high-resolution spectroscopy at hard X- and γ -ray energy. The main parts of the instruments are: a coded mask (see section 1.3) of tungsten elements, detector plane and a shielding system. Thus it also can provide low-angular resolution (2.5°) images. The detector is a hexagonal array of 19 high purity Germanium detectors. Two of them are permanently “dead”, thus the sensitivity is slightly reduced. Each 6-12 months annealing is needed to recuperate perfect crystal

status and to minimize the radiation damage on the detectors. An Anti-Coincidence Shielding (ACS) of Bismuth Germanate (BGO) defines the instrument Field-Of-View (FOV) by providing veto pulses for photons and particles coming from the sides. The ACS has a scientific impact as it is a detector for all γ -ray photons. Therefore it can detect all random GRB without any spatial information (Rau, A.; Kienlin, A. V.; et al., 2005).

1.4.2 IBIS

The hard X-ray and γ -ray imager IBIS (Ubertini, P.; Lebrun, F.; Di Cocco, G.; et al., 2003) is a coded mask telescope using 2 detector planes ISGRI (INTEGRAL Soft Gamma-Ray Imager) and PICsIT (Pixellated CsI Telescope). The mask is formed of the coded pattern (Tungsten elements) and the structure sustaining it. Its angular resolution is limited by the dimensions of the mask elements ($c = 11.2$ mm) and the distance between the detector plan and the mask ($h = 3133$ mm):

$$d\theta = \tan^{-1}(c/h) = 12'.$$

When decoding the sky this is used as point-spread function (PSF). Half of the mask is opaque to the radiation in the IBIS energy range. The basic mask pattern is cyclic replicated and is called MURA. Between the mask and the detectors, there is a collimator made of a passive material that blocks as much as possible of the high energy diffuse background emission. The collimator is opaque up to 200 keV. The FOV achieved for IBIS is of $29^\circ \times 29^\circ$ (at 0 intensity), with the FCFOV being $9^\circ \times 9^\circ$. Both detector planes are surrounded (bottom and 4 lateral sides) by an anti-coincidence system made of BGO crystals. It rejects those events detected by the instruments due to cosmic particles or local environment radiation.

The discrete-element double layer design of IBIS allows tracking the 3D path of photons interacting in both first in ISGRI due to Compton scattering and than in PICsIT where it is absorbed. The application of Compton reconstruction algorithms applied to IBIS is fully described in a very recent publication of Forot (Forot, M.; et al., 2007). This technique was applied to Crab pulsar and presented by the same author at the science workshop “Five years of INTEGRAL” in 2007 showing high-energy polarization to be fully consistent with the angle measured in the optical within 0.1 pc of the pulsar.

1.4.2.1 PICSIT

PICsIT (Labanti, C.; Di Cocco, G.; Ferro, G.; et al., 2003) works in the energy range from 200 keV to 10 MeV. It is made of 4069 CsI(Tl) scintillation crystals. These are grouped into 8 modules each one housing 16 x 32 detector elements. The modules are further divided into two electronically independent sub-modules. Once passed through ISGRI, the incident photon can be detected by PICsIT as single event or multiple events. In the former case the photon interacts with one CsI crystal which emits the scintillation light that is recorded at the photodiode. In the case that more detection units in one sub module are excited during one event, the energy of the photon is derived from the sum of the energies of all excited crystals. The photon will be spatially attributed to the pixel which detected the most energetic interaction.

Due to the high background level PICsIT works in histogram mode. This means that images and spectra are accumulated for about 30 minutes before down linking to ground. No time-tagging interval to the histogram is provided; therefore imaging has time resolution of 30 minutes. Spectra without imaging information are accumulated by the detector and transmitted with higher time resolution. Thus these spectra are useful only when contrite dominates over the background.

1.4.2.2 ISGRI

ISGRI (Lebrun, F.; Leray, J.P.; Lavocat, P.; et al., 2003) is made of 128 x 128 independent Cadmium-Telluride (CdTe) crystals being 4 x 4 x 2 mm³ in size. Its operative range is between 20 keV and 1 MeV and it is placed on the bottom of PICsIT. The layer is split into 8 electronically independent modules, each one housing 32 x 64 detector units. The normal ISGRI mode records each event tagging the pixel detector, energy deposit and event time (photon-by-photon). It works in single event mode: the photon is stopped in a single pixel of the ISGRI layer, giving rise to an electric pulse. In case of multiple detection units excitation within the same module the events are rejected. The excitation of the detection units in different modules are managed as independent single events. The energy deposit is determined by the amplitude of the pulse. Above 50 keV the energy deposit is calculated using the pulse rise time and the pulse height. The overall design of the instrument can be seen in figure 1.6.

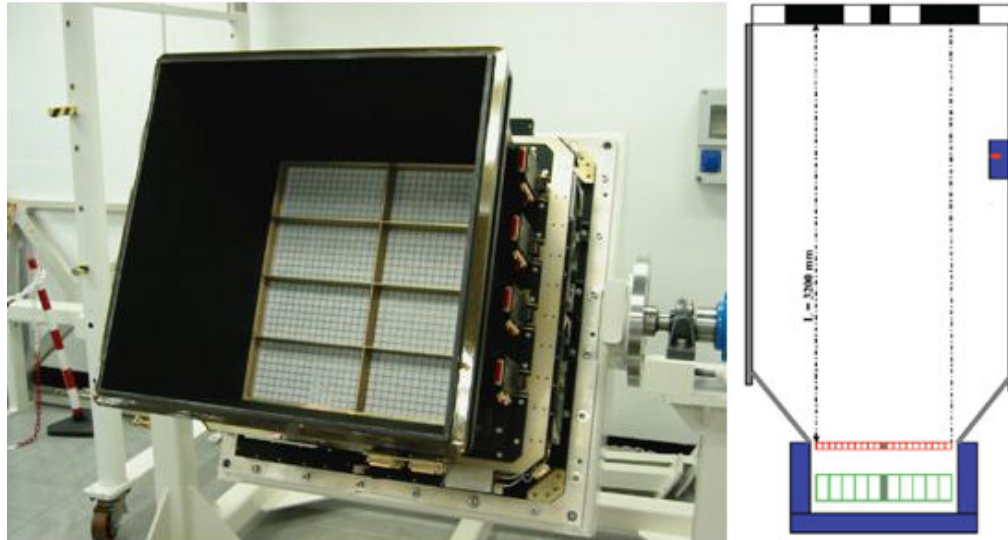


Figure 1.6: Left panel: IBIS in the Laben laboratories of Milan while being integrated. The 8 modules of the ISGRI detector can be seen. Right panel: in blue color the shielding system (16 BGO modules) for PICsIT (green) and ISGRI (red). The gray tube is the passive shielding (hooper tube). Between detector and coded mask the calibration unit (^{22}Na) is shown.

1.4.3 JEM-X

The operative energy range of JEM-X (Joint European X-ray Monitor) (Lund, N.; et al., 2003) is between 3 keV and 35 keV. Aim of the instrument is to complete the observations taken with the two main ones, described above, in order to cover the spectrum down to 3 keV. JEM-X has also imaging capabilities. This is possible because JEM-X consists of two identical coded mask telescopes co-aligned with the others. Both JEM-X units are made of: the coded mask placed on the top, the detector and the bottom electronics. Moreover the detectors consist of a gas chamber where incident photons are absorbed by photo-electric absorption and the resulting amplification is amplified towards the strip anodes using high voltages. A collimating structure connects detector and mask settling the FOV diameter to 13.2° and reducing the background. The detector - mask distance is 3400 mm and the cell size is of 3.3 mm resulting in an angular resolution of $3'$ (see equation above). Due to degradation of the anodes JEM-X2 is actually turned off.

1.4.4 OMC

The optical telescope OMC (Optical Monitoring Camera) (Mas-Hesse, J.M.; Gimenez, A.; et al., 2003) uses a large format CCD of 1024 x 1024 pixels resulting in a wide field of view of $5^\circ \times 5^\circ$. Also this instrument is co-aligned with the high-energy instruments. Telemetry restrictions allow only a small fraction of the data to be transmitted to the ground even though the large field of view. The refractive lenses and a Johnson *V* filter are the optical system. The limiting magnitude for OMC is 19 mag.

Chapter 2

2 THE BLAZAR AGN SUBCLASS

2.1 Introduction

Only a small fraction, about ~1%, of today's known galaxies shows phenomena which are referred to as activity. These are:

- compact core (less than 0.1 pc), brighter than that of normal galaxies (up to 10^{47} erg s⁻¹)
- continuum emission from central core component ranging from radio to X-rays and in some cases also to γ -rays
- emission lines arising from central regions by non-stellar processes
- highly variable radiation and/or emission lines
- non-thermal radiation originating in the center in form of jet

If one or more of these properties are shown then the galaxies are commonly referred to as Active Galactic Nuclei (AGN), indicating that the activity is confined or generated in their innermost central region.

The discovery of the Seyfert galaxies in 1943 (Seyfert, 1943) led to the studies of AGN. But the real AGN-story started in 1960 while trying to determine the angular size of the brightest objects of “The third Cambridge catalog” (3C) (Edge, 1959) using a 5m telescope. The emission lines in the spectra of some sources could not be identified. In the color U - B, B - V, diagram these sources occupied a region near to the white dwarfs indicating high temperatures on the surface. The general opinion was that these sources were stars in the Milky Way. This was based on the fact that they were star-like in aspect (the 5m telescope could not resolve), but also because photometry data of 3C 48 showed variability on timescales of the order of a day. It was deduced that the time necessary for the light to propagate through the region responsible for variability could at most be of the same order otherwise the variations would compensate themselves. Therefore the region could not be more extended than the distance of a light day, but obviously smaller. This conclusion enforced the hypothesis of a star object in the Galaxy. But in 1963, a crucial year for astronomy and cosmology, a further radio source namely 3C 273 was identified and its position was determined with an uncertainty of only 1”. This was possible due to Moon occultation of 3C 273. In fact the position of the moon is very well known and therefore it was possible to determine the position where the source was occulted and where it reappeared. Moreover two components of the source at a distance of 20” were found. Driven by the identification Schmidt decided to obtain an optical spectrum of the source. In addition he found a weak jet extending from the strong part of the source to the weaker one. The emission lines of the spectrum were not of easy interpretation. Therefore Schmidt decided to try to explain these features as due to the red shift despite the general accepted hypothesis of the galactic nature of the source. He immediately found that the lines could be interpreted as H-lines red shifted by 0.158 (Schmidt, 1963). This was the start-up of the Quasar-era which has developed to become one of the largest fields in astronomy. A systematic study of these objects gave significant contribution to the growth of AGN research. The investigation of their complexity of their build-up is possible only within different specialized subfields and their strong emission at almost all wavelengths makes them ideal targets for most ground- and space-based observations. The developments over several decades lead to the fascinating picture of a super-massive black hole, surrounded by an accretion disk, lying in center of the Galaxy and strong non-thermal jets extending over incredibly large

distances (10^{13} km) in some of them. For a more complete discussion of the AGN history I would like to refer the further interested reader to one of many excellent review articles (Shields, 1999).

2.2 AGN Paradigm

Leaving now the historical path several types of AGN are observationally identified and listed here below:

- QSO (Quasars radio loud/quiet): the name comes from their appearance: Quasi Stellar Objects. Most of QSOs emit radio waves and the discriminating principle between QSO radio-loud and radio-quiet was fixed conventionally at emission power $P_{5\text{GHz}} = 10^{24.7}$ W/Hz. A number of QSO radio-quiet show broad absorption lines in optical spectra. QSO radio-loud are per definition powerful radio emitters whose optical counterpart is dominated by a blue ($U-B < 0$) and bright nucleus. Nearly all of these radio-loud objects are X emitters at a few keV. Observed at radio wavelength with VLBI (Very Long Baseline Interferometry) techniques some of these sources show superluminal motions attributed, without violating the basics of relativity, to the presence of a jet.
- Sy 1 and 2 (Seyfert AGN): Seyfert AGN are divided in type 1 and 2 based on their emission line features. Both of them show radio power around $P_{5\text{GHz}} \sim 10^{20} \div 10^{23}$ W/Hz and their host galaxies are spiral in their morphology. H-lines in Sey 1 are very large (FWHM $1000 \div 5000$ km/s) with wings of FWHM between 7000 and 20000 km/s. Also broad lines and narrow forbidden lines are shown. Sey 2 instead exhibit more narrow lines. Moreover there are intermediate Seyfert categories (1.2, 1.3,... 1.9) based on spectral details.
- RG (radio galaxies): radio galaxies have emphasized emission at radio frequencies ($> 10^{23.3}$ W/Hz at 1.5 GHz). They show the largest linear dimensions (at radio frequencies) while the optical spectra contain only narrow line emission, if any. Distinguishing the powerful radio galaxies (PRG) from weak radio galaxies (WRG) the separation was set at $P_{1.4\text{GHz}} = 10^{25}$ W/Hz. PRG are generally the radio appearance of optical giant elliptical galaxies that are very luminous while WRG show the same host galaxy but less luminous. Representing the radio spectrum by a power law of type $F_\nu \sim \nu^{-\alpha}$ a further distinguishing

property is given by the spectral index. At 1 GHz flat spectrum RGs are distinguished from steep spectrum RG for values of $\alpha=0.4$. At the same frequency the radio maps show the classical two lobe structure. For PRG this structure is well defined while for WRG it is slightly complex and they are found to populate at higher red shift. In 1974, studying a sample of sources mapped at 178 MHz, Fanaroff and Riley (FR) introduced a further classification (Fanaroff, 1974) based on the ratio between the distance of the two opposite “hot spots” (i.e. small regions of high surface brightness) to the nucleus and total dimension of the RG. For ratio values < 0.5 the RG belongs to class FR I while for values > 0.5 it belongs to class FR II. This morphological transition corresponds to luminosity at 178 MHz of $2 \cdot 10^{25}$ W/Hz where lower values belong to class FR I and higher ones to FR II. The here explained morphology is illustrated in Fig. 2.1. The origin of the Fanaroff-Riley classification is still a matter of debate. Some authors attribute it to the slowing down of the advancing working surface (hot spot) at the end of the jet rather than of the bulk flow within the jet (Gopal-Kirshna and Wiita, 1988). The mass of the central black hole and its spin, or the composition of the plasma jet is the arguments in favor of a further model of other authors (Ghisellini, 2001).

- LINERS (low ionization nuclear emission-line region): Liners are characterised by emission lines of low ionized atoms like OI, SII. Meanwhile the ionization mechanism for Sey galaxies is due to photoionization Liners' lines originate due to shock waves.
- BL Lac (BL Lacerta) objects have spectra similar to QSO radio loud but do not show any emission line in the optical band.
- OVV (optically violent variables) are considered a subclass of QSO radio loud objects but showing large emission lines generally weaker than in QSO.
- BLAZARS: the term “blazar” is not distinctly defined but it includes BL Lac objects and Flat Spectrum Radio Quasars (Baliyan, 2001). These are usually distinguished from other types of AGN if they have some of the following properties: they are strong and compact radio sources with flat spectrum; they display strong and variable polarization especially in optical range; they possess smooth power law continuum, connecting radio, IR, optical and UV emission, indicating radiation to be synchrotron and hence nonthermal; they exhibit rapid and high variability in intensity at all wavelengths; highly relativistic jets beamed into (or close to) the line of observer's sight extend over huge distances; many of these are discovered to be γ sources as well.

An early attempt to put order in this zoo of objects lead to the Fig. 2.2. It is apparent by eye that the only class of object not fitting into this hierarchy is the blazar one. This classification scheme is due to phenomenological arguments. The milestone towards our understanding of these astrophysical objects is a classifying scheme developed on physical arguments, as discussed in this chapter.

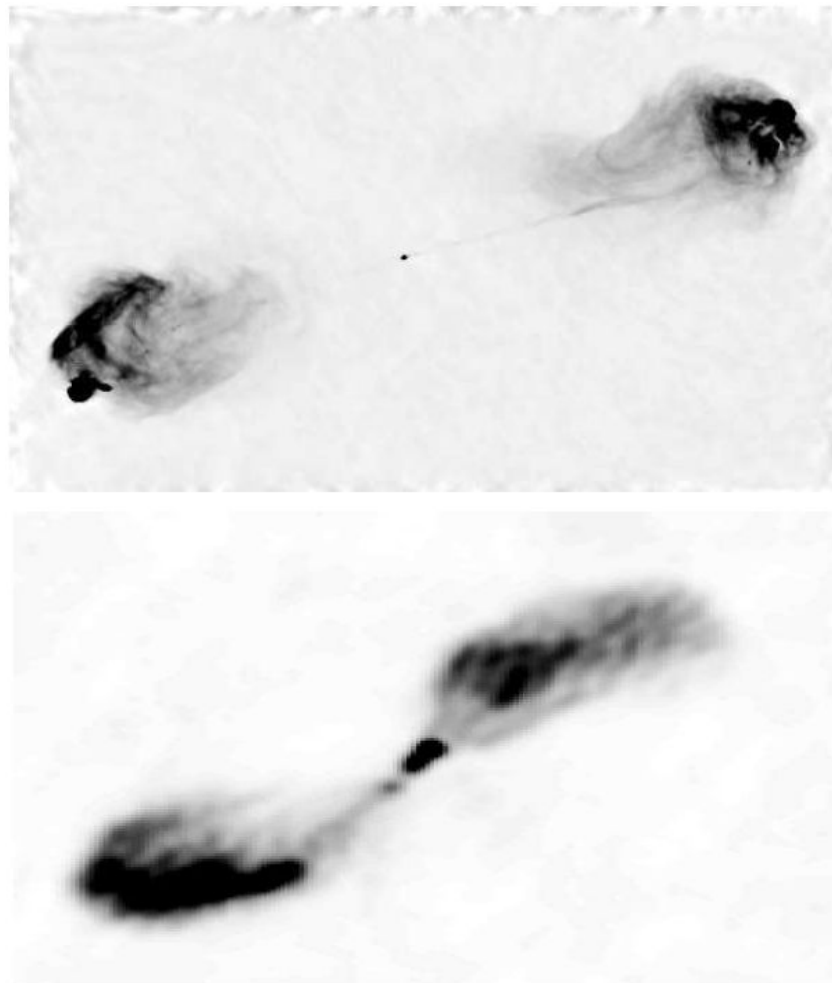


Figure 2.1. Upper panel: radio galaxy Cygnus A imaged at 6 cm. The radio galaxy extends for 127''. Lower panel: radio galaxy Centuarus A at 21 cm. The linear size corresponds to 500 x 250 kpc.

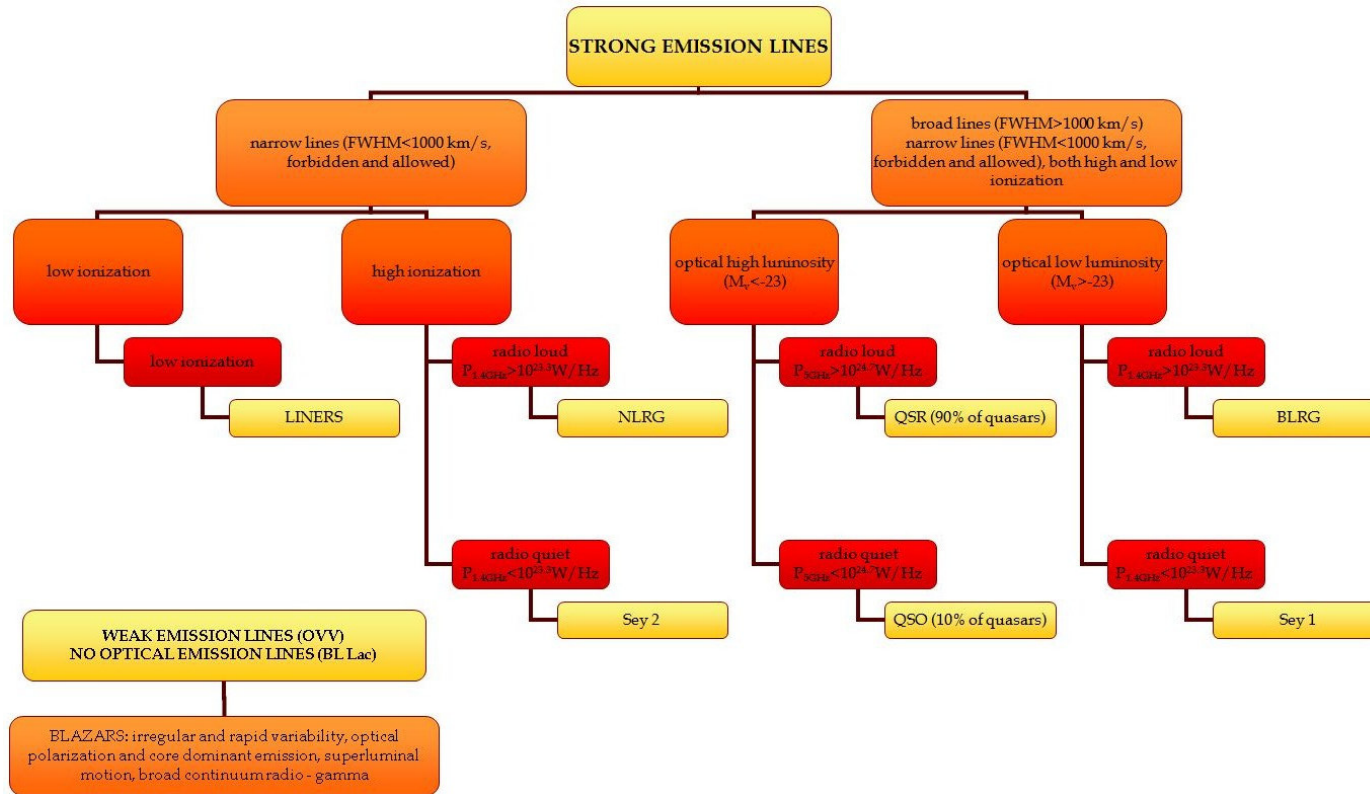


Figure 2.2 Zoology of AGN, based on phenomenological arguments.

The general accepted view of the structure of an AGN, based on several observation types, is represented in figure 2.3 and derived from (Urry & Padovani, 1995). This picture of the physical structure requires a super-massive black hole ($M \approx 10^6 - 10^9 M_{\odot}$, where M_{\odot} indicates the sun mass) lying in the center and accreting the surrounding material through its gravitational potential. The indicated mass range could be calculated by dynamical determination measuring the velocity dispersion of stars within the nucleus of known galaxies (Eckart, Genzel, & Schoedel, 2004). An accretion disk forms due to the conservation of the angular momentum of the in-falling matter and emits converting gravitational potential to thermal energy. It is thought that the plasma within the accretion disk is optically thick and thermal. Thus the radiated energy ranges roughly from optical to soft X-ray wavelength. AGN are within a small volume. Assuming a black hole of $10^8 M_{\odot}$, the gravitational radius is around $R_G \approx 5 \cdot 10^6$ pc. In such a compact environment a huge amount of energy is released compared to normal galaxies. The luminosity is at 10^{47} erg s^{-1} and makes this type of object the most luminous of extragalactic origin (explosive events excluded as said in Chapter 1).

Besides the earlier mentioned components, massive clouds of gas are moving at larger distances (up to few kpc) from the black hole. The clouds are invested by accretion disk's radiation producing strong emission lines via photo ionization and collision excitation. This feature is characteristic of AGNs' spectrum. At somewhat smaller distances from the black hole ($< \text{kpc}$) clouds are denser and have greater velocity. These cause the emission of broad emission lines ($> 1000 \text{ km s}^{-1}$) in the AGNs' spectra corresponding to permitted transitions. These clouds are referred to as broad-line region (BLR). Clouds at few kpc distance as mentioned above are of less densities and velocities, forming the narrow-line region (NLR) (Bennert, 2002). Lines originating from these clouds can be permitted and also forbidden due to their relatively low electron densities ($n_e \approx 10^{10} \text{ cm}^{-3}$).

The fact that almost all AGN show narrow lines, but not all of them show broad lines required the presence of an obscuring dusty torus. This is supposed to be located far outside the accretion disk and to obscure the BLR given a certain inclination of the AGN to the line of observer's sight. If viewed edge on the presence of gas and dust in the torus hides the central AGN environment in the infrared through ultraviolet range. This view is supported by both theoretical models (Efstathiou & Rowan-Robinson, 1995) and observations of polarized scattered light exhibiting broad emission lines of Sey 2 galaxies (Lumsden, Heisler, Bailey, Hough, & Young, 2001).

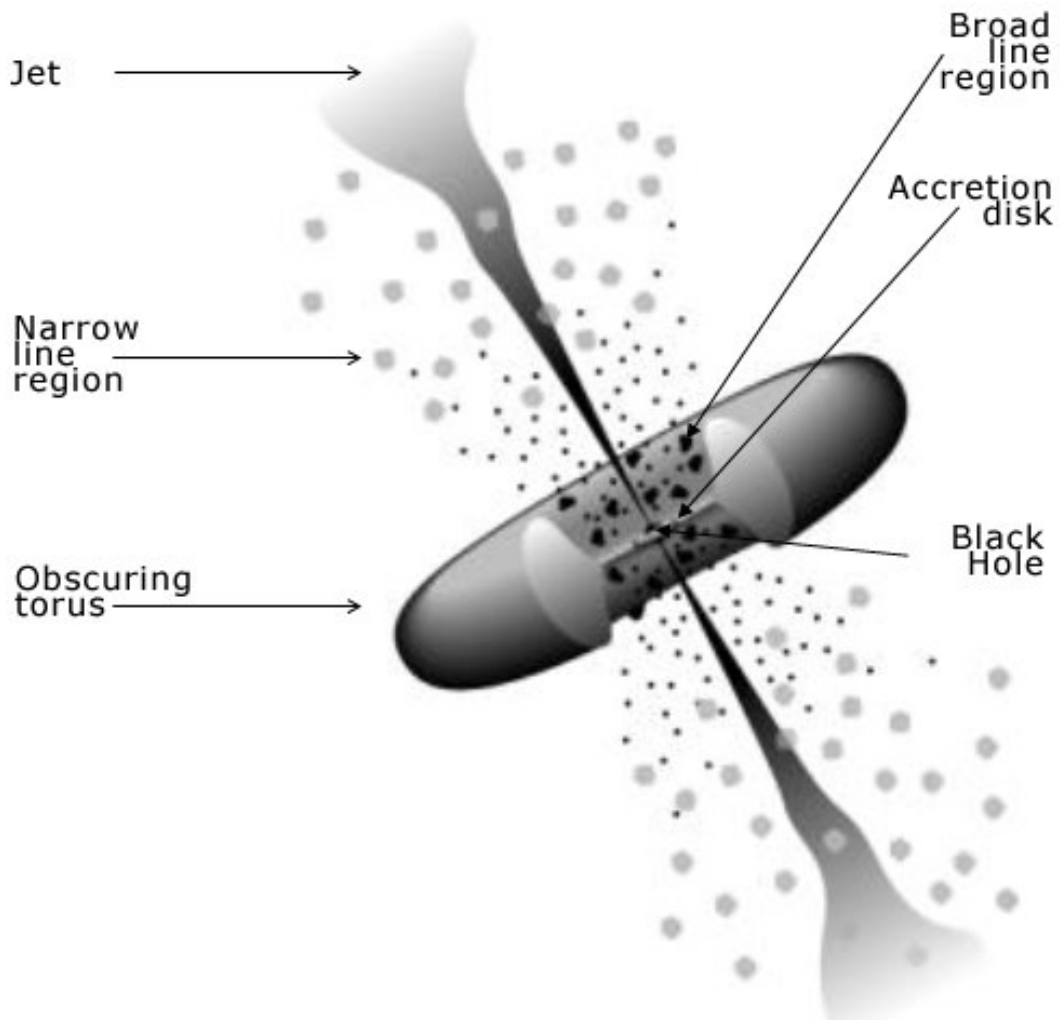


Figure 2.3: Schematic view of the current AGN paradigm (Urry & Padovani, 1995). The central black hole is surrounded by an accretion disk. In radio-loud AGN jets originate near the black hole and in some cases they extend to 100 kpc from the center. The BLR is represented by dark clouds. Further outside the central engine gray clouds show the NLR.

The obscuring torus hides the BLR to the observer watching the AGN edge-on. The inner radius of the dusty torus is about 0.1 pc.

A further characterizing component is the jet, a plasma flow of electrons and protons or electrons and positrons, streaming outward due to strong magnetic fields. This results in radiation caused by synchrotron processes. A first interpretation of this phenomenon was given in terms of equations describing a stationary axisymmetric magnetosphere of a rotating black hole where energy and angular momentum can be extracted electromagnetically (Blandford & Znajek, 1977). An alternative mechanism to this was proposed by the same author (Blandford & Payne, 1982). In this case, if the poloidal component of the magnetic field lines form certain angles with the disc surface, the centrifugally driven outflow of matter from the disc is possible. At large distances from the disc, the toroidal component of the magnetic field collimates the outflow into a pair of anti-collinear jets. This way energy and angular momentum are removed magnetically from the accretion disk, due to field lines leaving the disc surface and extending to large distances.

2.2.1 Radio Galaxies vs Blazars

The here exposed axis symmetry of the AGN modeling led to a morphological dichotomy strongly dependent on the angle between the observer's line of sight and object's axis. Radio loud AGN include radio galaxies, BL Lacs and Quasars. As discussed in section 2.2 radio galaxies show only narrow emission lines. This is explained in terms of presence of previously invoked obscuring torus and the observer's line of sight forming a large angle with the symmetry axis. The distinction between BL Lac objects and Quasars is due to their optical spectra as shown in fig 2.4 where for the former one no emission lines are present. In the case of Quasars both broad and narrow emission lines are shown. At radio frequencies these galaxies reach the largest dimensions, giving rise to the Fanaroff-Riley classification. The link between this classification scheme and BL Lacs and Quasars is given by the so called "radio-loud AGN unification" (Padovani, 1997). BL Lacs are associated to the FR I galaxies being their beamed counterpart while Quasars, pointing their jet close to the observer's line of sight, are thought to be FR II. A distinguishing characteristic within Quasar class is given by the spectral index of the radio domain associated to a powerlaw-slope of type $S_\nu \sim \nu^{-\alpha}$: Quasars showing the index $\alpha > 0.5$ are grouped into steep-spectrum radio Quasar

(SSRQ) while those exhibiting $\alpha < 0.5$ are flat-spectrum ones (FSRQ). This spectral feature gives hints to their different appearances: for FSRQ the radiation arises from the core component (flat spectrum) while SSRQ exhibit extended (steep spectrum) radio lobes having weaker radio cores. Therefore these Quasars are thought to belong to FR II where FSRQ and SSRQ form a small and intermediate angle between symmetry axis and observer's line of sight respectively.

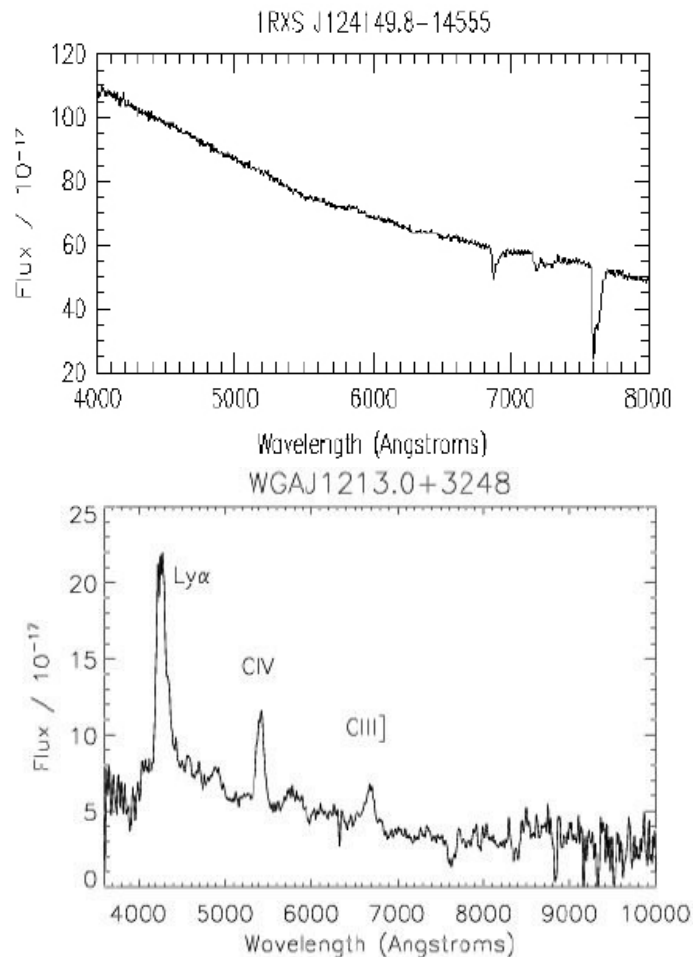


Fig.2.4: The upper panel shows a BL Lac spectrum. A redshift determination is very difficult or even impossible due to the featureless

slope. While in the lower panel the optical spectrum of a Quasar exhibits the typical strong narrow and broad emission lines.

2.2.2 Observational evidences supporting the FR I/BL Lac and FR II /Quasar association

Blazars show mostly non-thermal continuum emission extending from radio band to gamma-rays. At most wavelengths it is highly polarized, confirming the emission in origin to be synchrotron. Many blazars show superluminal expansion, which is expected when matter is moving at relativistic speed. This is consistent with a strongly beamed source caused by Doppler-boosted jet emission.

The environments of FR I and FR II give no hints about the radio galaxies-blazar association. In fact Quasars and FR IIs are located in clusters of similar richness (Wold, 2000). While Wurtz et al. (Wurtz, 1996) discovered that for BL Lacs the environment is more similar to FR IIs rather than to FR Is. Regarding the extended radio emission, Quasars exhibit typical radio powers of FR II radio galaxies. On the other hand, for the same parameters BL Lacs are associated to both FR I and FR II galaxies. Narrow emission lines are weak or absent in FR I radio galaxies, which is a characterizing property of BL Lacs (Laing, 1994). Padovani and Urry (Padovani & Urry, 1992) were able to apply successfully to the 2 Jy sample a method for the derivation of the luminosity functions of Quasars and FR II.

2.2.3 Doppler boosting

The EGRET experiment on board the Compton Gamma-Ray Observatory detected 33 blazars above 100 MeV (von Montigny, 1995). All EGRET blazars are radio-loud! As first claimed by Rees (Rees, 1966), when an emitting plasma moves with bulk relativistic motion within the jet of radio-loud AGN the energy is transported efficiently from the vicinity of the SMBH to the distant lobes. For the observer watching the jet at a relatively small angle this has strong implications. We assume that the source is moving at relativistic speed ($\beta = v/c \sim 1$). Then, if the source emits isotropically in its rest-frame C' , then the angular distribution of the radiation in the observer's frame C is peaked in the forward (with respect to C') direction. This effect is known as light aberration. The emitted photons by a particle in a magnetic field are observed in the observer's frame C within an angle given by:

$$\sin \phi = \frac{1}{\Gamma}$$

where $\Gamma = 1/\sqrt{1-\beta^2}$ is the Lorentz factor of the accelerated particle. This translates that, being in C , half of the photons are concentrated in a cone of semi-aperture angle of $\sim 1/\Gamma$ despite the available 2π of solid angle. Being the velocity vector closely aligned to the observer's line of sight (as it is believed for blazars) the intensity of a jet is extremely enhanced. This effect is called "Doppler boosting" or "beaming".

Moreover the emission and arrival time intervals of the emitted photons are different. In C the arrival time interval is given by the Doppler effect: $\Delta t_e = \Delta t_a(1 - \beta \cos \Phi)$, where Δt_e and Δt_a are emission and arrival interval respectively. This effect gives rise to the apparent superluminal motion as it is observed in blazars.

2.3 The Blazar sequence and its validity

2.3.1 The Blazar SED

The first statistical studies on blazar spectral energy distributions (SEDs) showed that BL Lacs selected at radio wavelengths showed lower ratios between X-ray flux and radio flux than those selected at X-ray frequencies (Urry & Padovani, 1995). Being the blazars' SED dominated by jet emission, an apparent dichotomy within the BL Lac class would have strong implications in matter of jet physics and object demographics in surveys. The difference between the samples was attributed to the intrinsic shape of the SED rather than to the orientation classification. BL Lacs have a large range in synchrotron peak frequency (ν_{peak}) which is the maximum output of the synchrotron peak. This led to the division of BL Lacs into low-energy peaked (LBL), with ν_{peak} in the IR/optical bands, and high-energy peaked (HBL) objects, with ν_{peak} in the UV/X-ray bands (Padovani & Giommi, 1995). Equivalently, the X-ray emission in LBL is dominated by inverse

Compton and by synchrotron for HBL. Although ν_{peak} distribution seems to be continuous now, the classification in LBL and HBL is still useful. For the more powerful FSRQ subclass, no such distinction was apparent. It was puzzling that all known FSRQ at that time were of type “L” (ν_{peak} within IR/optical bands), being the X-ray domain dominated by inverse Compton. At this point it is important to stress the fact that locating the ν_{peak} is not an easy task, as it requires SEDs build up with large number of data points. Furthermore, due to their variability, non-simultaneous blazar SEDs introduce large uncertainties. The characteristic blazar SED is shown in figure 2.5 (Urry C. M., 1998). On how to build and use an SED, the further interested reader can refer to (Gehrels, 1997).

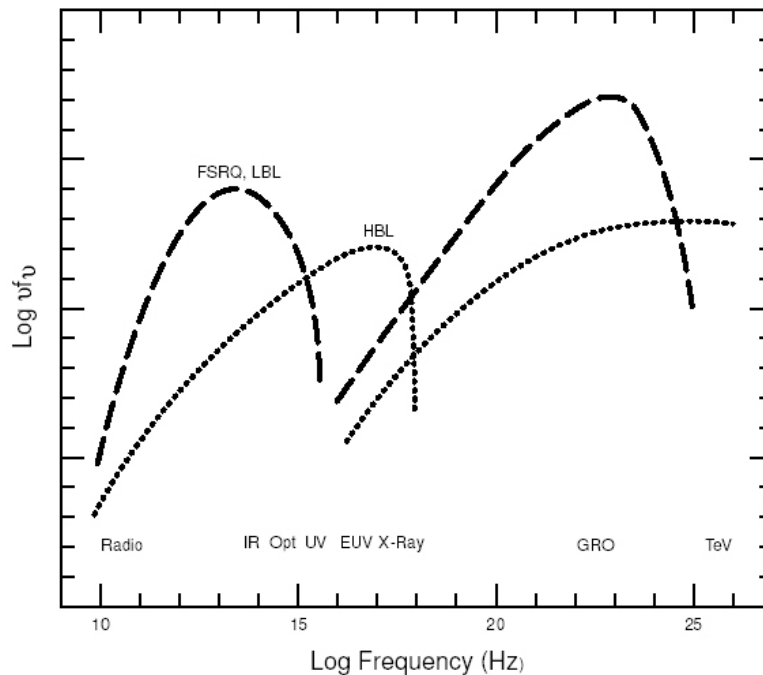


Figure 2.5: The blazar SED. The νF_ν vs ν plot shows the typical two hump structure of blazars. For LBL and FSRQ (dashed line) the low energy peak, due to synchrotron radiation, is located at IR/optical band, while for HBL (dotted line) this radiation peaks at UV/X-ray energies. The high energy components, due to inverse Compton, have maximum output in the GeV and TeV domain.

2.3.2 The Blazar sequence

After the advent of EGRET onboard the CGRO it was possible for the first time to describe the whole SED of blazars over the entire electromagnetic spectrum (e.g. (von Montigny, 1995)). The first systematic exploration of the blazars' SEDs was done by Fossati (Fossati, G. et al., 1998). They constructed SEDs of three complete samples of blazars (2 Jy radio-selected FSRQ, 1 Jy radio-selected FSRQ and Einstein Slew Survey BL Lacs X-ray-selected). Figure 2.6 shows the resulting blazar sequence which is binned according to radio luminosity irrespective of the original classification. Indeed, the SEDs look homogenous and systematic trends are clearly present. But the major outcome is given by the plots of the three samples which show their powers at various frequencies (νL_ν) vs ν_{peak} . It was found an anti-correlation where the least powerful source exhibit high ν_{peak} values and the most powerful ones show small ν_{peak} values. The theoretical interpretation of this was given by Ghisellini (Ghisellini, Celotti, Fossati, Maraschi, & Comastri, 1998) where ν_{peak} is given by B (magnetic field), δ (Doppler factor) and γ_{peak} (Lorentz factor of the electron energy which is determined by a competition between accelerating and cooling processes within the jet).

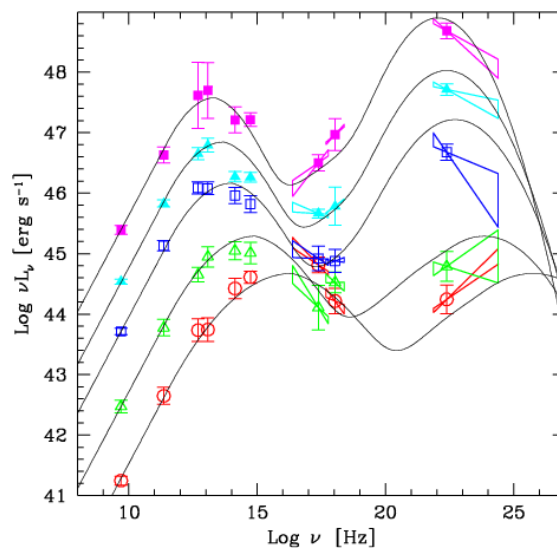


Figure 2.6: Average SED from the three blazar samples binned according to radio luminosity irrespective of the original classification from (Fossati, G. et al., 1998).

2.3.3 Validity of the Blazar sequence

The blazar sequence is still a matter of debate. It implies very precise predictions that are:

- FSRQ are more powerful than BL Lacs (they are considered the beamed counterpart of radio-loud AGN as discussed in chapter 2.2.1). An anti-correlation between power and v_{peak} implies that FSRQ with high v_{peak} should not exist.
- Observed luminosity functions show power-law slope of type $\varphi(L) \sim L^{-\alpha}$ ($\alpha > 0$). Moreover, the beaming effect, as discussed in chapter 2.2.3, is rather sensitive to small misalignments between observer's line of sight and symmetry axis. This has as consequence a decrease in luminosity. Thus low-luminosity sources are more numerous than those showing high luminosity. Again, the obtained anti-correlation from the blazar sequence implies that HBL should be more numerous than LBL.

Strong arguments against the blazar sequence came from the Deep X-ray Radio Blazar Survey (DXRBS). Its large, deep and homogeneous sample shows no anti-correlation between v_{peak} and jet power (Padovani, Perlman, & Landt, 2003), as expected in the blazar sequence. Moreover the DXRBS contains mostly FSRQ, whereas the blazar sequence expects the number of HBL to exceed that of FSRQ. The most evident violation of the sequence predicted properties came from the synchrotron dominated X-ray band of RGB J1629+4008 (Padovani, Costamanete, Ghisellini, Giommi, Perlman, & E., 2002) and recently reported ROXA J081009.9+384757.0 (Giommi, F.; et al., 2007) taken from Radio Optical X-ray ASDC catalogue (Turriziani, S.; et al., 2007), demonstrating the existence of the "forbidden" type "H" of FSRQ.

2.4 The Extragalactic Background Light (EBL)

2.4.1 What is EBL?

The diffuse extragalactic background light (EBL) consists mainly of the sum of the starlight emitted by galaxies through the history of the Universe. But it has also a component in the microwave band. It could have an important contribution

from the first stars, which may have formed before the start of galaxy formation. The main components of the EBL are:

- Cosmic Microwave Background (CMB): it is the remnant of the Big Bang, when the Universe became transparent to the radiation (radiation decoupled from matter). Due to the equilibrium between radiation and matter, the resulting spectrum was black body, which continuously cooled down reaching today's temperature of 2.75°K .
- Infrared and optical background: extending from the far infrared ($\sim 100\ \mu\text{m}$) to the UV-band ($\sim 0.1\ \mu\text{m}$), the infrared and optical background radiation is the contribution of red shifted starlight through the history of the Universe. The major contribution to the EBL is due to star formation giving the double-peaked structure in its intensity spectrum (see figure 2.5) (Vassilie, 1999).

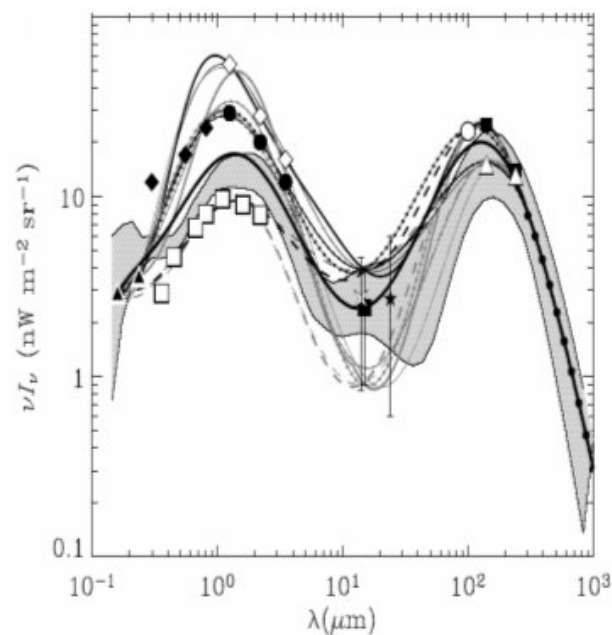


Figure 2.6: The figure shows template spectra, representing different realizations of the EBL, by fitting polynomials to all possible combinations of the following three spectral components, proposed by different authors: stellar (high, mid- and low-UV), mid-IR, and far-IR. Picture adapted from (Vassilie, 1999).

2.4.2 Measuring the EBL

The intergalactic medium is dominated by radiation, thus on their path to the Earth gamma-rays emitted from sources can pair produce. One approach to probe the EBL is to measure the attenuation through pair-production of gamma-rays from distant sources. At the Lyman edge the number density of UV-photons is expected to drop. Thus the Universe becomes transparent for gamma-rays red-shifted down to ~ 18 GeV. According to this there is only limited red-shift interval where GeV photons can undergo pair production with EBL. Any absorption feature would probe the radiation field in the primordial Universe, independently to the later star formation. The resulting effect of the attenuation is visible in blazars' gamma-ray spectrum as sharp high-energy cut-off. The present AGILE (20 MeV - 30 GeV) mission and the forthcoming GLAST (10 - 300 GeV) mission will probe the EBL within redshift 3-5. Ground-based TeV experiments are limited to redshift values of 0.2 due to the high opacity of the IR radiation (see figure 2.6 left panel) (Blanch & Martinez, 2005). The approach to study the history and evolution of star formation rate using the previously mentioned mission is a unique opportunity to access the high redshift range, which is inaccessible to optical/infrared surveys (Stecker, 2006). The determination of EBL is not easy to undertake. Unfortunately, neither the intrinsic blazar spectrum nor the EBL is known with high enough precision to accurately derive one quantity from the other. Moreover the EBL is viewed through strong sources of foreground emission consisting of reflected sunlight and thermal emission from zodiacal dust particles. Also the unsolved questions about the blazar jet models complicate the sources' spectral shape and thus the measurement of EBL. Indeed, the opacity due to pair production caused by external radiation field within the AGN system (local opacity) results in a contribution to the effective opacity $\tau_{\text{eff}} = \tau_{\text{EBL}} + \tau_{\text{source}}$ with the first addendum being the EBL-caused opacity and the latter the local opacity. Following the progress in black hole demographics a recent publication by Reimer demonstrates that for positively evolving and non-evolving accretion rates over cosmological time the local opacity shows a red-shift-dependence with larger opacity from sources at higher red-shift (Reimer, 2007). Ambiguities in the interpretation of blazar spectral absorption features are the consequences. As a result, the only suitable candidate sources (being unbiased for EBL evolution studies) are those without noticeable optical/UV radiation fields close to the gamma-ray emission region. The only subclass of AGN showing particular weak (or absent) emission lines are BL Lacs, as classified in Chapter 2. Predictions of the surface density of BL Lacs are given by Muecke and Pohl (Muecke & Pohl, 2000).

In AGILE AO-1 we were awarded data rights for the radio source PKS 0537-286 in the context of a multifrequency campaign (see Chapter 5). The source is a possible EGRET counterpart (Hartman, 1999). EGRET detected the earlier discussed source at $3.5 \cdot 10^{-7} \text{ ph cm}^{-2} \text{ s}^{-1}$. The flux limit obtained with the “AGILE Target Visibility and Flux Limit Computation Tool” is of $1.0 \times 10^{-7} \text{ ph cm}^{-2} \text{ s}^{-1}$ at $E > 100 \text{ MeV}$. According to the flux limit and to the source flux as revealed by EGRET, we were able to simulate the AGILE data (blue points figure 2.6 right panel). These are compared to the theoretically obtained spectrum (red line figure 2.6 right panel), using the model proposed by Stecker (Stecker, 2006) for the optical depth $\tau(E\gamma)$ of the Universe to γ -rays for interaction with EBL photons. The AGILE data reject the power law fit with $\chi_{red}^2 > 2.5$.

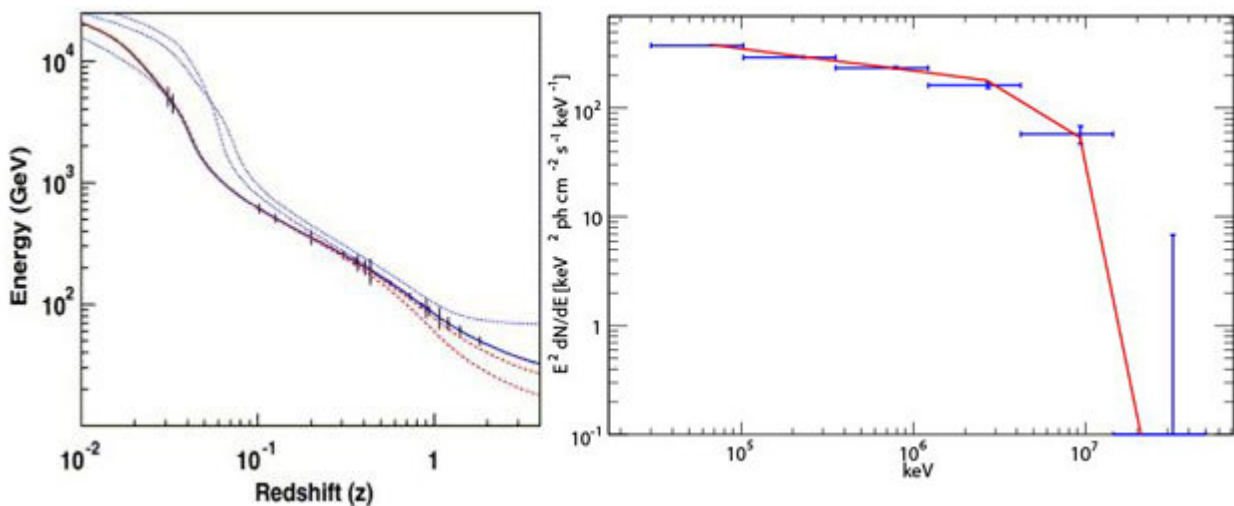


Figure 2.6: Left panel: the curves show different models for galaxy evolution with opacity $\tau=1$ of the Universe as functions of the gamma-ray energy and redshift. The Universe is optically thick in the areas above the curves limiting the TeV observations on Earth. Picture adapted from (Blanch & Martinez, 2005). Right Panel: Comparison between γ -ray data of PKS 0537-286 simulated for AGILE (using the flux limit obtained with “AGILE Target Visibility and Flux Limit Computation Tool” and the flux as revealed by EGRET) and the flux as revealed by EGRET) and the theoretically obtained spectrum for the same source calculated using the model of Stecker (Stecker, 2006) for the optical depth of the Universe to γ -rays for interaction with EBL.

2.5 The state of the art and outlook

The smooth non thermal continuum of blazars extends from radio to gamma-rays and is similar for both subclasses, FSRQ and BL Lacs. The total energetic output of these objects is mostly dominated by the high energy component. The first component of the spectral two hump structure reaches a peak in the IR/X-ray region and is due to synchrotron emission originating from electrons or protons at relativistic speed. This view is convincingly indicated by high degree of polarization (Piner & Edwards, 2005). For the high energy component, peaking at MeV/TeV energies, there is general agreement on the basic physical process, which is inverse-Compton emission. In a simple leptonic model low-energy photons are boosted via inverse-Compton. The origin of the low-energy seed photons is still a matter of debate. The Synchrotron Self-Compton (SSC) model predicts the low-energy photons to be up-scattered by the relativistic electron population (or pairs) responsible for the synchrotron emission (Bloom & Marscher, 1996) (Koenigl, 1981). The origin of the seed photons could be also external to the jet. The so-called External Compton model (Dermer, Schlickeiser, & Mastichiadis, 1992) assumes that soft photons originate from accretion disk, BLR or molecular clouds and dominate over the synchrotron contribution. While the mirror model (Ghisellini & Madau, 1996) foresees that the jet synchrotron radiation is reflected by clouds or free electrons in the BLR into the jet again. An alternative view comes from the hadronic models, which require high energy protons producing gamma-rays either through hadron-hadron collisions or photon-hadron reactions. These produce pairs and subsequently positron and electron cascade (Mannheim, 1993). Despite the huge efforts in blazar studies over the last decade, the question on how the super massive black hole transfers its gravitational energy to the outflowing plasma has remained elusive.

The confirmation of the theory comes from the phenomenology of blazars. The first blazar to be detected by EGRET was 3C 279 (Hartman, R. C., 1992). The radiation detected during a gamma-ray high state was modeled in the framework of the synchrotron-inverse-Compton (Hartman, R. C., 2001) emission where the seed photons were supposed to be internal and external to the jet. This is supported also by the results in chapter 3, where the source showed no day-scale activity. Taking in account a HBL object, Mrk 421 is one of the brightest sources of its class in the X-ray band. The source was observed during a flaring activity in the hard X-ray band in 2006. This triggered a multifrequency campaign which showed

correlated variability at all wavelength and permitted to derive physical results. The variability could be reproduced by changes of the SED-model parameter and fit to the observed data and thus conclude that Mrk 421 lives in a SSC scheme (see chapter 4). During the same campaign the source followed the well known trend “the brighter the harder” reported also by other observations for the same source (Pian, 2002). The same trend was observed in INTEGRAL AO-5 in 2007 (Bottacini, Beckmann, Ishibashi, Ajello, & Greiner, 2007) when we were awarded data right for 1ES 1959+650, a further HBL. Also X-ray/TeV correlations were found during the same campaign. In contrast to this, an interesting feature was observed in 2002 as 1ES 1959+650 underwent an active gamma-ray state: despite an increased activity in the gamma-ray domain no flux variation, measured simultaneously, was observed in X-rays (Krawczynski, Hughes, Horan, Aller, & Aller, 2004). Just little is known of this so-called “orphan”-flare. But blazars can also remain in quiescent state for a long period. This is the case of PKS 0537-286, a high red-shift FSRQ. Its complete SED is reported in chapter 5.

Simultaneous observations at X-ray and TeV energies had allowed measuring the correlation of the light curves on short time scales. Moreover the identification of relation between source intensity and variable temporal lags were possible. In this respect the actually flying high energy mission, like Swift and INTEGRAL, gave their significant contribution. While Swift is easy to schedule and therefore ideal for follow-up observations, INTEGRAL performs long pointings on single objects. Similar coordinated observations had received renewed interest after the launch (23rd April 2007) of the Italian satellite AGILE and will be pushed after the launch of GLAST in 2008. Finally, longer and denser monitoring of blazars will allow to better distinguishing between the different competing leptonic and hadronic emission models. GLAST’s effective area (1 m^2) is one order of magnitude larger than AGILE’s. GLAST will outperform EGRET, which had effective area of 0.15 m^2 . Its scanning mode will allow a constant monitoring of several tens of blazars and flare alerts to be issued. This will lead also to a uniform sky exposure. Extrapolating the EGRET the Log N - Log S, GLAST will detect at least one thousand blazars (Lott, et al., 2007).

Chapter 3

3 SOFTWARE DEVELOPMENT AND IMPROVEMENT OF IBIS STANDARD CODE

3.1 Introduction

As it is discussed in section 1.3, beside the instrumental design also the deconvolution algorithm plays a fundamental role in the sky image reconstruction for coded mask instruments. It is reductive to limit the discussion to an algorithm while it is more appropriate to refer to an entire software environment. The INTEGRAL Science Data Center (see section 1.4) provides a quick look to the “raw” data within 3 hours from the observation. These are preliminary results. This center, located in Geneva, is responsible also for the Off-line Science Analysis (OSA) software (Courvoisier, T.J.-L. et al., 2003). OSA is a package of scripts calling scientific executable code developed in C/C++ and FORTRAN. This is

compatible with Linux OS (32- and 64-bit), Solaris (32- and 64-bit) and OS X (32-bit). Details about the software and installing instruction can be found on the ISDC web site (<http://isdc.unige.ch>).

As the gamma-ray sky gets better and better covered by ISGRI and new INTEGRAL pointing strategies, aiming to detect weak sources, are adopted, the data analysis software needs improvements. Indeed, strong sources in the ISGRI X-ray sky have to be accounted during the imaging reconstruction. Moreover detailed detector models have to be developed in order to become more sensitive to weak sources. Very interesting links to the TeV sky counterpart are found. A recent example is the microquasar and TeV/EGRET/COS-B source LSI +61 303 which has been detected by INTEGRAL (Chernyakova, M.; et al., 2006) (see figure 3.1).

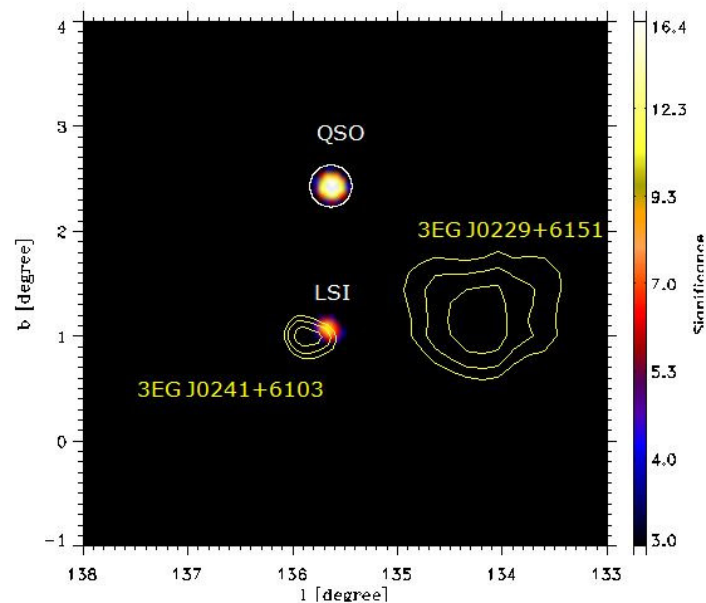


Figure 3.1: The ISGRI significance map in the energy range from 20 - 95 keV shows the detected source LSI +61 303 (Hermesen, 2007). The EGRET confidence level contours of the source 3EG J0241 +6103 are overplotted. The quasar in the middle-upper zone of the map is QSO 0241 +622.

A similar map as shown in figure 3.1 has been made for the same source with the Major Atmospheric Gamma-ray Imaging Cherenkov (MAGIC) telescope above

400 GeV. The position of the optical source LSI +61 303 and the 95% confidence level contours for 3EG J0241 +6103 were found coincident (Albert, J.; et al., 2006). In the southern hemisphere another microquasar LS 5039 was detected as a TeV emitter (Aharonian, F.; et al., 2005) by the High Energy Stereoscopic System (HESS) and positional compatible with the further EGRET source 3EG J1824-1514. Microquasars are thought to be X-ray binaries composed of a normal star in orbit around a neutron star or a stellar-mass black hole. Just little is known about their high energy emission mechanism. The questions of whether they are just down-scaled AGN are still asking to be solved.

The HESS experiment discovered very recently a number of very high energy gamma-ray sources on the galactic plane without any identified counterparts (Aharonian, F.; et al., 2008). Most of previously detected sources were identified as AGN, SNR, pulsar wind nebulae (PWN) and X-ray binaries (XRB). Very high energy emission associated with young stellar cluster was detected (Aharonian, F.; et al., 2007).

A further undetected population is the highly absorbed AGN. The unresolved component of the cosmic X-ray background is consistent as being the emission of these types of object. Despite studies of the local Universe show that Compton-thick objects should be as numerous as moderately obscured AGN (Risaliti, G.; et al., 1999), only a few of these objects were found (Comastri, 2004) (Ajello, M.; et al., 2008).

In order to find answers to the above opened questions the best sensitivity in the survey studies is crucial. ISGRI is the ideal instrument for such type of observations. Its large field of view ($29^\circ \times 29^\circ$ at 0 intensity), the very good location accuracy (40'' for 10σ and 2' for 5σ) and high sensitivity (1 mCrab for 10^6 s at 3σ) are the assets for approaching the unsolved problems in population studies. Most of the counterpart identifications of the very high energy gamma-ray sources are made with X-ray telescopes like XMM or Suzaku. But these instruments provide images and spectra up to 10 keV while ISGRI ranges up to several hundreds of keV. Some of these sources show also asymmetric emission regions (Funk, S.; et al., 2007). Thus ISGRI bridges the energy gap of imaging, spectral and timing capabilities between the earlier mentioned X-ray telescopes and the very high energy gamma-ray telescopes. The ISGRI deep sky maps are and will be unique to allow the detection of yet unidentified very high energy gamma-ray sources from GLAST, EGRET and ground-based TeV experiments. Furthermore, the sources now being discovered will form the input catalog for the next generation narrow-field instruments like Symbol-X.

Usually simple formulae are used to describe the sensitivity of coded mask telescopes, but these are only applicable if a number of assumptions are met. Very recently Skinner (Skinner, 2008) pointed out that these basic assumptions are not always fulfilled. In the following we will show how to get rid of several artifacts introduced by some instrumental and observation strategy complications by the usage of software improvements.

3.2 OSA standard software

The INTEGRAL observations are carried out in response of a scientific proposal. The satellite moves on a highly eccentric orbit around the Earth with a revolution period of about 3 sidereal days. The perigee height is 10.000 km and the apogee one is 152.600 km and with an inclination of 51.6° with respect to the equatorial plane. The aim was to minimize the background noise due to protons trapped in the radiation belt and to allow long periods of unbroken observations.

3.2.1 Data flow

The down-linked data from the satellite are forwarded from the MOC to the ISDC for scientific monitoring within less than an hour to be able to alter potential target of opportunities. After 1-2 weeks the MOC updates the dataset at the ISDC with telemetry and auxiliary data. After preprocessing, the data are consolidated and delivered (10-12 weeks after the observation) as high-level data to the PI of the accepted proposal. Starting from that moment the data remain private for the PI and become public after 1 year.

3.2.2 The data

INTEGRAL observations last usually hundreds of (kiloseconds) ks, while the instrument settings change on 1 - 10 ks time scale. As consequence the long datasets are split into Science Windows (ScWs), which is the time interval of data taking with the same instrument settings. Many ScWs belong to the same observation, that is, they form an observation group (OG). A natural grouping of

ScWs is given by the revolution period. The ScWs are just the scientific part of the data. Also the instrumental (auxiliary, housekeeping) data have to be taken in account by setting properly the data analysis environment (this can be found on the ISDC web pages documentation). Also the data base, based on ORACLE data base management system, can be queried through parameterized web pages in order to obtain a list of ScWs to be processed. The same can be done through the HEASARC web pages of NASA.

3.2.3 The software

INTEGRAL being a multiwavelength laboratory, the philosophy behind OSA is to process optical, X- and hard X-ray and gamma-ray data with single software. This means that a list of ScWs regarding an observation is enough to process the data coming from different instruments. Obviously all the instruments and analysis specific parameter have to be taken in account.

In order to avoid large systematic errors INTEGRAL performs a combination of time and spatial coding referred to as dithering. This way the systematic errors are spread uniformly all over the final image of the sky. The satellite can do a hexagonal and a rectangular dithering. The latter is the most used one and it consists of a 5 x 5 dither pattern with points spaced 2.17° apart. Also a small roll-over angle is applied which cannot be seen in figure 3.2. This figure shows also that only the central 9 out of the 25 dither pointing yield useful JEM-X data for the central source in case of rectangular dithering. This results in only 23% of effective observation time. Therefore, even though the 4 instruments on board the INTEGRAL satellite are co-aligned, not all of them observe the pointed source simultaneously. As consequence, not all ScWs useful for ISGRI are so for JEM-X (and obviously also for OMC).

We will focus on OSA for ISGRI. The single steps of the standard processing pipeline are:

- COR: tags noisy pixels and computes the energy deposit of the event
- GTI: extracts good time intervals and merges them (house keeping data, satellite stability, data gaps)
- DEAD: computes the dead time (instrument, veto)
- BIN_I: creates shadowgrams in chosen energy bins (intensity shadowgrams and corresponding efficiency maps)

- CAT_I: creates a catalog from a given list of sources in the field of view
- IMA: shadowgrams are deconvolved making use of cross correlation, via Fast Fourier Transformation (FFT), with a deconvolution array being the mask pattern; source search is performed in the single ScWs as well as in the final mosaiced image of the sky

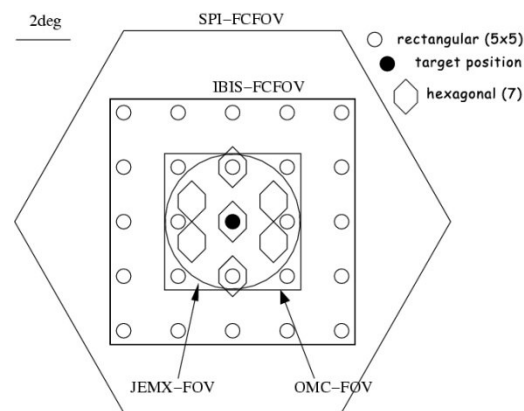


Figure 3.2: The FCFOV of each instrument is shown and centered on the target (filled circle). The empty circles are the 2.17° dithering steps while the hexagons represent the hexagonal one. The roll-over angle is not shown.

3.2.4 Image statistics

The standard ISGRI imaging software does a good job. However sometimes systematic errors exceed statistics one in deep images. The reasons that lead to the effects shown in figure 3.3 and 3.4 can be many. Accurate detector background maps are difficult to derive; they are time variable, energy dependent and very often there is a temporal leak of flat field observations. The periodic shape of the IBIS mask can give rise to imperfect ghost cleaning and thus the presence of this artifact. Multiple sources are entangled due to the PSF. The coded mask theory exposed in section 1.3 requires some assumptions which are not always fulfilled (Skinner, 2008). These differences to a “real” coded mask instruments can be summarized and grouped into 3 main instrument aspects:

- Detector: detector's finite position resolution, efficiency non-uniformities, background non-uniformity, gaps in detector plane, dead/inactive pixels, response dependence on off-axis angles
- Mask: mask's closed element absorption and open element transparency, element thickness, non cyclic mask
- Other: imperfect shielding, obstructions between detector and mask

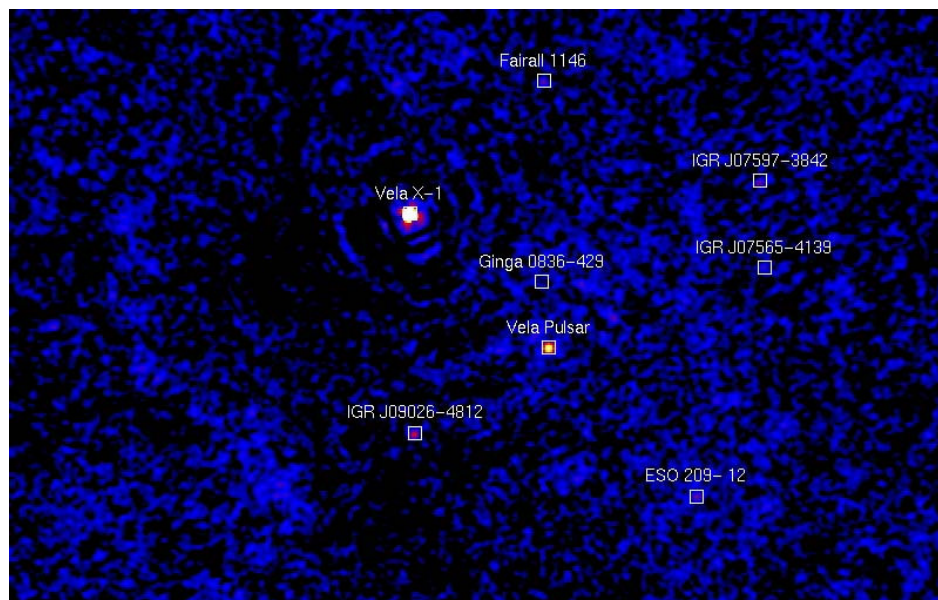


Figure 3.3: This is the significance map of the Vela region in the 20 -60 keV energy band with effective exposure of 1.6 Ms. The image has logarithmic color scale. Vela X-1 is detected at more than 1000σ . The PSF is perfectly recognisable leading to side-lobes and visible as concentric rings around the source Vela X-1.

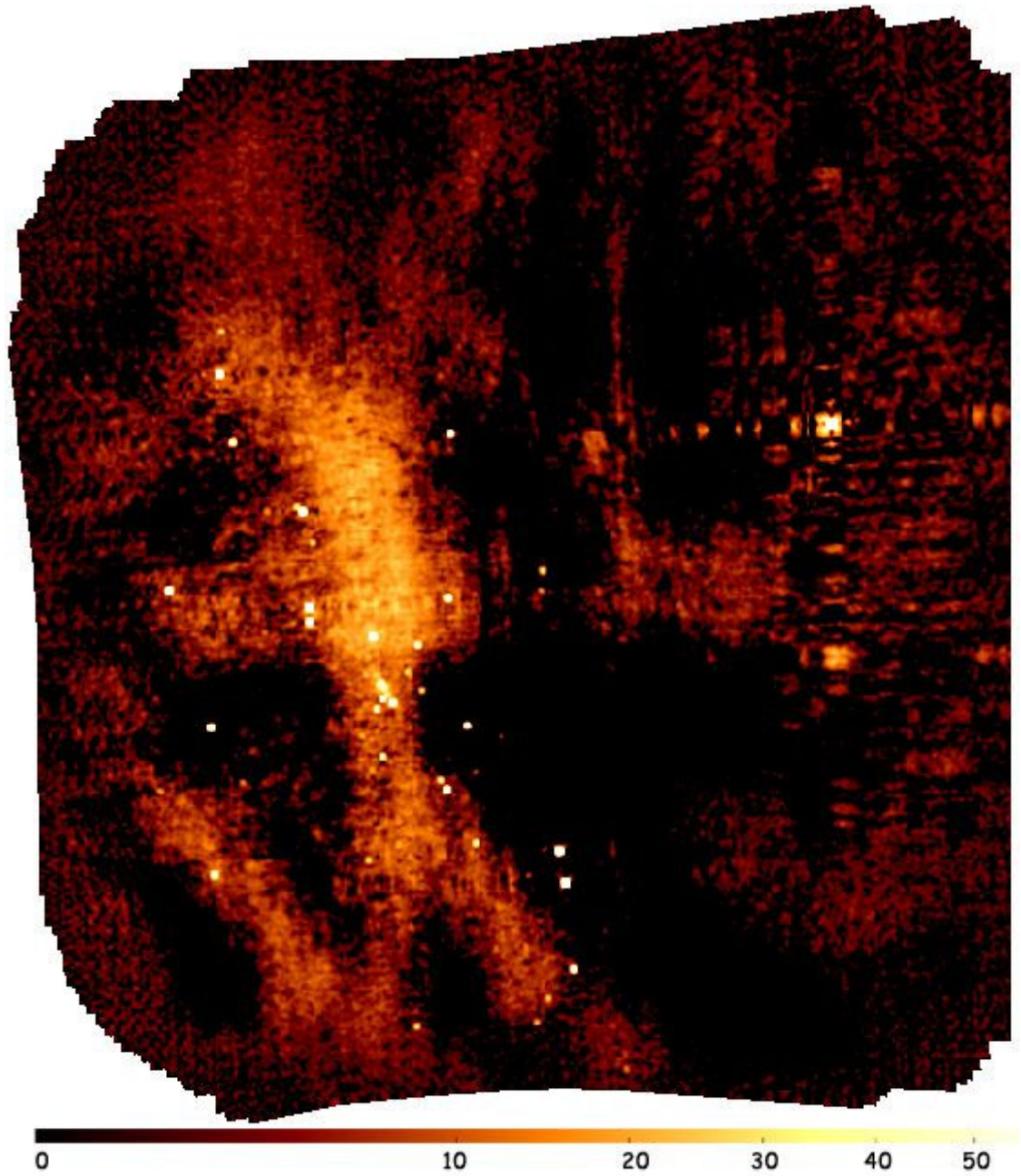


Figure 3.4: This significance map being color coded in square root scale shows the region of the galactic center obtained with OSA 7.0 having an

effective exposure of 6.5 Ms. The bar beneath is the color coding for the significances. In the upper right area the source Sco X-1 first cosmic X-ray source to be discovered (Giacconi, Gursky, Paolini, & Rossi, 1962) is detected at 1595σ . Also its ghost can be clearly seen by eye! The diffuse component on the left side is due to the galactic plane. Many point-like sources are therein. On its right side the maps shows dark areas exhibiting negative significance values.

3.3 Software improvement

In order to avoid the above exposed artifacts in the final sky image, several actions can be adopted. The first step consists in a proper data screening. Most of the effects like solar flare or satellite instability are properly tagged by the ISDC. But still a number of the ScWs show artifacts, mostly due to the perigee passage where the background model is not any longer representative of the real background.

Since the PSF of a point source fills the whole detector plane and if there are more than one source in the field of view, then each source is background for the other. This becomes a serious problem for strong sources that out-shine the weaker one. Thus the latter can still remain undetected. This is the typical situation on the galactic plane where strong sources dominate. Here source subtraction becomes inevitable. This necessity is enhanced by the fact that the ISGRI survey is biased by the target observation. All on-axis sources are known to be detected in advance. Moreover a proper weighting in the background subtraction has to be applied. As discussed above the theoretical instruments deviates from the real one. Therefore a model of the detector plane can account for several effects. It should represent the best possible reality of the detector.

3.3.1 Data selection and screening

Unfortunately no diagnostic tools are available before the data are processed. Therefore the first step is to run the standard software which produces for each chosen energy bin and for each ScWs a map of intensity, variance, significance and residual. The data can be screened according to the median count rate with

respect to each ScWs and its distribution. The aim of this first step is to find bad ScWs regardless of the reason. These are then further inspected. About 1.5% is found to be above any acceptable value. This results usually from the data taking near the perigee passage of the satellite, where data are subject to bad background modeling.

A more sophisticated way for screening the data is to look at the statistics of each single ScW image. To this end, we have developed a software in IDL (Interactive Data Language) that provides a graphical user interface. It allows browsing for observations regardless to the number of ScWs and energy bins, retrieve the information for each SCWs (like the number of bad or dead pixels of the detector, image rms, count rate, ScW number etc.) and represent them graphically. The parameters obtained from the statistics can be plotted against each other. Thus their consistency can be inspected. Results can be saved and re-loaded without re-triving the informations once again. Due to a proper handling of the working session the software can be instantiated simultaneously by more than one user, avoiding problems related to the persistence of the data in shared memory areas which is typical in IDL applications. As an example the standard deviation of each ScW is plotted versus time in figure 3.5. Those ScWs exhibiting a standard deviation above a certain value are inspected by eye. The reason for this can be for example a very strong source in the field of view. Also ScW having a short exposure (around 600 sec) and thus having poor statistics, can give rise to this statistical behavior. ScWs that cannot be recovered are rejected and not used for scientific purpose neither for imaging nor for spectral analysis. The total amount of rejection is at present at 3% within 1 Ms of observations.

3.3.2 Shadowgram correction

The shadowgram correction is done combining scripting routines in Python (an appropriate `lsgrilib` library was created) with executable written in C++. The raw detector data are corrected for efficiency, background, detector models and sky source contribution.

Efficiency corrections are performed arithmetically. Efficiency maps are obtained from the house keeping data and take in account two components:

- dead time: delay following a photon detection during which another event cannot be recorded

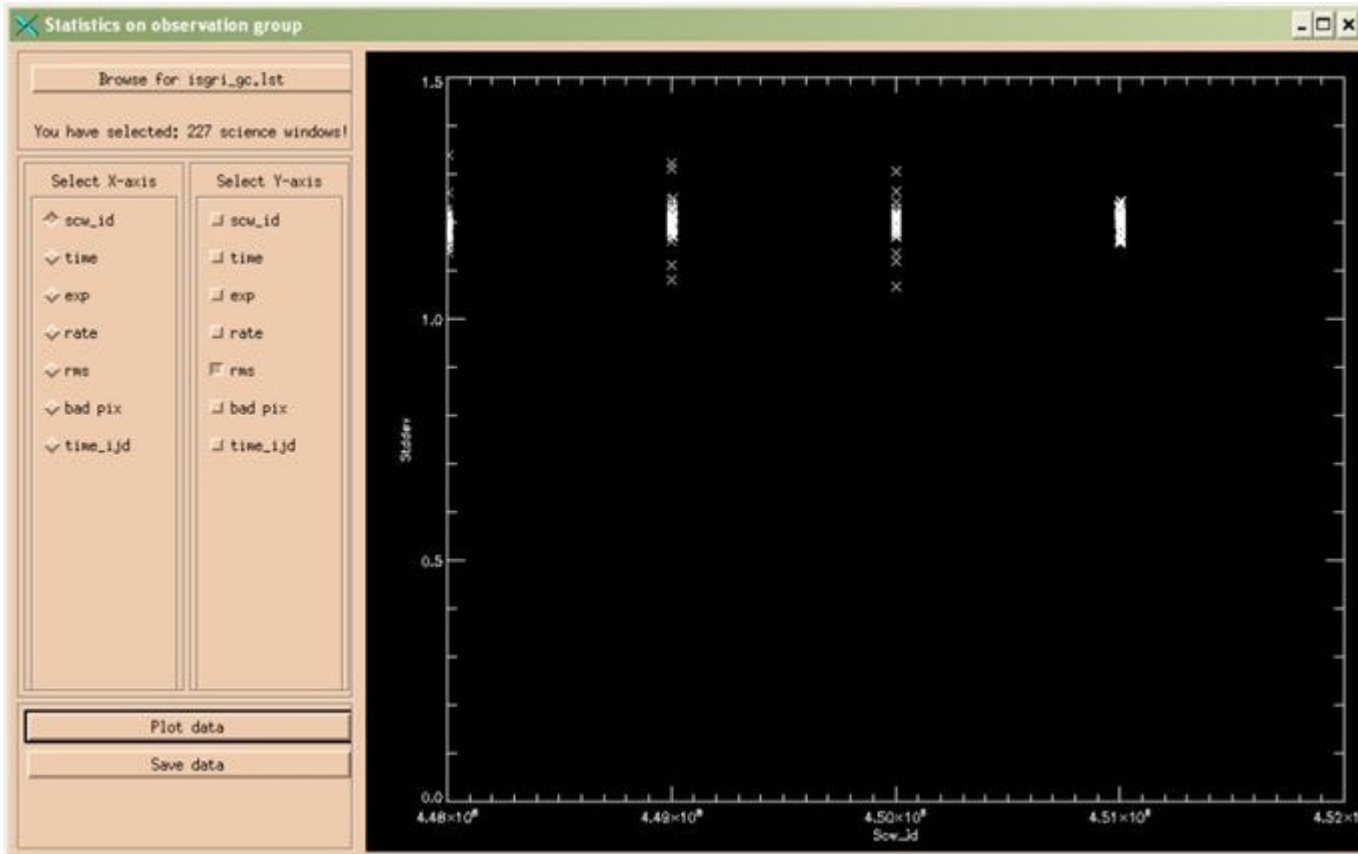


Figure 3.5: The interface of the software for data screening and selection is shown. Several parameters from the image statistics can be plotted. This allows to verify the behaviour of each ScW. In this case the standard deviation of each ScW is plotted against ScW-number (corresponding basically to the data taking time). They take values within 1.20 ± 0.15 .

- efficiency energy dependence: for the low energy bins due to the low threshold operation limit.

The efficiency map results therefore from the following formula:

$$E_{eff}[Tbin, Ebin, y, z] = (1 - D[Tbin, mdu]) \cdot LT[Ebin, y, z]$$

where *Tbin* and *Ebin* are time and energy bin respectively, *D* is the detector dead time and *LT* is the correction for the low energy dependency.

Background maps are provided by the ISGRI instrument team. These maps are created on the base of observations containing only faint sources in their field of view. On short time scales the statistical uncertainties exceed the background features. Therefore, the background subtraction not always ensures best results.

Sophisticated detector models are crucial as they take in account systematics for each ScW. One of the most important model components is related to the physical structure of the detector itself. The supporting structure introduces gaps between the modules of ISGRI. Pixels contiguous to these gaps show higher count rates. Pixels touching two gap surfaces show even higher count rate. Moreover the behavior of the entire modules is taken in account. Also typical effects like vignetting are considered.

Each source in the field of view is also background for the whole detector. Therefore, for the reasons discussed above, also the shadowgram of the projected mask pattern onto the detector plane must be fitted. A model for each source is created. The Pixel Illumination Factor (PIF) is a number between 0 and 1. It expresses the theoretical degree of illumination of each pixel in the detector plane of a coded mask instrument. The PIF is computed according to the position and is normalized to 1 count/pixel source. Depending on weather sources are detected in a single ScW, the relative PIFs are created.

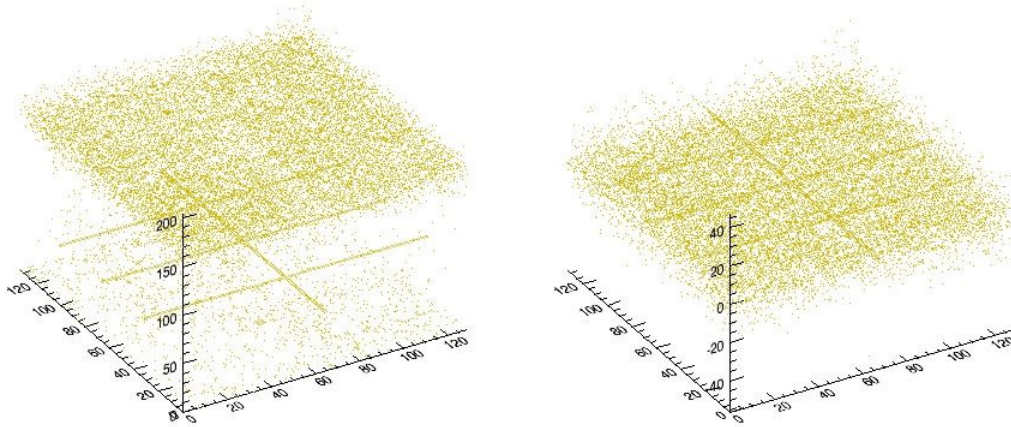


Figure 3.6: The corrected counts of the detector plane of one ScW are shown. The counts are plotted in the detector coordinate space. Left panel: the detector plane counts obtained with standard software. Right panel: the detector plane counts using the improved software.

When observing a field hosting n sources the resulting detector image is the sum of the n shadow patterns plus the background, resulting in $S(y,z)$ counts in the pixel having position given by y,z detector coordinates. We then fit our previously described models to the shadowgram extracting the level of the background, level of our detector models and the flux of the source. Finally we remove bright sources, background and detector models as follows:

$$S(y,z) = S(y,z) - \sum_{i=1}^n [f_i \cdot PIF_i(y,z)] - bB_{mod}(y,z) - \sum_{j=1}^m d_j D_{j,mod}(y,z)$$

with $PIF_i(y,z)$ and f_i being the flux and the pixel illumination fraction cast on the detector of the i -th source respectively in the pixel (y,z) . $B_{mod}(y,z)$ corresponds to the values from the background maps and b is the normalization factor so that $bB_{mod}(y,z)$ is the background in the pixel. $D_{j,mod}(y,z)$ corresponds to

the j -th detector model in detector position (y,z) and d_j is the obtained fit parameter.

Tests for the goodness of the single fit are done with χ^2 -test . Figure 3.6 shows a detector shadowgram obtained with standard OSA and the same with the improved software.

This leads to an improved standard deviation for each ScW and thus many artifacts can be properly avoided. Figure 3.7 shows the standard deviations for each ScW using the improved software. As comparison figure 3.5 shows the plot of the same parameters obtained with OSA standard for the same ISGRI observation.

Considering our method, we test the perfectly symmetric Gaussian noise in the reconstructed image by fitting a normal distribution to the significance map. The result is shown in figure 3.9 where the red line represents the fitted values.

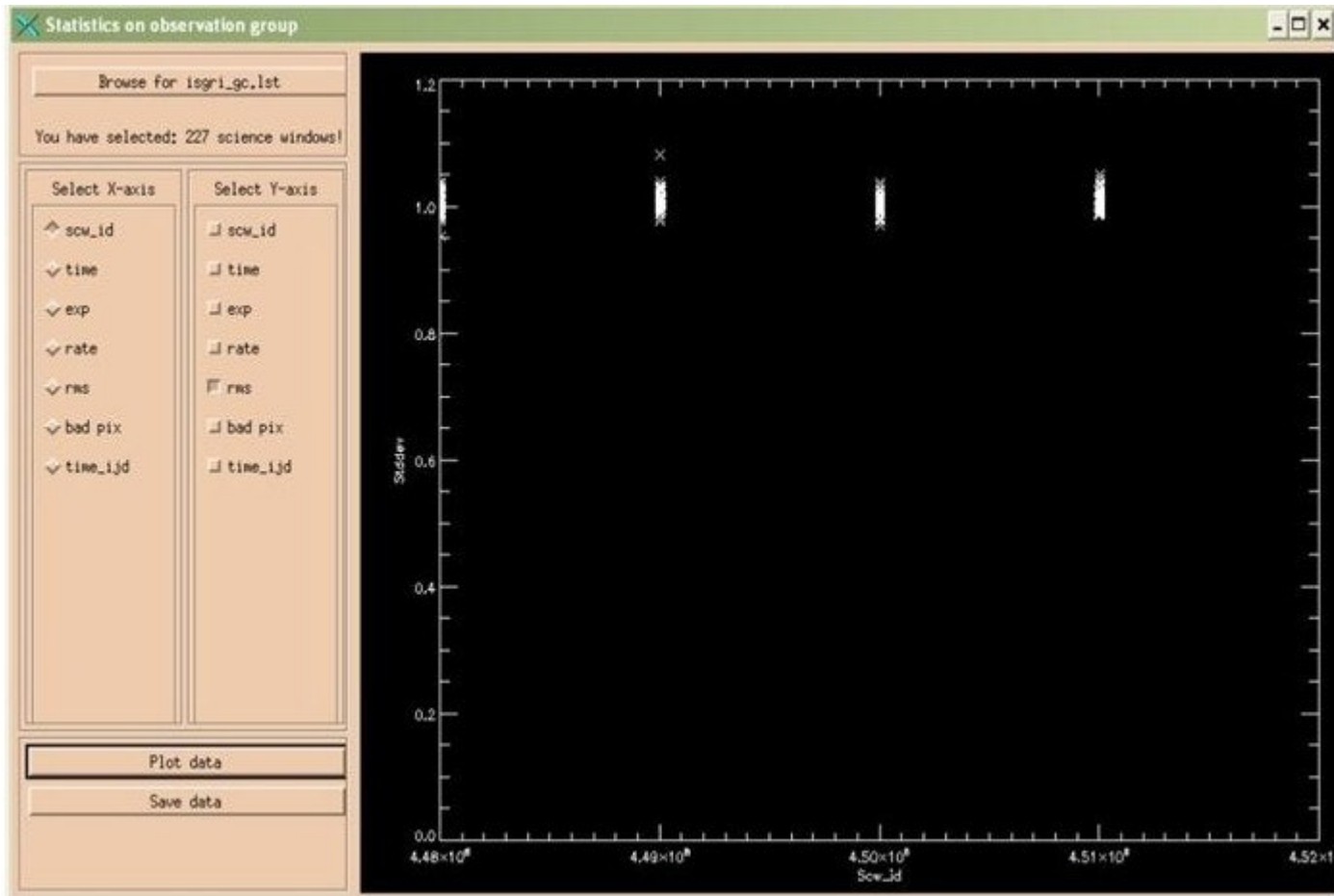


Figure 3.7: This figure and figure 3.5 show the standard deviation of each ScW of the same ISGRI observation using the improved and the standard software respectively. The standard deviation has values of 1.0 ± 0.1 .

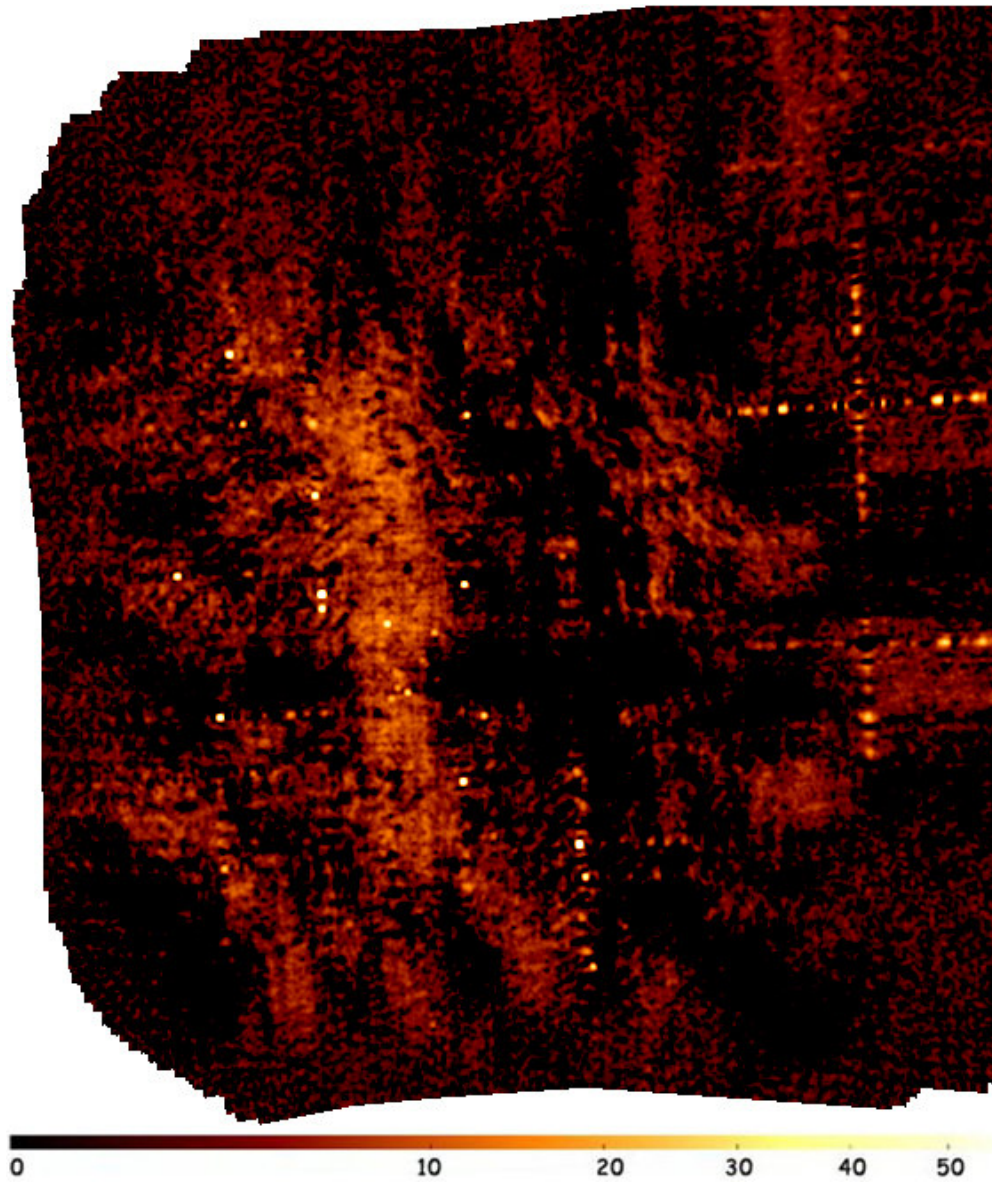


Figure 3.8: The image shows the same significance map as in figure 3.4. Also the color scalings are the same. In the upper right corner the source Sco X-1, together with its ghosts, have been removed completely. Still

some artifacts of the source can be seen. This has been recently found to be due to contaminating material on the coded mask. It will be properly modeled and accounted in the next software release. On the galactic plane the “diffuse” emission is on a much lower level, permitting the weak sources to emerge.

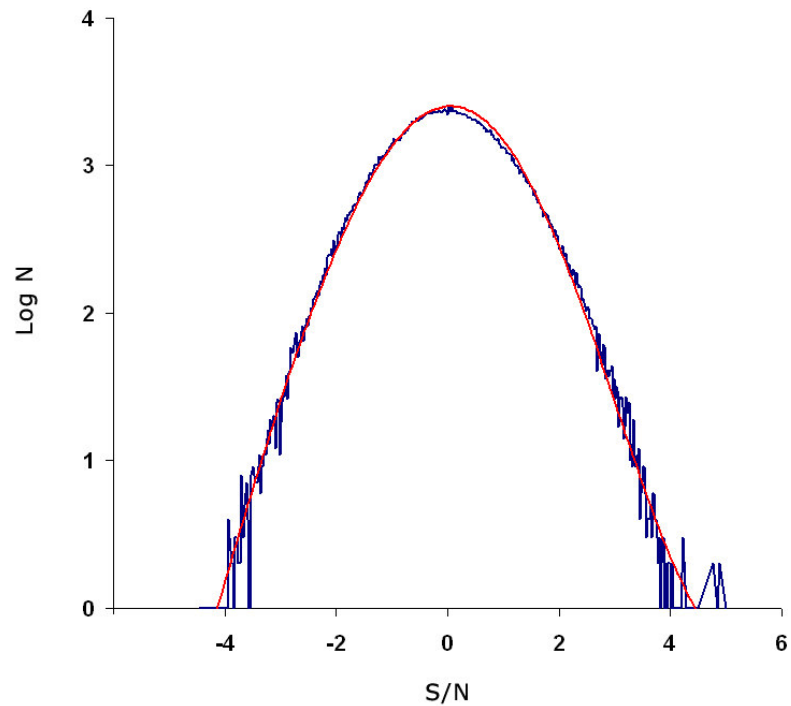


Figure 3.9: The blue line shows the S/N distribution of the reconstructed image. The red overlaid line is the fitted Gaussian distribution with $\sigma=1$. The data are perfectly symmetric.

Chapter 4

4 INTEGRAL OBSERVATION OF GAMMA-RAY BLAZARS

4.1 INTEGRAL OBSERVATIONS OF THE GAMMA-RAY BLAZAR 3C 279 DURING THE ‘DEEP EXTRAGALACTIC SURVEY’

4.1.1 Introduction

The prominent Gamma-Ray blazar 3C 279, an optically violently variable (OVV) quasar, was observed by INTEGRAL in AO-3 several times during the so-called “Deep Extragalactic Survey“, which foresaw 1 Ms of total exposure time on the Virgo sky region. The blazar was detected with 6.9σ in the 20 - 60 keV energy band

at a flux level of $(1.16 \pm 0.24) \times 10^{-11} \text{ erg cm}^{-2} \text{ s}^{-1}$. A power-law fit between 20 and 100 keV resulted in a photon index of 2.0 ± 0.4 . By combining our flux results with other INTEGRAL observations of 3C 279, we find a constant flux level at hard X-ray energies. This is in contrast to observed significant variability in the optical band, showing that there is no simultaneous correlation between the optical and the hard X-rays.

The EGRET telescope on-board the Compton Gamma-Ray Observatory (CGRO) detected about 90 blazars during its mission [1]. One of the best studied of these sources is 3C 279, an OVV quasar located at a red-shift of 0.538. This quasar, as all OVV, shows variability at all wavelength bands, and also highly variable optical polarization [2]. Several multi-wavelength campaigns on 3C 279 were carried out during the last 15 years, and hence there are plenty of archival high-energy data available for this object.

According to the “Unified Scheme” for AGN, blazars are thought to be those objects viewed at a small angle to their jet axis [3]. Their observed spectral continua are predominately of non-thermal emission arising from a relativistic jet [4]. Due to beaming effects, the non-thermal emission component dominates or even outshines completely, like in the case of 3C 279, the thermal emission of a blazar. In a ν - F_ν representation, the non-thermal jet component shows for blazars a typical two-hump structure. 3C 279 shows such a typical blazar spectral energy distribution (SED), which is rising in the radio through millimeter band, falling in the IR through UV band, and again rising in the X-ray band and falling at GeV energies, showing the typical two-hump shape broadband (e.g., Fig. 1 from [5]). The first spectral component is generally interpreted as being synchrotron radiation from high-energy electrons moving in a magnetic relativistic jet, which at the low end (radio to mm) is self-absorbed. The high-energy emission is believed to be IC emission, where the relativistic electrons upscatter lower-energy photons. It is still unclear, which is the dominant population of the upscattered target photons. To discriminate or at least to provide constraints on the emission models, multiwavelength variability has to be considered, because the different blazar emission models make predictions on variability correlations (or anti correlations) of different spectral components.

In this paper we present the results of an analysis of the yet available 3C 279 INTEGRAL (IBIS/ISGRI, OMC) data of the so-called “Deep Extragalactic Survey”, which is performed during INTEGRAL AO3. We then combine these results with similar results of other INTEGRAL observations.

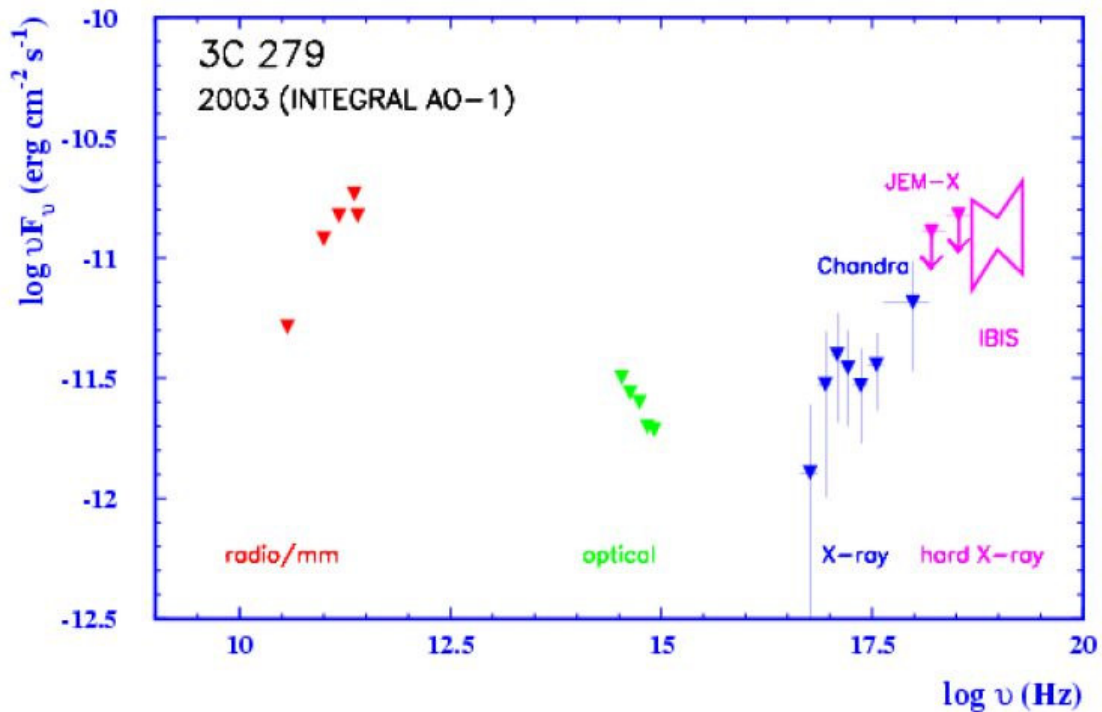


Fig. 1. The 3C 279 low-state multiwavelength spectrum as measured during the campaign in June 2003 [5]. The broadband SED shows the typical two-hump shape.

4.1.2 Observations

The “Deep Extragalactic Survey” consists of a rectangular dithering pattern of 5×12 (dither step 2.17°) centered on RA/DEC (J2000) = $12\text{h}34.5\text{m}/03^\circ 32'$. This pattern is repeated several times, leading to a total exposure time on the Virgo sky region of 1 Ms. These observations were accomplished only partly, i.e. in the first visibility period of the Virgo region in May, June, and July 2005 (INTEGRAL revolutions 320, 321, 334) and in May and June 2006 (revolutions 443 to 445)

leading to a total Virgo exposure time of more than 650 ks. The remaining 350 ks were not carried out.

Also other INTEGRAL observations were taken in account in order to investigate possible long term variations (see section 4.2). Table 1 summarizes some observational details of the analyzed observations.

Observations	Exposure (s)	Science Windows
June 2003 (PI obs.)	290405	88
Survey 2005 (May-July)	327145	239
January 2006 (ToO)	505043	149
Survey 2006 (May-June)	334136	162

Table 1: The data used

4.1.3 Data analysis

4.1.3.1 High-energy observations

The analysis of IBIS data have been performed using the INTEGRAL Offline Scientific Analysis (OSA) version 5.1. The most recent response matrices available for standard software were used for spectral analysis. Data screening was performed according to the median count rate with respect to each science window and their counts distributions in the energy band 20 - 60 keV. By omitting science windows having an excessively high count rate, we end up with a total of 401 science windows for the “Deep Extragalactic Survey” in 2005 and 2006. This corresponds to 659217 seconds of exposure time, for scientific analysis. They have

been analyzed in a combined manner, as well as by separating the 2005 and 2006 data.

4.1.3.2 Optical observations

Also the corresponding OMC (Optical Monitoring Camera) data were analyzed using OSA 5.1. OMC provides the optical flux in the Johnson V band. The flux measurement was obtained by considering a box of 3 x 3 detector pixels, which corresponds to a region on the sky of about 1 x 1 arcmin. Since OMC reports brightness measurement roughly every 10 minutes, an optical V band light curve is obtained, from which we calculated mean magnitude values by weighting on the error bars of the single points.

4.1.4 Results

4.1.4.1 Deep Extragalactic Survey

For the total (2005 and 2006) of the Deep Extragalactic Survey, 3C 279 was detected by ISGRI at energies between 20 and 60 keV with a significance of 6.9σ . Fig. 2 shows an image of the sky region around 3C 279 for this period.

The hard X-ray spectrum for the sum of the data (corresponding to Fig. 2) was obtained in the energy band from 20 - 100 keV by using 6 energy bins (Fig. 3). By fitting a power-law shape (Fig. 3), we derive a photon index of 2.0 ± 0.4 (1σ), which is consistent with the value previously derived by [5]. We derive a flux (20 - 60 keV) of $(1.16 \pm 0.24) \times 10^{-11}$ erg cm⁻² s⁻¹.

By analyzing the 2005 and 2006 survey data separately, we detect 3C 279 at significance levels of 4.6σ and 5.3σ and flux levels of $(1.32 \pm 0.38) \times 10^{-11}$ erg cm⁻² s⁻¹ and $(1.53 \pm 0.49) \times 10^{-11}$ erg cm⁻² s⁻¹ in 2005 and 2006, respectively.

The analysis of the OMC data led to V-band light curves during 2005 and 2006. Calculating the weighted means resulted in 14.33 ± 0.01 mag for 2005, and in 14.48 ± 0.02 mag for 2006.

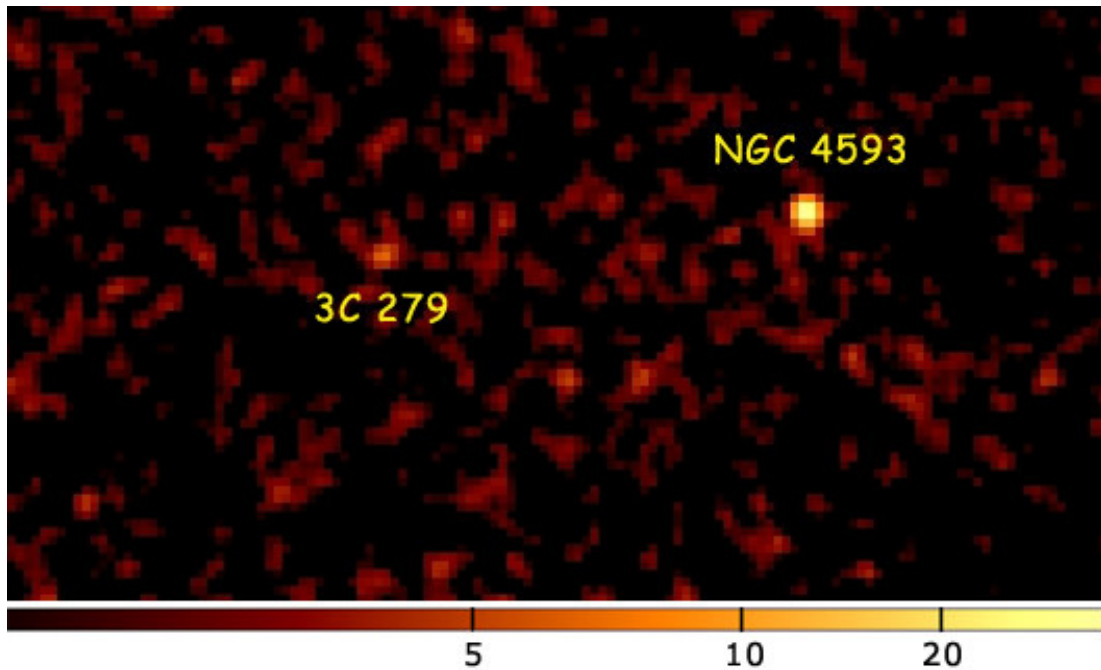


Fig. 2. 3C 279 is ‘seen’ by ISGRI with a detection significance of 6.9σ . The Seyfert galaxy NGC 4593 is with 14.6σ more significantly detected. The image shows the significance map using the color scaling in square root scale. The bar beneath is the color coding for the significances.

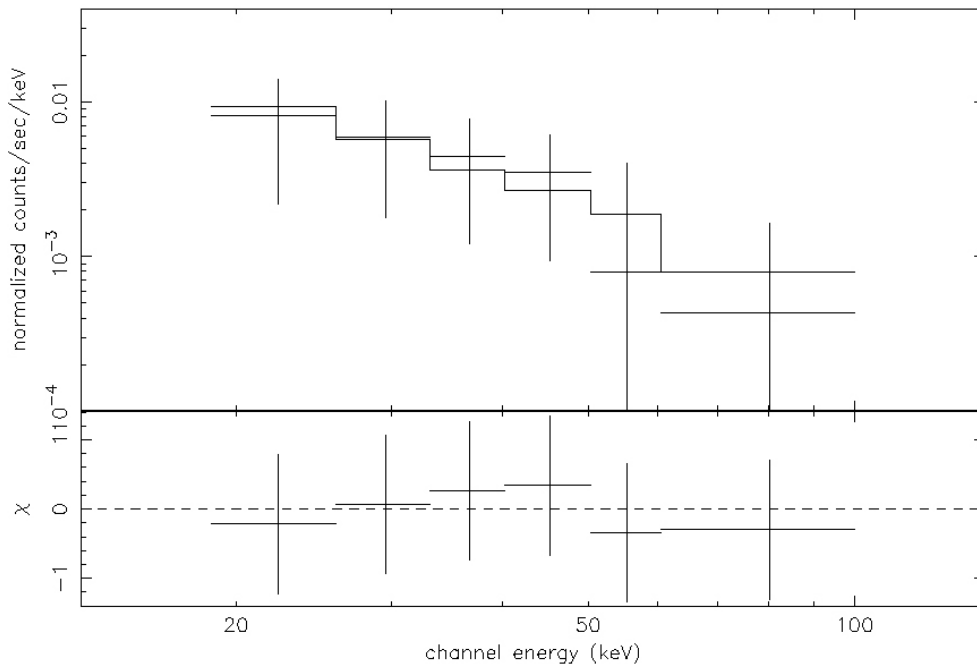


Fig. 3. The ISGRI spectrum in the energy band 20 - 100 keV with the best fit power-law is shown.

4.1.4.2 Combined results

In order to test for possible long-term trends, we combined our “Deep Extragalactic Survey” results with other available measurements during the INTEGRAL mission. INTEGRAL observed 3C 279 in a regular PI observation in June 2003 for 300 ks (see [5]) and in a ToO observation (PI: W. Collmar) triggered on an optical high state, in January 2006 for 511 ks, which was supplemented by a multifrequency campaign (see [6]).

To have a consistent set of results, we analyzed or re-analyzed the INTEGRAL ISGRI and OMC data of the June 2003 and the January 2006 observations, by using the same analysis tools (OSA 5.1) and methods as for the “Deep Extragalactic Survey” observations (see section 3). Table 1 summarizes some observational details of the analyzed observations, and Fig. 4, as an example of our analysis, shows the OMC V-band light curve for the January 2006 ToO observation. The calculated mean V-band brightness of 15.43 ± 0.01 mag, agrees well with the

value of ~ 15.4 mag (the source varied between ~ 15.2 and 15.7 mag during the INTEGRAL observations), which was measured by supplementing optical observations in the multi-wavelength campaign (see [6], also for the ISGRI results of this observation).

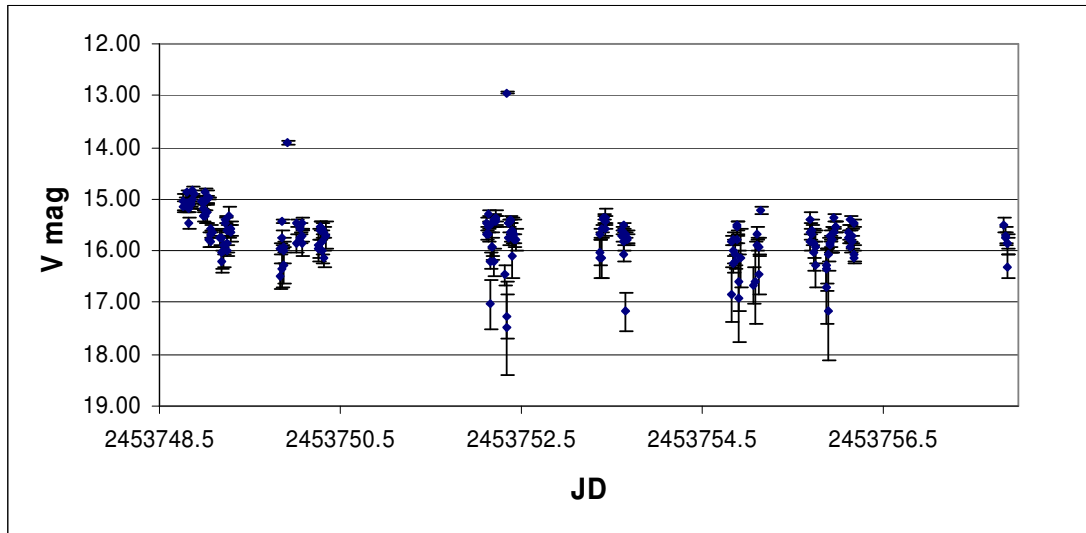


Fig. 4. The optical light curve, obtained with OMC of the ToO observation in January 2006, which was supplemented by a multifrequency campaign, is shown.

During the June 2003 INTEGRAL observation of 3C 279, also supplemented by a multifrequency campaign, the blazar was found in the deepest optical low-state of the last ten years [5]. Its V-band brightness was measured by optical telescopes to be about 17.2 mag. Because this is close to the limiting magnitude of the OMC, we use this accurately measured value instead of the result of our OMC analysis, which yielded a somewhat brighter source. The results of our analysis, i.e. the light curves of the two wavelength bands, are shown in Fig. 5.

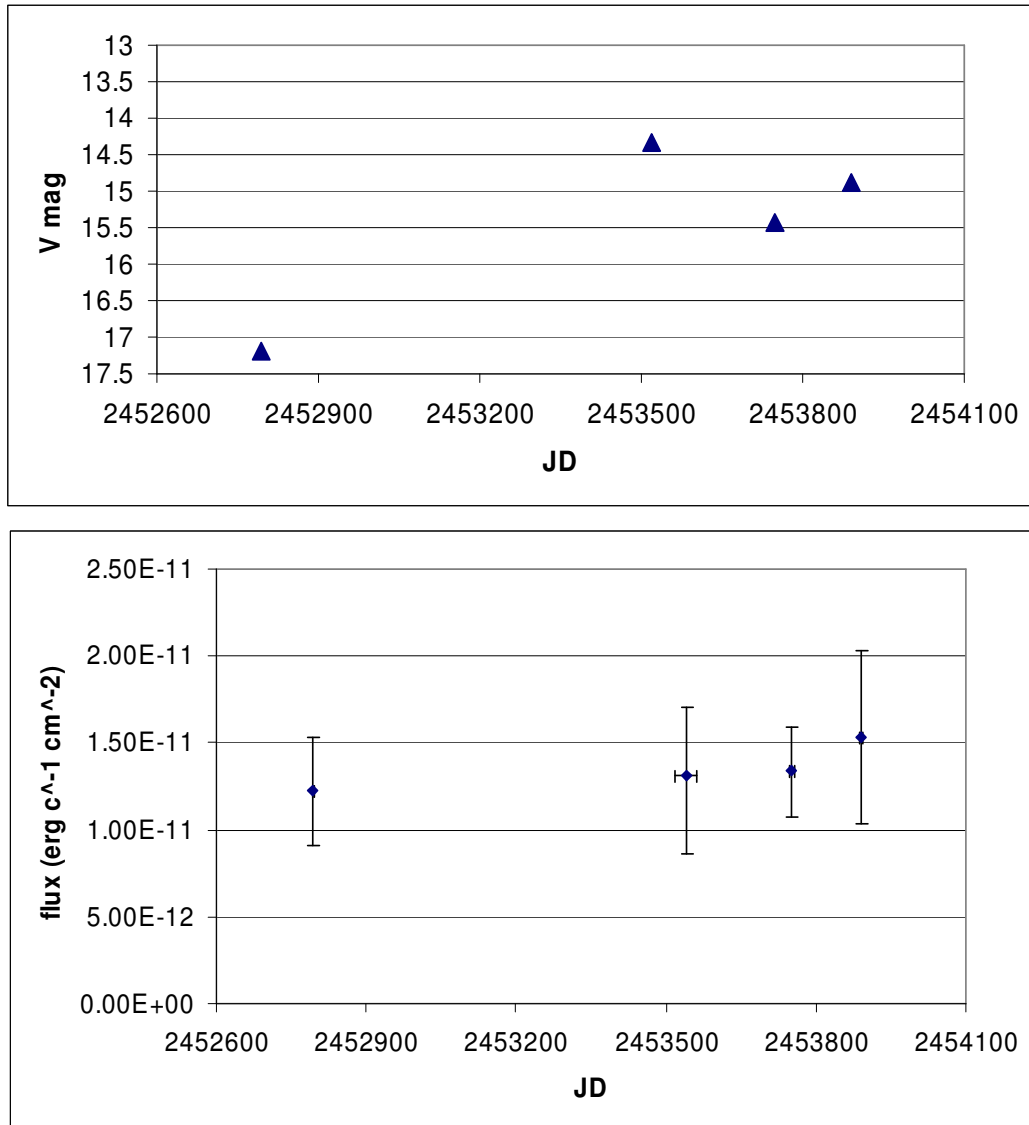


Fig. 5. Light curves in the optical V-band (top) and the ISGRI 20 - 60 keV hard X-ray band (bottom) during the four observational periods.

While the hard X-ray (20-60 keV) fluxes are rather constant, the optical V-

band shows significant variability. This becomes even more obvious by correlating the two bands (Fig. 6). While the V-band magnitude covers a range from 14.3 to about 17.2 mag, i.e. a flux variation of about a factor of 15, the hard X-rays remain constant. This result clearly shows that there is no simultaneous variability between the two bands. The two bands seem to be uncorrelated.

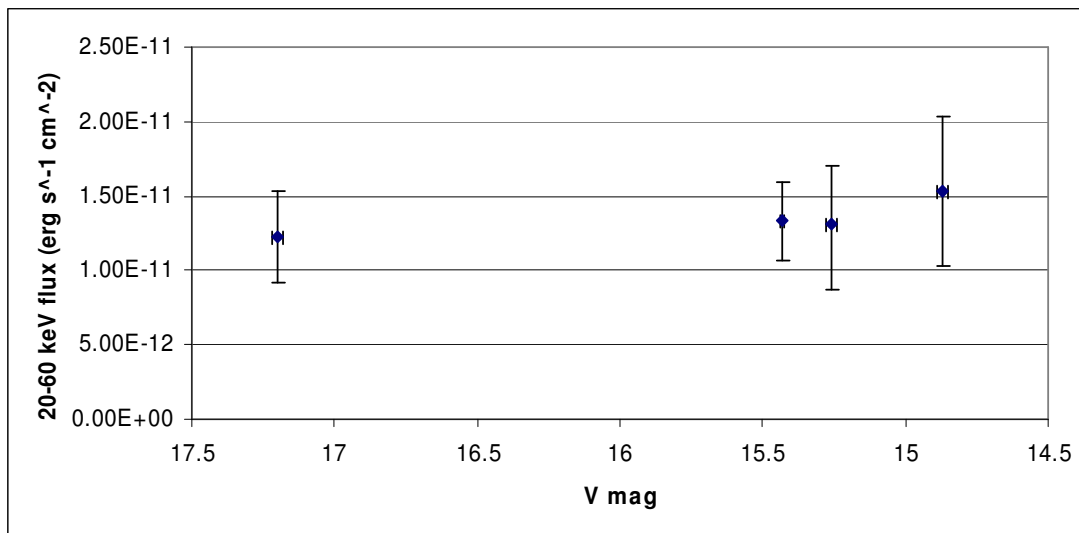


Fig. 6. The hard X-ray flux is plotted against the V- band magnitude obtained from simultaneous observations with ISGRI and OMC, or by optical telescopes for June 2003. The two bands do not show a correlation.

4.1.5 Discussion

As mentioned earlier, 3C 279 shows the typical two-hump broadband SED, interpreted as non-thermal synchrotron and IC emission emanating from a relativistic jet. Most detailed blazar emission models have been developed within this scenario. While the synchrotron emission is generally understood, the detailed nature of the IC emission remains unclear. For example, it is not agreed on whether hadronic or leptonic processes dominate. If leptonic processes dominate, it is still unclear whether the leptons upscatter the synchrotron jet photons

themselves, which is called the synchrotron self-Compton (SSC) mechanism ([7],[8]), or whether photons external to the jet (e.g. from an accretion disk are upscattered to higher energies ([9],[10])). The latter models are called EC (external Comptonization) models. Since all these processes are physically possible, it might be that a combination of processes contributes to the IC emission of blazars. Such a multi-component modeling was applied to describe the multifrequency emission of 3C 279 [11]. According to this modeling the low-energy IC emission (X- and hard X-rays) is dominated by the SSC component, while the γ -rays ($\geq 1\text{MeV}$) are predominantly due to Comptonization of photons external to the jet.

We have studied the hard X-ray emission of 3C 279 during the INTEGRAL mission. We find that over 4 observational periods, the hard X-ray flux (20 - 60 keV) is nearly constant. By considering the error bars on the flux values, 3C 279 is varying within a factor of two at most (Fig. 5). In contrast to the hard X-ray band, we find - by analyzing the INTEGRAL OMC data or by taking values from the literature - significant variability in the optical V-band for the same observational periods. Variability changes between 14.3 and 17.2 mag correspond to flux changes of a factor of 14.5. Fig. 6 shows, that in spite of these large optical flux changes, the hard X-ray flux remains constant, showing that the two spectral bands are not correlated. This result means that the optical flux cannot be used as tracer to estimate the level of the hard X-rays. By assuming a leptonic emission scenario, our result - the non-correlation between optical and hard X-rays - is consistent with and therefore supports the suggestion that in 3C 279 the X- and hard X-rays are SSC emission. In simple SSC models, the IC spectrum follows to first order the shape of the curved synchrotron spectrum, just shifted to higher energies. A significant change in the optical band, being at the high-energy synchrotron part, should then have its "IC counterpart" at the higher IC energies, i.e. above the hard X-rays, e.g. at MeV or GeV energies.

REFERENCES:

- 1) Hartman R. C., et al. 1999, ApJ, 123, 79
- 2) Impey, C. D., & Tapia, S. 1990, ApJ, 354, 124
- 3) Urry, C. M. & Padovani, P. 1995, PASP, 107, 803
- 4) Koenigl, A. 1981, ApJ, 243, 700
- 5) Collmar W., et al. 2004, Proceedings of the 5th INTEGRAL Workshop on the INTEGRAL Universe ESA Publication Division, SP-552

- 6) Collmar, W., et al. 2007, Proceeding of the 6th INTEGRAL Workshop on the INTEGRAL Universe ESA Publication Division, SP-622
- 7) Maraschi, L., Ghisellini, G., & Celotti, A. 1992, ApJ, 397, L5
- 8) Bloom S. D., & Marscher, A. P. 1996, ApJ, 461, 657
- 9) Dermer, C.D., & Schlickeiser, R. 1993, ApJ, 416, 458
- 10) Sikora, M., et al. 1994, ApJ, 421, 153
- 11) Hartman R.C., et al. 2001, ApJ 553, 683

4.2 PKS 0537-286, the high red-shift FSRQ, giving new insights into the jet physics

4.2.1 Introduction

We have performed a multiwavelength campaign within five different epochs on the high red-shift FSRQ PKS 0537-286 during October - November 2006 and February 2008. The automatic optical and near-infrared telescope (REM) and the Gamma-Ray Burst Optical and Near Infrared Detector (GROND) observed the source simultaneously to X-ray satellite pointings that allowed covering a wide range of energies. At X-ray energies no variability was found. The Swift/BAT light curve over two years of survey showed a constant flux level. We confirm the soft X-ray excess absorption already mentioned in a number of previous observations (Cappi et al., 1997; Fiore et al., 1998; Reeves et al., 2001; Sambruna et al., 2007). Our studies focus on the spectral flattening, common to the high red-shift FSRQ.

The source is thought to be the EGRET 3EG J0531-2940 counterpart (Sambruna et al., 2007). Due a viable emission mechanism we can confirm the source as counterpart.

The sampled spectral energy distribution is explained in a synchrotron and inverse-Compton emission mechanism. This foresees the plasma within the jet to emit when shocks are formed, giving rise to the internal shock scenario. We derived the physical parameters associated to the simulated spectral energy distribution of the source.

The spectral energy distribution (SED) of blazars is dominated by non-thermal continuum. The relativistic jets producing this typical two hump structure from radio to gamma-rays and sometimes to TeV band (Fossati et al., 1998) extend over kparsec scale. According to whether they are observed edge-on or face-on they give rise to radio galaxies or blazar objects (Urry & Padovani, 1995). Within this framework multiwavelength studies of blazars give a unique insight into the jet physics due to emission enhancement through relativistic aberration. These observations over several decades of energy bands started to be carried out more than ten years ago and lead to different emission models. But still the question, on how the central super massive black hole (SMBH) transfers its gravitational energy to the relativistic moving plasma, is asking to be solved.

The overall blazar emission is successfully interpreted in the view of the synchrotron inverse-Compton models. The first peak at lower energies is unequivocally dominated by synchrotron radiation from radio to UV/X domain (Blandford et al., 1978). This view is supported by the polarized radio emission (Piner et al., 2005). At higher energies, the second component is due to inverse Compton scattering by the same electron population (Ghisellini et al., 1998) producing the photons, although alternative scenarios have been proposed (Koenigl, 1981). The prevailing picture of the emission mechanism foresees the emitting plasma to be accelerated within the jet. Cooling and acceleration of these relativistic particles leads to variability in the measured spectrum caused by shocks within the jet. In this scenario also the external components (Dermer et al., 1992) to the jet, like the accretion disk surrounding the central SMBH, play a fundamental role, injecting external seed photons scattered by the broad line region into the jet.

The importance of high red-shift blazars is related to the evolution studies of SMBH in the early Universe. Their high energy spectral properties make them suitable candidates for the recently launched GLAST gamma-ray mission and thus ideal targets for further probe of gamma-ray horizon (Stecker et al., 2006). The diffuse extragalactic background light (EBL), consisting of the sum of starlight emitted by galaxies through the history of the Universe, leads to attenuation via pair production of the sources' gamma-rays originating within the jet, while propagating to the Earth. The resulting effect of the attenuation is visible in the gamma-ray spectrum as a high-energy cut-off (Stecker et al., 2006). But the opacity due to pair production caused by external radiation field within the AGN system (local opacity), results in a contribution to the effective opacity, which is the sum of the EBL-caused opacity and the local opacity. Following the progress in recent black hole demographics, Reimer (2007) demonstrates that for positively evolving and non-evolving accretion rates over cosmological time, the local opacity shows a red-shift-dependence with larger opacity from sources at higher redshift. Ambiguities in the interpretation of blazar spectral absorption features are the consequences. It is key to disentangle the two components for the estimation of EBL, which carries the information of primordial star formation rate. To this end the precisely measured spectra and their shape can give hints to the underlying physical processes.

For high red-shift quasars, the X-ray and hard X-ray spectrum is of particular interest. It covers the rising component all the way up to the IC-peak of the ν - F_ν plot. Thus, it is key for the completion of the SED and therefore the determination

of the physical parameters that can be derived from simulations (Tavecchio et al., 2000). In the soft X-ray range an excess absorption compared to the galactic values has been confirmed for high red-shift blazars (Yuan et al., 2005; Worsley et al., 2004). The spectra of these sources are well represented by absorption features at soft X-ray frequencies and a hard spectral index. Spectral flattening has been confirmed in a number of studies of high red-shift radio-loud quasars (Fiore et al., 1998; Reeve & Turner, 2000), which found this spectral feature to be systematic in high red-shift FSRQ.

Multiwavelength campaigns are carried out in order to cover the complete emission domain of blazars. The INTEGRAL (Winkle et al., 2003) and Swift (Gherels et al., 2004) satellites carry ideal experiments for this purpose, the latter being very easy to schedule and the former one performing long pointings on single objects. Both satellites' energy ranges extend over a large interval of frequencies, allowing to simultaneously observing the pointed objects at different wavelengths.

We report here on a multiwavelength campaign carried out in 5 different epoches on PKS 0537-286, focusing on X-ray and hard X-ray spectral analysis. The SED is compiled and physical parameters derived.

4.2.2 The source

PKS 0537-286, at $z = 3.104$ (Wright et al., 1978), is one of the most luminous known high red-shift quasar. First detected at radio frequencies (Bolton et al., 1975), it was observed at X-rays by the Einstein observatory (Zamorani et al., 1981) and then studied with ASCA (Cappi et al., 1997; Siebert et al., 1996), ROSAT (Fiore et al., 1998), XMM (Reeves et al., 2001) and Swift (Sambruna et al., 2007). These observations showed an extremely luminous quasar ($L_x = 10^{47}$ erg s⁻¹ in the 0.1 - 2 keV range). A further characteristic is its particularly hard spectrum and a weak iron K emission and reflection features. Moreover Sowards-Emmerd et al. (2004) identified PKS 0537-286 as probable counterpart of the EGRET source 3EG J0531-2940.

4.2.3 Observations

The source was proposed to be monitored by INTEGRAL. Due to the fact that the Swift/BAT light curve over 9 months of exposure (Ajello et al., 2008) was consistent with a constant flux level, the INTEGRAL pointings were proposed in

non-contiguous time intervals. In the 3 - 20 keV band, PKS 0537-286 was observed simultaneously with the RXTE All Sky Monitor on November 1st 2006. During the same epoch REM observations performed photometry in 5 optical energy bands (V, R, J, I, H). In order to better cover the X-ray range and simultaneously obtain UV-data we requested a Swift ToO. This was scheduled on October 27th, 30th, 31st 2006 and further Swift/XRT observations were done on February 10th, 12th 2008.

We monitored the source in several occasions. At X-rays, five Swift/XRT pointings, one INTEGRAL/ISGRI monitoring (on several epochs) and one RXTE observation were performed. Simultaneously optical to UV observations respectively with REM/GROND and Swift/UVOT were carried out. Details of the multiwavelength campaigns can be found in tables 1, 2, 3, 4, 5 and 6.

Date (UTC)	Band	Mag	Error mag
2008-02-14 02:11:05	g'	19.40	0.07
2008-02-14 02:11:05	r'	18.89	0.07
2008-02-14 02:11:05	i'	18.89	0.06
2008-02-14 05:21:55	g'	19.44	0.07
2008-02-14 05:21:55	r'	18.79	0.07
2008-02-14 05:21:55	i'	18.98	0.05

Table 1: GROND observation log.

Date (UTC)	Band	Mag	Error mag
2006-10-18 04:51:14	V	18.25	0.08
2006-10-28 03:22:58	V	18.83	0.18
2006-10-30 05:59:53	V	18.5	0.08
2006-10-31 05:24:10	V	18.46	0.1
2006-11-01 06:10:36	V	18.39	0.09
2006-10-18 05:46:48	R	17.67	0.08

2006-10-28 04:18:33	R	17.93	0.09
2006-10-30 04:10:12	R	18.36	0.12
2006-10-31 06:17:09	R	18.55	0.09
2006-11-01 06:59:38	R	18.48	0.1
2006-10-18 06:42:21	I	17.15	0.09
2006-10-30 05:05:47	I	17.74	0.12
2006-10-31 05:01:54	I	17.77	0.13
2006-11-01 05:41:47	I	17.77	0.11
2006-10-18 04:25:24	J	17.05	0.18
2006-10-28 02:57:07	J	17.68	0.2
2006-10-30 04:44:01	J	17.66	0.17
2006-10-31 04:08:18	J	17.65	0.14
2006-11-01 04:26:12	J	17.73	0.14
2006-10-18 05:25:28	H	16.43	0.16
2006-10-28 03:57:10	H	16.77	0.14
2006-10-30 03:48:58	H	17.41	0.11
2006-10-31 05:13:25	H	17.1	0.08
2006-11-01 05:52:46	H	17.25	0.14

Table 2: REM observation log.

Start Date (UTC)	Band	Exp (ksec)	Flux ^a
2006-10-27 05:55:46	U	1.007	4.6±1.0
2006-10-30 06:15:23	U	1.090	5.9±1.0
2006-10-31 06:21:27	U	1.084	4.2±1.0
2008-02-10 16:22:46	U	0.484	5.6±1.2
2008-02-12 16:24:40	U	0.925	3.9±1.1

Table 3: UVOT observation log. ^a in units of 10^{-14} erg cm⁻² s⁻¹.

Start Date (UTC)	Exp (ksec)	flux	Error mag
2006-11-01 00:06:40	7.2	19.40	0.07

Table 4: RXTE observation log.

INTEGRAL Rev.	Start date (UTC)	End date (UTC)	Exp (sec)
0493	2006-10-26 23:31:06	2006-10-29 04:19:28	180423
0494	2006-10-29 22:36:24	2006-11-01 12:51:01	202377
0549	2007-04-12 23:33:26	2007-04-15 03:02:26	170054
0550	2007-04-15 17:04:49	2007-04-18 01:32:37	188714
0552	2007-04-22 07:17:30	2007-02-24 01:23:05	136084
0558	2007-05-09 11:34:04	2007-05-10 21:03:40	115482

Table 5: ISGRI observation log.

Start Date (UTC)	Exp (ksec)
2006-10-27 05:55:53	3.0
2006-10-30 06:15:21	3.8
2006-10-31 06:21:26	3.4
2008-02-10 16:22:48	6.7
2008-02-12 16:24:38	5.2

Table 6: Swift/XRT observation log.

4.2.3.1 X-ray observations

The INTEGRAL satellite observed the source with its imager IBIS/ISGRI (Lebrun et al., 2003) which operates in the range 17 - 1000 keV. The long exposure of 1 Ms was carried out in non-consecutive pointings. These observations were performed with a hexagonal dithering pattern. By instrument design, only few dither pointings produced a useful JEM-X spectrum of the source being off-axis for most of the time. This leads to an effective observation time of 69% for JEM-X which did not detect the source. The source is only marginally detected with ISGRI in the 17 - 55 keV band. We used OSA 6.0 software for the ISGRI analysis. Using the detected count rate we performed data cleaning. Most recent matrices available for standard software (`isgri_arf_rsp_0019.fits`) were used for spectral analysis. We used 296 science windows for a total amount of 981 ksec of exposure time on the source. The source is detected with ISGRI with a significance of 5.6 sigma. Data screening was performed according to the median count rate with respect to each science window and its distribution. Due to the low detection level a spectrum cannot be fitted.

The Burst-Alert Telescope (BAT, Barthelmy et al., 2005) on board the Swift satellite is a coded-mask telescope operating in the 15 - 200 keV energy range. Thanks to its large field of view, BAT surveys up to 80% of the sky every day. We selected all observations comprised in the time span January 2005 - March 2007. The data were processed using HEASOFT 6.3 and following the recipes presented in Ajello et al. (2008b). The spectrum and the light curve of PKS 0537-286 were extracted using the method presented in Ajello et al. (2008).

RXTE observed PKS 0537-286 for 9.9 ksec, starting on 2006 October 28. We reduced the data using the standard reduction script REX included in the HEASOFT6.0.4 package. The analysis was restricted to standard 2 binned data of layer 1 of the Proportional Counting Unit 2 (PCU2) of the Proportional Counter Array (PCA) from 3 - 20 keV. We used PCARSP to produce the response matrix for the dataset.

The X-Ray Telescope (Burrows et al., 2005) on board Swift observed the blazar in October 2006 and February 2008. The monitoring campaign was carried out within five observations. Data processing, screening and filtering were done using the FTOOL *xrtpipeline* comprised in the HEASOFT 6.3 distribution.

4.2.3.2 Optical to UV observations

PKS 0537-286 was targeted in the U-band with the UV-Optical Telescope UVOT (Roming et al., 2005) onboard the Swift satellite. Observations were performed in three epochs in 2006 October and two epochs in 2008 February. Here, we use the standard pipeline reduced image products, co-added and exposure corrected within the <http://heasarc.gsfc.nasa.gov/docs/xanadu/ximage/ximage.html> environment. Flux densities are corrected for Galactic foreground extinction (Schlegel et al., 1998).

Photometry data were acquired by the Rapid Eye Mount (REM) (Chincarini et al., 2003) in October and November 2006, using different filters. The log is reported in table 2. The light curve (figure 2) shows a nearly constant behavior over the monitoring period.

The Gamma-Ray Burst Optical and Near Infrared Detector (GROND) is a 7-channels imager primarily designed for fast follow-up observations of GRB afterglows (Greiner et al., 2008). Due to the use of dichroic beam splitters it is capable of simultaneous imaging in seven bands, g' r' i' z' (similar to the Sloan system) and J H K (400 nm - 2310 nm). GROND is mounted on the 2.2 m ESO/MPI telescope on LaSilla/Chile since April 2007.

4.2.4 Timing analysis

The optical light curves obtained with REM and GROND do not show significant variations (see figure 2 and 3). Whenever, if at a given date, more than one REM or GROND measurement is available, then the average flux is taken. It has to be accounted that the source was during optical photometry close to the horizon. Thus, some uncertainty cannot be avoided. Within each individual Swift/XRT pointing no evidence of flux variation in the XRT spectrum was found. Among the five pointings, the flux stayed basically constant within the error bars (table 6). The BAT light curve is consistent with being constant over 2 two years of survey (see figure 1).

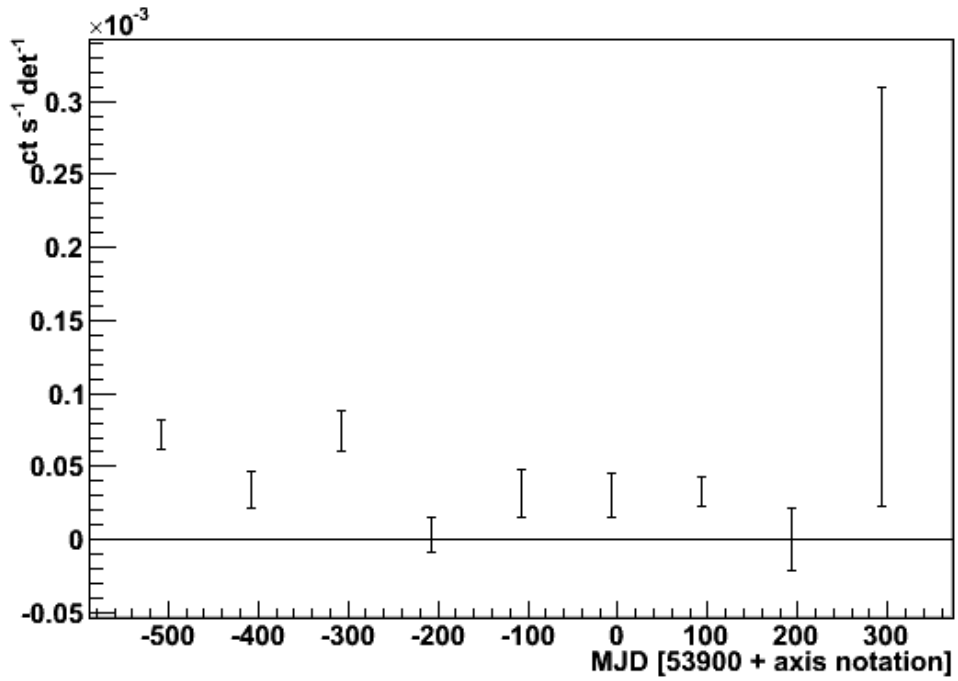


Figure 1: The Swift/BAT lightcurve obtained due to two years of survey.

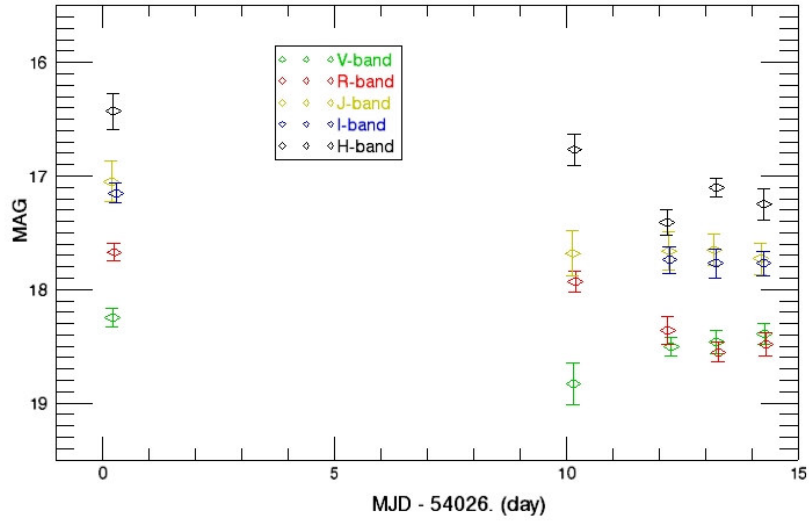


Figure 2: The REM lightcurve shows nearly constant flux over the whole observation period.

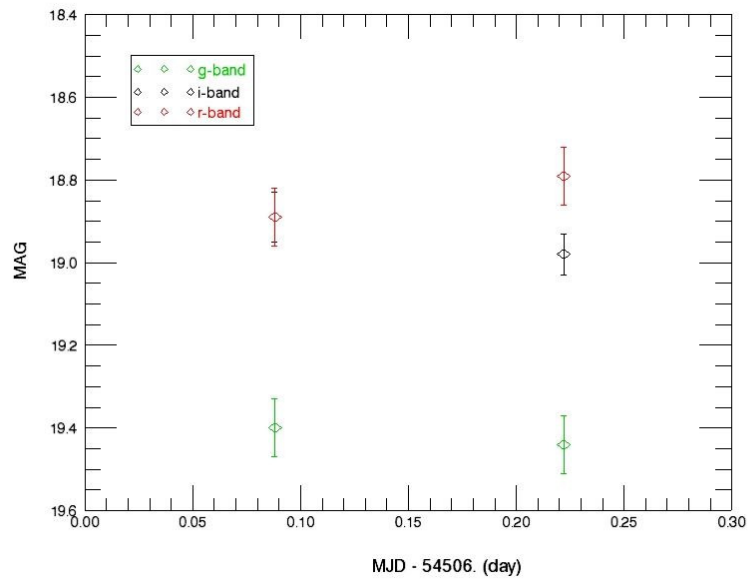


Figure 3: The GROND lightcurve shows no variability of the source.

4.2.5 X-ray and hard X-ray spectra

4.2.5.1 Single spectra

The fit results of single spectra as well as the combined X-ray and hard X-ray fit are shown in table 7 which summarizes all results. The spectra were fitted using XSPEC 12 and the latest available response matrices from calibration.

Swift/BAT detected, in the 15 - 150 keV range, PKS 0537-286 with a flux of $\sim 6 \times 10^{-11}$ erg cm $^{-2}$ s $^{-1}$ during the two years of the survey. The BAT light curve is consistent with being constant. The spectrum is exceptionally hard and it can be modeled as a power law with photon index of 1.1 - 1.2. No foreground absorption features were taken in account since at these energies the small column densities are negligible.

The single XRT spectral fit are shown in table 7. In the energy range between 0.3 - 10 keV we find evidence for absorption in excess of the Galactic value (at about 1 keV). The lower limit on the N_{H} -value is 5.3×10^{20} cm $^{-2}$, that is well above the Galactic value of 2.0×10^{20} cm $^{-2}$. The absorbed powerlaw gives the best result in terms of chi-square.

Since the lower limit of the energy range is around 2 keV the above mentioned absorption features present in XRT, cannot be detected in RXTE. Therefore these data are well represented by a simple powerlaw.

Ins	model	N_{H}^{a}	Γ	norm $^{\text{b}}$	flux $^{\text{c}}$
XRT	abs pwrlw	0.13 ± 0.10	1.5 ± 0.2	4.7 ± 1.3	$2.5_{1.8}^{3.1}$
XRT	abs pwrlw	0.22 ± 0.05	2.0 ± 0.1	8.6 ± 1.6	$2.1_{1.8}^{2.4}$
XRT	abs pwrlw	0.17 ± 0.06	1.7 ± 0.1	6.3 ± 1.3	$2.3_{1.9}^{2.5}$
XRT	abs pwrlw	0.12 ± 0.04	1.5 ± 0.1	5.3 ± 0.8	$2.6_{2.8}^{2.9}$
XRT	abs pwrlw	0.12 ± 0.06	1.4 ± 0.1	4.4 ± 0.8	$2.6_{2.3}^{2.9}$
RXTE	pwrlw		1.3 ± 0.2	0.05 ± 0.04	$0.04_{0.03}^{0.05}$
BAT	pwrlw		1.2 ± 0.3	0.3 ± 0.1	$0.6_{0.4}^{0.7}$

Table 7: Fit result of single X-ray spectra. $^{\text{a}}$ in units of 10^{22} cm $^{-2}$, $^{\text{b}}$ in units of 10^{-2} counts s $^{-1}$ keV $^{-1}$, $^{\text{c}}$ in units of 10^{-10} erg cm $^{-2}$ s $^{-1}$ (2 - 10 keV for XRT, 3 - 15 keV for RXTE, 15 - 150 keV for BAT).

4.2.5.2 Joint X-ray and hard X-ray spectra

None of the X-ray and hard X-ray observations showed flux variability. We therefore fitted all the spectra simultaneously. All fit results are listed in table 8. The aim is to obtain the best sampled spectrum (and thus statistics) and detect possible spectral features. Indeed a systematic spectral flattening of high red-shift blazars was found (Fiore et al., 1998; Reeves & Turner, 2000). Here we account that flattening in the X-ray spectrum reveals the presence of emission via bulk Comptonization. In order to find a possible Compton bump we add a blackbody component to the absorbed powerlaw model. Having a look at the residuals in figure 5, it is worth noticing how the fit produces much better residuals for RXTE and BAT data points. This is exactly at energies where this effect is predicted by Celotti et al. (2007). A further interpretation of the bulk motion Comptonization is given by Titarchuk et al. (1997) whose model is self-consistent bulk motion Comptonization rather than the sum of two components like powerlaw and black body. We fitted therefore the BMC-model to the data gaining a reduced chi-square of 0.9. Table 8 the results of the fit described in this paragraph.

Model	N_H^a	Γ	BB ^b	norm pw ^c	norm BB ^d	Log(A) ^e	α^f	norm ^g	kT ^e
abs pwrlw	0.05±0.01	1.3±0.3		4.2±0.4					
abs pwrlw+BB	0.07±0.2	1.3±0.6	8.6±1.8	4.4±0.6	0.4±0.7				
BMC						0.25±0.05	0.27±0.04	2.5±1.0	0.25±0.05

Table 8: Joint fit results of all X-ray and hard X-ray spectra with different models. ^a in units of 10^{22} cm⁻², ^b in units of keV, ^c in units of 10^{-4} counts s⁻¹ keV⁻¹, ^d in units of 10^{-4} counts s⁻¹ keV⁻¹.

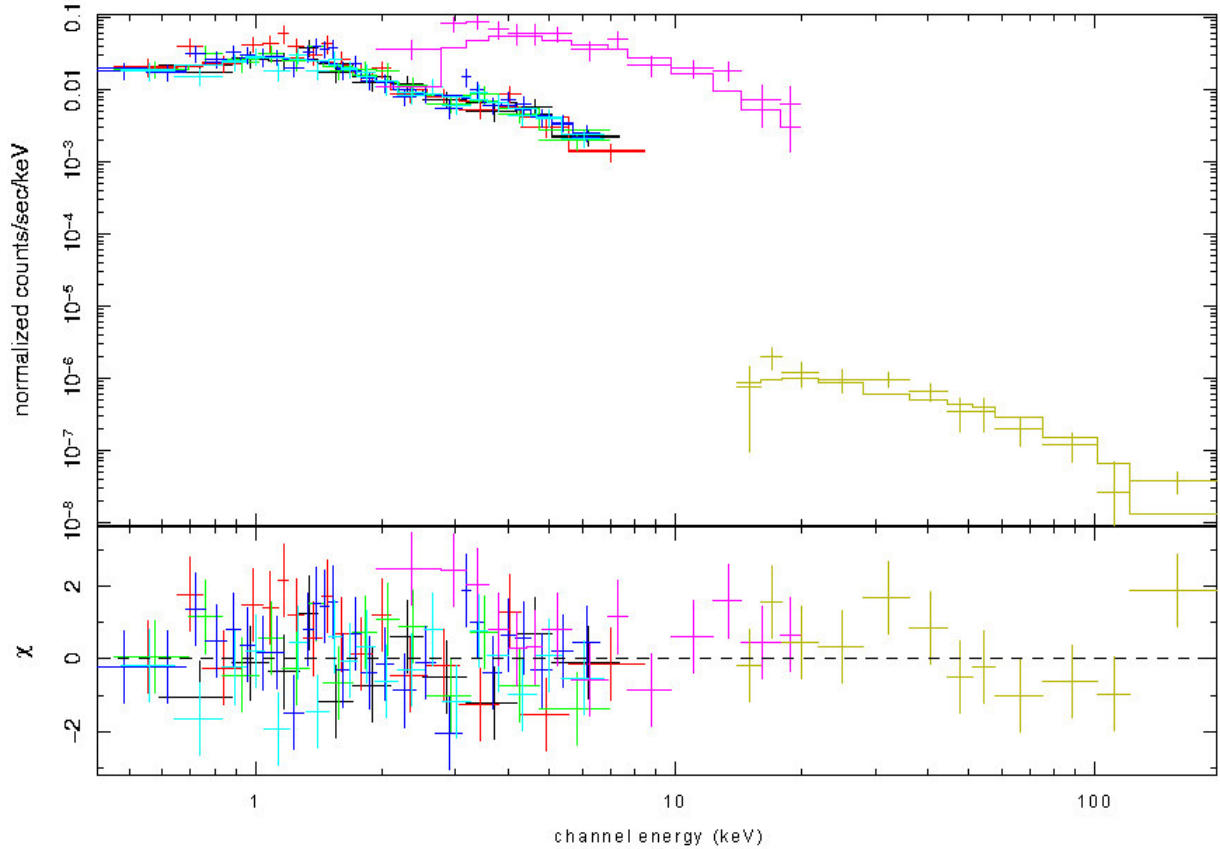


Figure 4: The joint spectrum of all X-ray and hard X-ray spectra from our multiwavelength campaigns. The fit to the data points is an absorbed powerlaw of spectral index 1.3 (see table 8 for all parameters) gaining a reduced chi-square of 0.9.

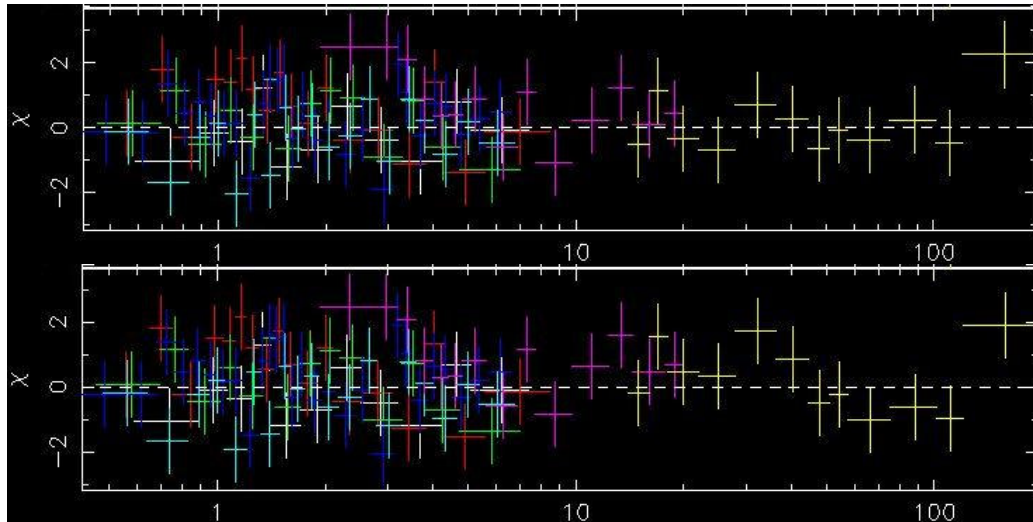


Figure 5: The comparison between the residuals obtained with an absorbed powerlaw+BB model (upper panel) and a simple absorbed powerlaw model (lower panel) is shown. It is apparent that in the former case the residuals of RXTE and BAT data are much better compared to that obtained by the simple absorbed powerlaw.

4.2.6 Spectral energy distribution

4.2.6.1 Data

The source was pointed five times by Swift/XRT. During these observations photometry at longer wavelength was carried out. EGRET detected the blazar only in two energy bins. The data points plotted in the SED (figure 6) represent the modeled spectrum as could have been obtained by EGRET in the GeV range. Thus we can show 5 SEDs and derive the parameters which model the data points. PKS 0537-286 belongs to the FSRQ subclass of blazars. Its optical spectra are dominated by broad emission lines. It must be noted the sharp steepening in the optical-UV continuum. The shape of the optical data points obtained with REM and GROND is in good agreement. There is a slightly offset suggesting that the source faded in the optical band. The typical two hump structure is evident in all SEDs.

The IC-peak can be constrained by the BAT and EGRET spectra to lay at around few GeV.

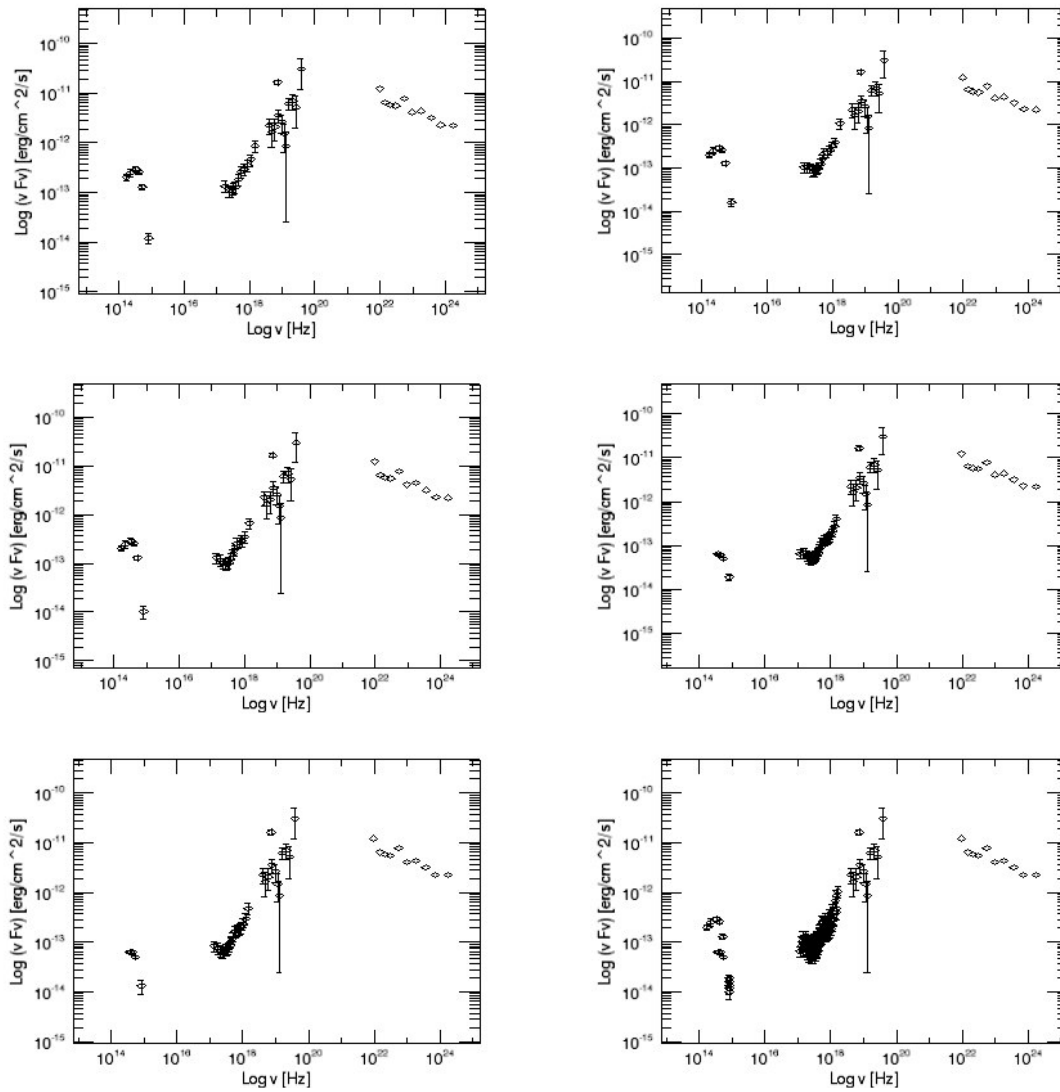


Figure 6: This figure shows the five simultaneous SEDs obtained observing PKS 0537-286 from optical to hard X-rays. The lower right corner contains the SED using all our available data.

The synchrotron peak is somewhat difficult to determine. The sharp cut-off in the optical-UV continuum suggests a thermal component in its origin. This makes the effort to exactly determine the synchrotron peak elusive.

4.2.6.2 SED modeling

I model the data according to Ghisellini et al. (2002), assuming a one-zone, homogeneous synchrotron and inverse-Compton model. The ejecta move within the jet seen under an angle θ and bulk Lorentz factor Γ . The homogeneous magnetic field is tangled throughout the region. The emitting region is a cylinder having width $\Delta R' \approx R/\Gamma$, in the co-moving frame, and radius R being the jet's cross section. A basic assumption is a finite injection time t_{inj} , that lasts for $t_{inj} = \Delta R'/c$. The equation describing the particle distribution has no steady state solution. However considering the particle distribution at the time t_{inj} , this shows a good representation of the observed spectrum since variable sources are studied. The emitted luminosity in fact is maximized at the end of the injection.

The broad line region (BLR) clouds reprocess the external radiation field. This component is approximated to a black body radiation with luminosity L_d produced at the distance of the broad line region R_{BLR} . L'_{int} is the luminosity of injected relativistic electrons which distribution is given by the injection and cooling processes. Assuming the injection to last for a finite timescale, only the higher energy particles have the time to cool and radiate. Thus, the particle distribution is described by a broken power law with a steep part above the break energy and the original injection slope s below. Defining γ_c as the energy of those electrons able to cool in the t_{inj} , there are different particle distributions $N(\gamma)$ having different slopes depending on the y_{min} and y_{max} . A full description of the model can be found in Ghisellini et al. (2002).

We modeled the first and the fourth observation epoches which show the largest variation from optical to X-ray band. Using the upper limit obtained by EGRET, the IC peak was assumed to be between this limit and the Swift/BAT. The results are shown in figure 7 (solid green and black lines). The assumed parameters are reported in tabel 9. GROND data could not be modeled (see paragraph 4.2.7.1). Even though very small variability in X-rays, the only parameter changing over the two observation epoches is related to the particle distribution.

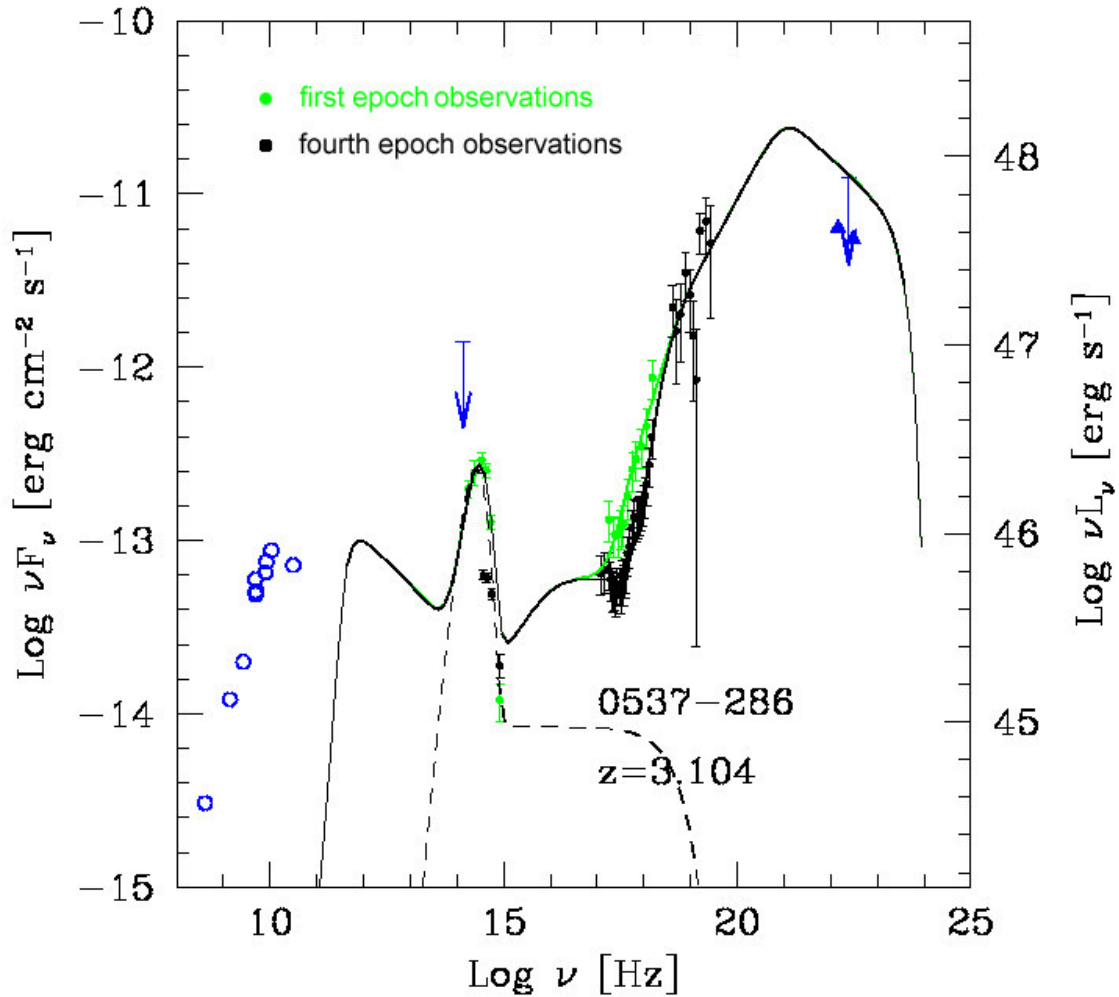


Figure 7: The SED model as described in Ghisellini et al. (2002). The green data points correspond to the first observation epoch (REM + Swift/UVOT + Swift/XRT). Black data points are obtained during the fourth epoch (GROND + Swift/UVOT + Swift/XRT). For most of the fitted data points the continuum green and black lines are superimposed. GROND data points could not be modeled and this remains an open question (see also discussion of optical data in paragraph 4.2.7.1).

R [cm]	Γ	Θ [deg]	B [G]	L'_{inj} [erg s ⁻¹]	γ_{min}	γ_{max}	s	L_d [erg s ⁻¹]	R_{BLR} [cm]
$2 \cdot 10^{16}$	15	3.0	2.3	$1.3 \cdot 10^{44}$	20	10^4	3.0	$5 \cdot 10^{46}$	$4.5 \cdot 10^{17}$
$2 \cdot 10^{16}$	15	3.0	2.2	$1.3 \cdot 10^{44}$	25	10^4	3.0	$5 \cdot 10^{46}$	$4.5 \cdot 10^{17}$

Table 9: Parameters derived from the SED modeling. R = radius emitting region, Γ = Bulk Lorentz factor, Θ = viewed angle, B = magnetic field, L'_{inj} = luminosity of injected relativistic electrons, γ_{min} = minimum Lorentz factor of injected electrons, γ_{max} = maximum Lorentz factor of injected electrons, s = spectral slope of injected electrons, L_d = disk luminosity, R_{BLR} = BLR radius.

4.2.7 Discussion

4.2.7.1 Optical data

It is worth noticing the flux gap between REM and GROND data. PKS 0537-286 is at REM's limiting magnitude and the background can relevantly disturb photometry. Nevertheless, the observed flux increase towards longer wavelengths is proportional for the two instruments. This sharp increase is not surprising, as the Lyman alpha emission line is shifted along lower frequencies due to the high red-shift, and an observed continuum discontinuity near 3650 Å. (in the observers frame) associated with an absorption system enhances this feature (Wright et al., 1978). If so, the only open question remains the difference between the two optical datasets, since the behavior of the flux of the Lyman alpha emission line of other FRSQ shows to be constant (Koratkar et al., 1998).

4.2.7.2 X-ray spectra

For the Swift/XRT spectra a power law with a fixed Galactic absorption ($2.0 \times 10^{20} \text{ cm}^{-2}$) yielded an unacceptable fit. Leaving the absorption value to be fitted freely a substantial improvement of the reduced chi-square was obtained. The absorption parameter is in good agreement within the five observations and so

does the spectral index. These results can be clearly seen in figure 8, where the confidence level contours of fitted excess absorption N_H and the spectral index are plotted. It is unlikely that an excess column density is in origin Galactic. It would require a factor ~ 3.5 of increase in the Galactic column density toward the direction of the source. Also the intergalactic origin is highly improbable because the line of sight should intercept several systems having very high column density. The intrinsic absorber hypothesis is much debated. Cold (neutral) and warm (ionized) absorber cannot be disentangled only by X-ray data. Furthermore, the best evidences for warm absorbers, like O absorption edge and Fe M-shell, are down shifted outside our observed range (0.3 - 10 keV) being in the rest frames' energy band within 0.5 - 0.9 keV. The possibility for the warm absorber to give rise to absorption variability (Reeves & Turner, 2000) is not confirmed in our case. The excess absorption, also referred to as spectral flattening, has been reported several times for this source (Cappi et al., 1997; Fiore et al., 1998; Reeves et al., 2001; Sambruna et al., 2007). While Siebert et al. (1996) reveal only upper limits. Spectral flattening for high red-shift FSRQ is shown also by Worsley et al. (2004) and Yuan et al. (2005). Spectral flattening is in agreement with a general behavior seen in a number of high red-shift radio-loud quasars studies (Fiore et al., 1998; Reeves & Turner, 2000) which find this spectral feature to be systematic in high red-shift FSRQ. Therefore the flattening is physically associated to high red-shift FSRQs. It is likely that hard X-rays in blazars can be produced via inverse-Compton scattering of seed photons by relativistic bulk motions within the jet. A theoretical interpretation to this is given by Celotti et al. (2007) who foresee a peaked seed photon energy distribution. The seed photons are expected to arise from the accretion disk surrounding the super massive black hole and are comptonized in the jet. The effect of the bulk Comptonization of the seed photons, arising from the innermost part of the accretion disk and entering directly the jet cone, is unobservable. This is because of the small angle between the disc photons and the outward moving shell. On the other hand, photons reprocessed in the BLR are seen always head-on and therefore blue-shifted. Thus the entire spectrum is the contribution of relativistic Compton and bulk Compton, which can be approximated by the sum of a powerlaw and blackbody components.

Bridging the energy gap between Swift/XRT- and Swift/BAT-data with RXTE, our data are very suitable for the determination of the above mentioned spectral features. Therefore we fitted in addition to an absorbed powerlaw also a black body component gaining an equal good fit result as previously but with better residuals (see table 8). The f-test probability of 97.2% confirms the additional parameter. Figure 5 shows the comparison between residuals of the fit of

absorbed power law + black body and simple absorbed power law. The seed photon temperature of 8.6 keV is in good agreement with the predicted one by the authors of the earlier mentioned paper. A further model describing bulk Comptonization motion is given by Titarchuk et al. (1997) whose model is self-consistent bulk motion Comptonization rather than the sum of two components (as done previously). Again we obtained a good fit with reduced chi-square of 0.9 (see table 8) by fitting the BMC-model. The seed photon temperature of 0.2 keV is in good agreement with the one predicted considering a geometrically thin and optically thick accretion disc, having surface temperature (multi-colour black body) profile as in Shakura & Sunyaev (1973). The BMC parameter alpha is related to the spectral index ($\Gamma = 1 + \alpha$) giving the efficiency of Comptonization. A gives the coverage of the seed photon radiation by the Compton medium. The confidence contours of fitted seed photon temperature and alpha are shown at confidence levels of 68%, 90% and 99% (see figure 9). These parameters converge at all levels.

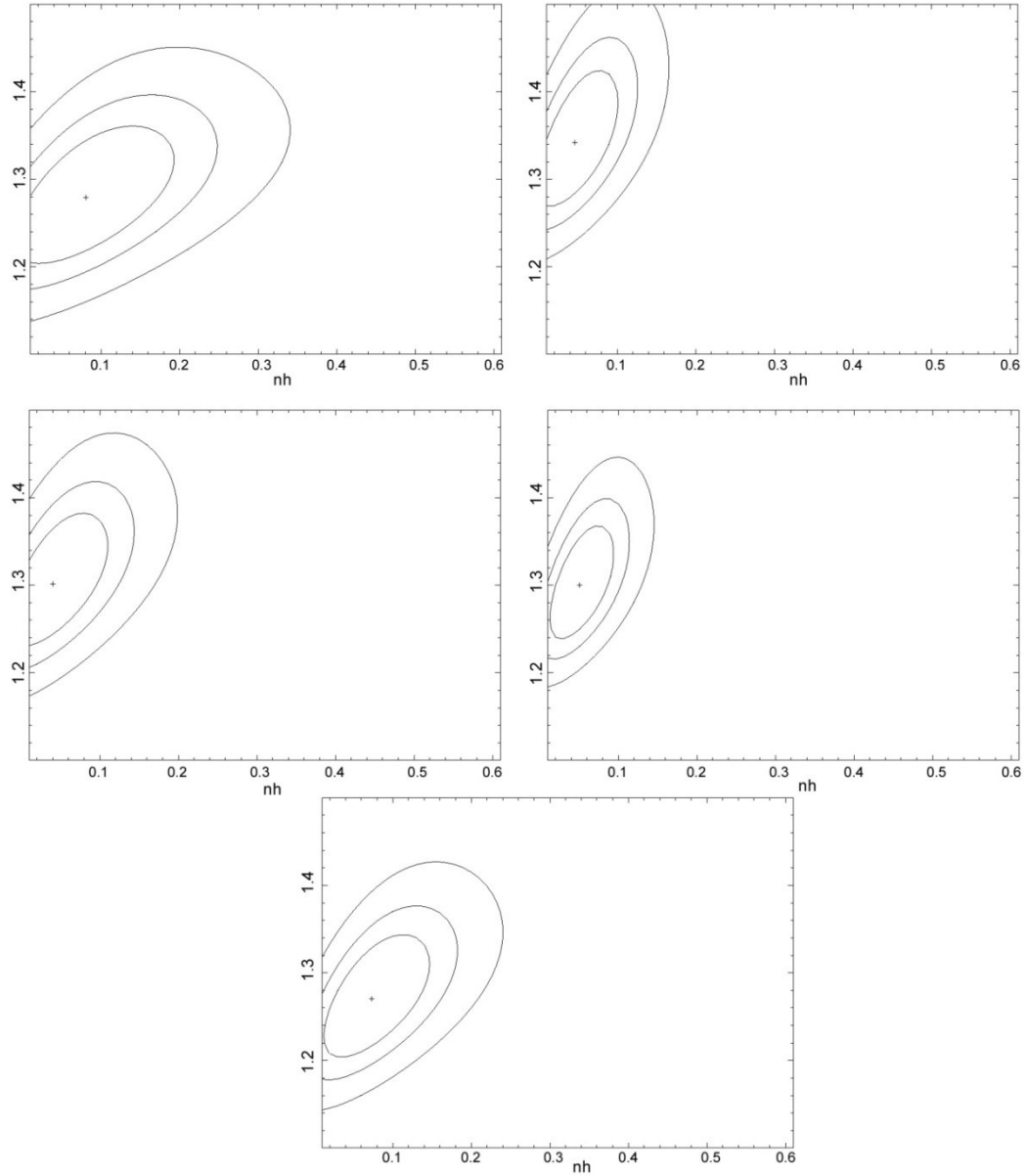


Figure 8: The confidence level contours at 68%, 90% and 99% of the fitted excess absorption and spectral index are shown

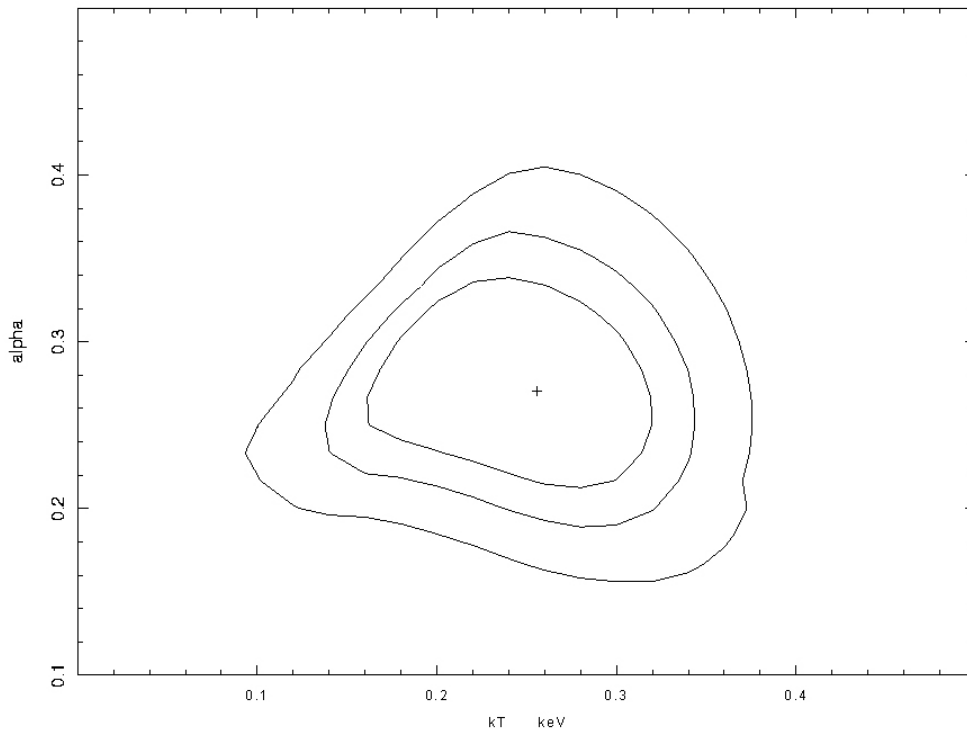


Figure 9: This figure shows the confidence level contours at 68%, 90% and 99% of the parameter kT (indicating the temperature of the seed photons) and α (indicating the efficiency of the Comptonization) of the BMC model (Titarchuk L. et al., 1997). Both parameters converge.

4.2.8 Conclusions

We have conducted a multifrequency campaign on PKS 0537-286 on five different epochs. The source was monitored strictly simultaneously from optical to gamma-rays. At X-rays the source showed very small flux variation between observations on 2006.10.27 and on 2008.02.10, where for the latter pointing the integration time was half of the former one. We show the spectral flattening, characteristic for high red-shift quasars, to be physically associated to the source. The joint X-ray and hard X-ray spectra are fitted to a bulk motion Comptonization

model. Indeed, this model can mimic the flattening toward longer wavelength. Furthermore, we detect spectral X-ray features, related to bulk Comptonization scattering, predicted by Celotti et al. (2007) to be observable for powerful quasars, like PKS 0537-286. Thus, we find the source's jet to be matter dominated. The bulk Comptonization is generally expected to be a transient feature because of the non-continuous plasma injection (or dissipation) into the jet and observed at X-rays in terms of flux variability. But in the case of PKS 0537-286 just little variability is seen in the X-ray spectrum and thus, a more continuous plasma injection must be at work. This finding can have an impact on cosmological evolution of blazars. Indeed, Boettcher and Dermer (2002) proposed that BL Lacs are the final stage of FSRQ where all the material has already been accreted and no gas or dust are left to scatter the external Compton-scattered component. A further hint for this can be the apparent lack of BL Lacs evolution (Padovani et al., 2007). FERMI can confirm this scenario if a decrease in the number density of FSRQ is clearly seen at lower red-shift where the bulk of BL Lacs exists.

REFERENCES:

- Ajello M. et al., 2008, ApJ, 673, 96
- Ajello M. et al., 2008b, ApJ, 678, 102
- Barthelmy S. D. et al., 2005, SSRv, 120, 143
- Blandford R. et al., 1978, in Pittsburgh Conference on BL Lac Objects, ed. A. M. Wolfe, 328
- Bolton, J. G., et al., 1975, Aus. J. Phys. Ap. Suppl. 34, 1
- Boettcher, M., Dermer, C.D., 2002, ApJ, 564, 86
- Burrows D. N. et al., 2005, SSRv., 120, 165
- Cappi M. et al., 1997, ApJ, 478, 492
- Celotti A. et al., 2007, MNRAS, 375, 417
- Chincarini, G. et al. 2003, The Messenger, 113, 40
- Dermer C.D. et al., 1992, A&A, 256, 27
- Fiore F. et al., 1998, ApJ, 492, 79
- Fossati et al., 1998, MNRAS, 299, 433
- Gherels N. et al., 2004, ApJ, 611, 1005
- Ghisellini G. et al., 1998, MNRAS, 301, 451
- Ghisellini G. et al., 2002, A&A, 386, 833
- Greiner J. et al., 2008, PASP, 120, 405
- Koenigl A., 1981, ApJ, 243, 700
- Koratkar A. et al., 1998, ApJ, 492, 173
- Lebrun F. et al., 2003, A&A, 411, 14
- Padovani P. et al., 2007, ApJ, 622, 182
- Piner B. et al., 2005, ApJ, 622, 168
- Reeves J.N. & Turner M.J.L., 2000, MNRAS, 316, 234
- Reeves J.N. et al., 2001, A&A, 365, 116
- Reimer A., 2007, ApJ, 665, 1023
- Roming P.W.A. et al., 2005, Space Science Review, 120, 95
- Sambruna R.M. et al., 2007, ApJ, 669, 884
- Schlegel D.J. et al., 1998, ApJ, 500, 525

- Shakura N.I. & Sunyaev R.A., 1973, A&A, 24, 337
- Siebert J. et al., 1996, A&A, 307, 8
- Sowards-Emmerd D. et al., 2004, ApJ, 609, 564
- Stecker F. W. et al., 2006, ApJ, 648, 774
- Tavecchio F. et al., 2000, ApJ, 543, 535
- Titarchuk L. et al., 1997, ApJ, 487, 834
- Urry C.M. & Padovani P., 1995, PASP, 107, 803
- Winkler C. et al., 2003, A&A, 411, 1
- Worsley M.A. et al., 2004, MNRAS, 350, 67
- Wright A.E. et al., 1978, 226, 61
- Yuan W. et al., 2005, MNRAS, 358, 432
- Zamorani, G., et al., 1981, ApJ, 245, 357

4.3 INTEGRAL observations of the blazar Mrk 421 in outburst

4.3.1 Introduction

If one wants to understand the physics of blazars, better simultaneous observations are important at all wavelengths, so it was fortunate that a ToO observation of the TeV-emitting blazar Mrk 421 with INTEGRAL could be triggered in June 2006 by an increase in the RXTE count rate to more than 30 mCrab. The source was then observed with all INTEGRAL instruments, with the exception of the spectrometer SPI, for a total exposure of 829 ks. During this time several outbursts were observed by IBIS and JEM-X. Multiwavelength observations were immediately triggered, and the source was observed at radio, optical, and X-ray wavelengths up to TeV energies.

The data obtained during these observations were analysed with respect to time variability, time lags, correlated variability, and spectral evolution and then compiled in a ν - F_ν spectrum. The observations of the different instruments/telescopes were analysed with the usual correlation and time-analysis methods. The spectral analysis of the X-ray data was performed with XSPEC.

In 1992 the first AGN, Mrk 421, was detected at energies >500 GeV (Punch et al. 1992). Since then, 20 detections of AGNs have been reported at TeV energies (Blazejowski et al. 2005; Padovani et al. 2007; Wagner 2007). Seventeen of these objects belong to the HBL Lac type of AGNs. They are radioloud sources with the radio emission originating mainly in a core region and they are characterised by a high polarization at radio and optical wavelengths and a strong variability at all wavelengths. The spectral characteristics point to non-thermal emission processes that presumably take place in a narrow relativistic jet pointed at a small angle to the line of sight. The spectral energy-density distribution of these sources shows two smooth broadband emission components: a first one that reaches a broad peak in the IR to X-ray region and a second one at GeV to TeV energies. Both emission components are clearly separated (see Figure 3 of Ghisellini et al. 1996).

It is believed by many researchers that both components are generated by the same leptonic population (electrons and/or positrons) moving at relativistic speed in the jet (Blandford and Rees 1978), which creates the low-energy photons via incoherent synchrotron radiation and the high-energy gamma-rays via inverse-

Compton scattering of soft photons. This common origin would explain the similarity of the two components (Ghisellini and Maraschi 1996); hence, a similar temporal evolution is expected for both components if this scenario is correct. Such time correlations were indeed observed by observations at X-ray and TeV energies (Buckley et al. 1996; Catanese et al. 1997; Fossati et al. 2008), and they even extend to the optical and radio wavelengths (Katarzynski et al. 2003). This idea is further supported by the observed polarization at radio wavelengths (Piner and Edwards 2005). However, there are some exceptions to these clear correlations, such as the orphan TeV flares reported by Blazejowski et al. (2005) and Krawczynski et al. (2004). Unfortunately, measurements between 10 keV and 1 GeV that would allow us to further constrain this common origin have been scarce. Until now only few measurements between 10 keV and 1 GeV exist. COMPTEL has detected Mrk 421 in the 10 - 30 MeV range with 3.2σ (Collmar et al. 1999). EGRET, however, has detected this source many times above 100 MeV (Hartman et al. 1999).

Since the high-energy emission is not as well understood, many different models try to explain this emission component. In one scenario the low-energy synchrotron photons are boosted to high energies by the same electron population that creates the synchrotron photons [the synchrotron self-Compton (SSC) models (Königl 1981, Maraschi et al. 1999, Bloom & Marscher 1996)]. Although this process must be at work in all blazars and if the synchrotron-emission hypothesis is correct, it may not be the dominant one. In another model the seed photons for the inverse-Compton effect enter from outside the jet region, e. g. from the accretion disc or from clouds surrounding the jet (Dermer et al. 1992; Sikora et al. 1994). Apart from these lepton models, the so-called hadron models were proposed in which the high energy γ -rays are produced by proton-initiated cascades (Mannheim 1993, Mücke & Protheroe 2000) and/or protosynchrotron emission (Aharonian 2000; Mücke et al. 2003).

The homogeneous SSC model makes very definite predictions about the correlated behaviour of the high-energy end of both the synchrotron and SSC components: simultaneous variability of photons and well-defined correlated spectral changes in the medium/hard X-rays and TeV bands. But these models have problems with the bulk-Lorentz factor statistics (Henri & Saugé 2006) and it seems to be very important to measure a detailed variability pattern from X-rays up to TeV γ -rays. Several alternatives have been proposed, and each needs to be quantified in more detail. However, in general one can say that in the leptonic models synchrotron radiation is “primary” and inverse Compton radiation

“secondary”, while for at least one hadronic model it is the opposite: the γ -rays are produced by the “primary” protons through cascades, while the X-rays have a synchrotron origin in the “primary” electrons. In this case the relation between the two components can be looser than for lepton models. Also, in this case the “cascade” spectra are quite soft (lots of soft γ -rays).

To investigate all these theoretical ideas and models, an INTEGRAL ToO proposal was submitted to observe the blazar Mrk 421 when it becomes active. Mrk 421 has a redshift of 0.031, and with a distance of about 125 Mpc [for $H_0 = 71$ km/(s Mpc)] is one of the closest and therefore brightest blazars. It hosts a supermassive black hole with a mass of $(2-8) \cdot 10^8 M_\odot$ in its centre (Barth et al. 2003; Falomo et al. 2002; Treves et al. 2003). At high energies, MRK 421 has been detected in the 10 - 30 MeV range by COMPTEL with 3.2σ (Collmar et al. 1999) and many times above 100 MeV by EGRET (Hartman et al. 1999) and in the TeV range by Cherenkov telescopes (Kerrick et al. 1995; Aharonian et al. 1999; Sambruna et al. 2000; Krennrich et al. 2001; Aharonian et al. 2005 and Rebillot et al. 2006). In June 2006, Mrk 421 became active and our INTEGRAL proposal was activated. The proposal foresaw not only observations with the INTEGRAL instruments but also observations with other telescopes at all wavelengths. Data at radio, optical, X-ray, and TeV wavelengths were taken. However, the observations at TeV energies turned out to be sparse because the visibility period for the Cherenkov telescopes approached its end. It was thus impossible to investigate possible correlations or time lags between the synchrotron and inverse-Compton emission as we wished. We therefore had to concentrate our analysis mainly on the INTEGRAL data itself and on the multi-wavelength spectrum. Preliminary results of this analysis have been already published by Lichti et al. (2007).

4.3.2 Observations

In April 2006 the blazar Mrk 421 increased its intensity to a level >30 mCrab as measured by the all-sky monitor (ASM) of RXTE (the quiescent intensity fluctuates strongly around an average value of 10 - 15 mCrab). It remained at this level until September 2006. This triggered an INTEGRAL observation and correlated multiwavelength observations in the radio, optical, X-ray and TeV ranges. The details of the various observations are given in this section.

4.3.2.1 INTEGRAL observations

On June 14, 2006 (MJD 53900) at 09:53:16.8 hours UT, an observation of this source was triggered with INTEGRAL. The observation lasted about nine days and ended on June 26, 2006 (MJD 53911) at 02:03:55.4 hours UT. In total the source was observed for 829 ks with the instruments IBIS, JEM-X, and OMC in pointing mode (the spectrometer SPI was disabled because of annealing its Ge detectors).

The data of the three operating instruments were analysed with the INTEGRAL Off line Scientific Analysis (OSA) software version 5.1 using the latest response matrices available for that software. The collected data were screened by computing the median count rate for each science window, and it was then compared with each of the other science windows and their distributions. Those science windows showing rates higher than 10 standard deviations from the median count rate were checked again. By this screening effort, three suspicious science windows were detected. A closer look revealed that these science windows belonged to times when INTEGRAL was close to the radiation belts and that the high counting rates were due to the trapped charged particles. After this screening process, 230 science windows remained and were considered for further analysis.

Mrk 421 was clearly detected by all three INTEGRAL instruments. In Figure 1 IBIS/ISGRI, JEM-X, and OMC skymaps in galactic coordinates are shown. In all three maps the source is detected at a high significance level [by IBIS in the energy interval 20 - 40 keV with 160σ , by JEM-X in the energy interval 3 - 4.5 keV with 720σ , and by OMC (limiting magnitude ≈ 18) with $m_v \approx 12.87$]. It should be mentioned that in the field of view of IBIS another AGN, NGC 4151, was observed, which was detected in the energy intervals 20-50 keV, 50-100 keV, and 100-150 keV with 34.7σ , 15.1σ , and 5.4σ , respectively.

The magnitudes m of OMC were converted into differential flux values with the following formula (obtained from A. D. Garau of the OMC team):

$$S(\text{erg/cm}^2 \text{ s } \text{\AA}) = 3.64 \cdot 10^{-9} \cdot 10^{-0.4m}$$

$$\Delta S = 0.921 \cdot S \cdot \Delta m$$

The calibration was obtained from the flux of a star with $m = 0$ at 5500 \AA from Wamsteker 1981. The contribution of the host galaxy was estimated from the colour of a typical elliptical galaxy ($V - R = 0.6$) and its R-band flux of 16.5 mJy to be 9.5 mJy . This host-galaxy flux was taken into account when calculating the energy-density flux. A correction for a possible contribution from the bright ($V = 6$) close-by ($\sim 2 \text{ arcmin}$ away) star 51 Uma (HR 4309) is not necessary because of the sharp pointspread function of the OMC, which drops practically to zero at a distance of 2 arcmin (attenuation factor $< 10^{-23}$).

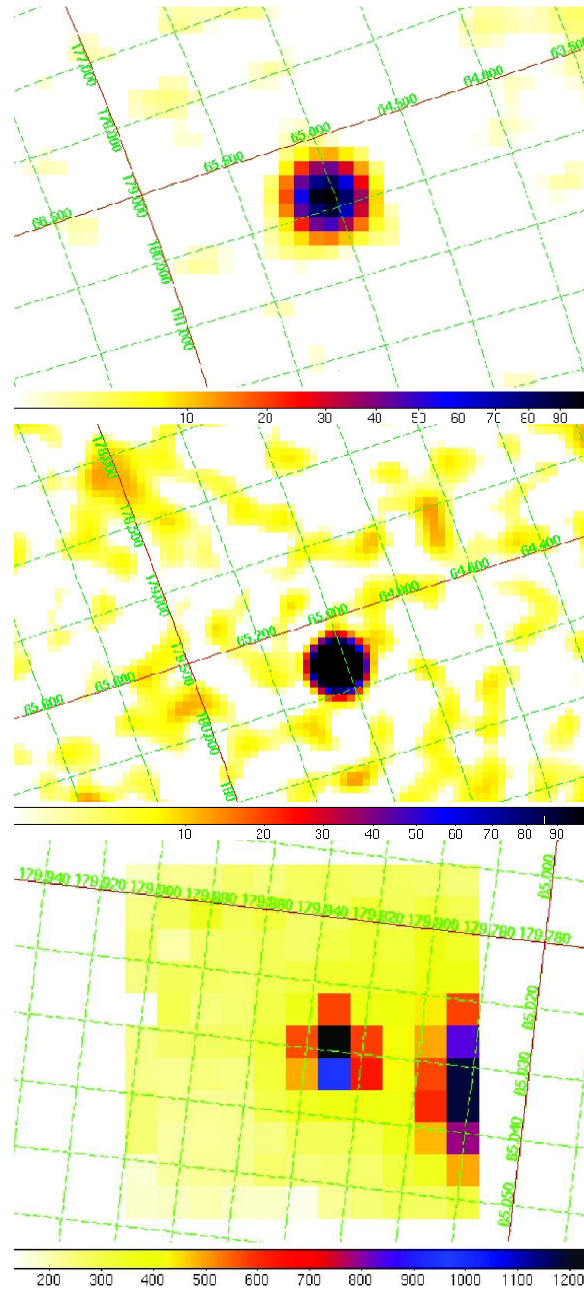


Figure 1. IBIS/ISGRI, JEM-X, and OMC skymaps (from top to bottom) of the region around Mrk 421 for 20 - 40 and 3 - 4.5 keV and at visible wavelengths, respectively, in galactic coordinates. In the OMC map, the

bright star 51 Uma ($V=6$), which is clearly separated from Mrk 421 (distance ~ 2 arcmin), is seen at the edge of the field of view.

Immediately after the beginning of the observation with INTEGRAL, the other observers participating in this multiwavelength campaign were alerted, and they commenced with their observations as allowed by the observational constraints.

4.3.2.2 VLBA observations

Following the notification of the INTEGRAL observations, a request to trigger our previously-approved target of opportunity VLBA observations was sent to NRAO on June 13, 2006. After preparation of the observing schedule, the project entered the queue for dynamical scheduling at the VLBA and actually got scheduled on June 25. The observations started at 17:00 UT on that day and lasted for 14 hours, with scans alternated on six different frequency bands (2.3, 5.0, 8.4, 15.4, 22.2, and 43.2 GHz). The total observing time on each frequency band was roughly 1 hour at 2.3, 5 and 8.4 GHz, 2 hours at 15 GHz, 3 hours at 22 GHz, and 6 hours at 43 GHz. Additional scans on calibrator sources were also inserted into the schedule for proper amplitude and polarization calibration.

After correlation at the Array Operation Center in Socorro, the data were calibrated and corrected for residual delay and delay rate using the NRAO Astronomical Image Processing System (AIPS) and subsequently imaged using the Caltech VLBI imaging software DIFMAP. The flux density was then integrated over each image to produce the total flux densities used in the present study of the spectral energy distribution of Mrk 421. The values of the flux density derived so far in this way are 0.283 Jy at 5 GHz and 0.273 Jy at 8.4 GHz. Presentation of the VLBI images is deferred to a future paper, which will present and discuss the results of the VLBI data analysis in more details.

4.3.2.3 Observation with the Metsähovi radiotelescope

The 37 GHz observations were made with the 13.7 m diameter Metsähovi radio telescope, which is a radome-enclosed paraboloid antenna situated in Finland (24° 23' 38" E, +60° 13' 05" N). The measurements were made with a 1 GHz-band dualbeam receiver centred at 36.8 GHz. The HEMPT (high-electron mobility

pseudomorphic transistor) front end operates at room temperature. The observations are ON-OFF observations, alternating the source and the sky in each feed horn. A typical integration time to obtain one flux-density data point is 1200 - 1400 s. The detection limit of our telescope at 37 GHz is approximately 0.2 Jy under optimal conditions. Data points with a signal-to-noise ratio < 4 were handled as non-detections.

The flux-density scale was set by observations of the bright compact HII region DR 21. Sources 3C 84 and 3C 274 were used as secondary calibrators. A detailed description on the data reduction and analysis is given in Teräsranta et al. (1998). The error estimate in the flux density includes the contribution from the measurement rms and the uncertainty of the absolute calibration.

The observations of Mrk 421 during the INTEGRAL campaign were made in varying weather conditions. The first measurements were non-detections, but shortly the flux level increased and several detections were achieved on days 53902 and 53903. The rest of the campaign was lost due to changeable weather and the end of the telescope time allocation.

The sparse radio data do not allow any conclusion by themselves. For the Metsähovi observations Mrk 421 stays basically on the verge of the detection limit and it never gets very bright. This is typical of the TeV blazars observed at Metsähovi. However, this kind of behaviour is different from other GeV-peaking gamma-ray blazars, and may reflect the different mechanism for the production of gamma rays in Mrk 421 and the other TeV blazars.

4.3.2.4 KVA observations

Mrk 421 was observed in the R-band (centred at 640 nm) with the 35 cm KVA telescope on La Palma, Canary Islands, during 8 nights on June 14 - 22, 2006. The camera employed was an SBIG ST-8 with a gain factor of $2.3 \text{ e}^-/\text{ADU}$ and a readout noise of 14 e^- . Each night 4-10 exposures of 180 s were made. The images were processed in a standard way (bias subtraction, dark subtraction and flat-fielding) and the raw counts of Mrk 421 and stars 1-3 in Villata et al. (1998) were integrated within a 15 arcsec diameter aperture. The magnitude of Mrk 421 was determined by comparing its counts to star 1, for which $R = 14.04$ from Villata et al. (1998) was assumed. The use of differential mode effectively eliminates the influence of varying transparency due to clouds, etc., and accurate fluxes can even be obtained under varying observing conditions. The flux of Mrk 421 was then computed from:

$$F[\text{Jy}] = 3080.0 \cdot 10^{-0.4R}$$

where R is the R-band magnitude (with an effective wavelength of 6400 Å). The normalization constant was taken from Table IV of Bessell (1979). The host galaxy flux with the 15 arcsec diameter aperture is 8.0 ± 0.5 mJy (Nilsson et al. 2007), and this flux was subtracted from the observed fluxes before proceeding with the analysis.

4.3.2.5 RXTE observations

The data of the all-sky monitor (ASM) of RXTE (for a description see Levine et al. 1996) monitors the X-ray sky more or less continuously in the energy range 1.5 - 12 keV. Its data are publicly available. The data for Mrk 421 were downloaded and the fifth lightcurve at the top of Figure 2 was produced. The RXTE counting rates were translated into energy fluxes by using the Crab-nebula flux from Kirsch et al. (2005). These authors derived an energy flux of $2.2 \cdot 10^{-8}$ erg/(cm² s) for the Crab for the energy interval 2-10 keV (i. e. the energy range of the ASM). This corresponds to an RXTE counting rate of 73 counts/s, so 1 RXTE count/s corresponds to $3 \cdot 10^{-10}$ erg/(cm² s). With this value, the RXTE-counting rates were converted to energy fluxes.

4.3.2.6 Swift/XRT observations

The X-Ray Telescope (XRT) instrument on the Swift Observatory (Burrows et al. 2005 and Gehrels et al. 2004) is sensitive to X-rays in the 0.2-10 keV band. These data were reduced using the latest HEASoft tools (version 6.1.0), including Swift software version 2.0 and the latest response (version 8) and ancillary response files (created using xrtmkarf) available in CALDB at the time of analysis. Data were screened with standard parameters, including the elimination of time periods when the CCD temperature was warmer than -48° C. Only WT (windowed timing) mode data was used in this analysis due to the high rates of the active source, and only grades 0 - 2 were included. Since the count rate stayed below ≈ 100 c/s, the WT mode data is free of significant pile-up effects. These data were corrected for effects due to bad columns and bad pixels. Source and background

regions were both chosen in a way that avoids overlap with serendipitous sources in the image. All analysis and fitting of XRT data was done in the 0.3 to 10 keV energy band. Due to the low hydrogen-column density towards Mrk 421 of $1.43 \cdot 10^{20} \text{ cm}^{-2}$, the absorption is $<0.5\%$ and was neglected. Finally the measured counting rates were transformed into energy fluxes using the formula:

$$F[\text{erg}/\text{cm}^2 \text{ s}] = (4 \pm 2.5) \cdot 10^{-11} \cdot \frac{R_{cts}}{s}$$

This conversion factor was calculated using a subset of these Swift-XRT Mrk 421 observations, which included both high and low-state flux measurements. For each time period used, the rate was calculated using the analysis described above, and the spectral fits to these data allowed the flux to be calculated, thus resulting in a conversion factor. Since a single conversion factor was used, rather than many individual time-resolved spectral fits, the large error bars are required to represent the variation in this conversion factor due to spectral variability of the source.

4.3.2.7 Swift-BAT observations

The Burst-Alert Telescope (BAT, Barthelmy et al. 2005) on board the Swift satellite mission (Gehrels et al. 2004) is a coded-mask telescope sensitive to the 15-200 keV energy range. Thanks to the pointing strategy and to its wide field of view (FoV), BAT surveys $\sim 80\%$ of the sky every day. We thus looked in the archive for BAT observations that contained Mrk 421 in the FoV. We selected all observations included in the time-span June 12-26, 2006. The BAT data were processed using the HEASOFT 6.2 package and according to the recipes presented in http://swift.gsfc.nasa.gov/docs/swift/analysis/threads/bat_threads.html. Spectra and lightcurves were corrected for off-axis variation of the rates and residual background contamination as described in Ajello et al. (2008).

4.3.2.8 Whipple observations

The Whipple Telescope is located at the Fred Lawrence Whipple Observatory, at an elevation of 2300 m in Southern Arizona. It comprises a 10 m dish on which 248 mirrors are mounted. These mirrors reflect the Cherenkov light from extensive

air showers onto a 379-element imaging camera at the focal plane of the telescope. The instrument is described in detail by Kildea et al. (2007). The Mrk 421 data presented here were taken in “tracking” mode at large zenith angles on June 18, 19, and 21, 2006 (MJD 53904, 53905, and 53907). The observing scans were performed with the gamma-ray source at the centre of the field of view. No separate control data were taken. Rather, the background rate of gamma-ray-like events was estimated from the distribution of events passing all but the orientation image-selection cuts (Horan et al. 2002). The gamma-ray rates are calculated in units of the flux from large zenith-angle observations of the Crab Nebula, the standard candle in TeV astronomy, and are given in Table 1. They were converted into energy-flux values by integrating the Crab spectrum of Hillas et al. (1998) from the threshold energies of 0.6 and 0.9 TeV to infinity and using the resulting flux values as normalization for the time-averaged spectrum of Mrk 421 as given by Aharonian et al. (1999). Under the assumption that the spectral shape is constant this normalization was adapted to the measured flux values.

MJD ^a	Flux (Crab)	Energy density (erg cm ⁻² s ⁻¹)
53904.17	0.25 ± 0.38	(2.90±4.46) · 10 ⁻¹¹
53905.17	1.63 ± 0.42	(10.89±6.31) · 10 ⁻¹¹
53907.20	0.39 ± 0.28	(3.71±2.82) · 10 ⁻¹¹

Table 1. The measured TeV intensities (in Crab units) of Mrk 421 as measured by the Whipple observatory. ^a the integration time for each data point was 18 minutes. The centre of each time interval is given.

4.3.3 Results of the timing analysis

It is known that blazars are time variable on all different time scales. This is especially true for TeV blazars and thus also for Mrk 421. We have therefore investigated our data in this respect and compare the data collected at different energies with each other and search for possible correlations between them. The results of this exercise are presented in this section.

instrument	average value	error
Radio	0.33 Jy	0.026 Jy
KVA	$1.83 \cdot 10^{-2}$ Jy	$3 \cdot 10^{-4}$ Jy
OMC	$2.579 \cdot 10^{-14}$ erg/cm ² s Å	0.007 erg/cm ² s Å
RXTE	2.86 cts/s	0.3 cts/s

Table 2. Weighted of the fluxes/magnitude/counting rates in Figure 2.

interval number	Start time	End time
1	53902:07:47:23	53904:00:29:59
2	53906:09:53:24	53906:19:07:15
3	53909:09:36:14	53910:18:49:56

Table 3. Time boundaries in modified Julian Date (days:hours:minutes:seconds) for the active state.

4.3.4 The lightcurves

The lightcurves of the various observations are shown in Figures 2 to 7. Whereas the sampling of the lightcurves of the three INTEGRAL instruments and the SWIFT-XRT telescope is ample, this is not the case for the other lightcurves. This makes the search for intensity correlations between the different wavebands difficult if not even impossible. Another fact is striking when one looks at the lightcurves. Although four strong flares are seen in the ISGRI lightcurve (and even more in the Swift- XRT lightcurve of Figure 3), these flares are not visible at the other energies. An inspection of the X-ray lightcurves reveals the following:

- the strength and the shapes of the flares vary significantly;
- the shape of the flares is not symmetric (some flares show a sharp rise and a slow decay time, others a slow rise and a fast decay time);
- the duration of the flares is about 0.5 days;
- comparing Figures 3 and 4 one can see that the energy spectrum of the flare around day 53910.5 is qualitatively softer than the spectrum of the other flares;

- from a linear fit to all the data, it becomes obvious that the total intensity is slightly increasing with time.

Especially interesting is that these flares are also not seen by the OMC. It is the common understanding that in blazars, if viewed under small angles, the optical thermal emission of the accretion disk and of the galaxy is outshined by the non-thermal beamed emission of the jet (Tavecchio 2005). Since both the X-rays and the optical photons are produced by the same population of relativistic electrons via synchrotron emission, one would expect similar (if not even identical) lightcurves, if this scenario is correct. For Mrk 421, this happened to be the case in 2001 when a flare showing variability in the visible band coincident with that at radio wavelengths and at TeV energies was observed (Katarzynski et al. 2003). That this is not observed in our data contradicts to this hypothesis and asks for an explanation. Possible explanations will be discussed in the last section.

From the radio, KVA, OMC, and RXTE lightcurves of Figure 2, the average fluxes/magnitude/counting rates were calculated. The weighted means are given in Table 2. The ISGRI lightcurve of Figure 5 was used to define by eye the times when the source was in quiescent and active states. Three time intervals were specified and their boundaries are given in Table 3.

4.3.5 Rise-time analysis

The rise-time scale gives information about the extension of the emission region. From observations at TeV energies it is known that Mrk 421 shows short-time variability with time scales of about one day and shorter (Aharonian et al. 2002, 2003). Doubling times with time scales of about one day or even down to 15-20 minutes were also reported by Cortina and Schweizer (2002) and Krennrich et al. (2003). In May 1996 two fast flares were observed (Gaidos et al. 1996). The first one had an intensity 10 times higher than the one of the Crab nebula (the highest flux ever observed from this source at these energies) with a time scale of <1 day. The second one a week later had an unprecedented time scale of ~30 minutes indicating a very small emission region!

An inspection of the ISGRI lightcurves reveals that the steepest ascent occurred in the third time interval. Fitting an exponential rise-time law of the form $a \cdot e^{t/t_0}$ to the data of the energy interval 40 - 100 keV one finds a value of 2.79 hours for t_0 . In the energy interval 20 - 40 keV, the increase is somewhat slower (only 4.28 hours).

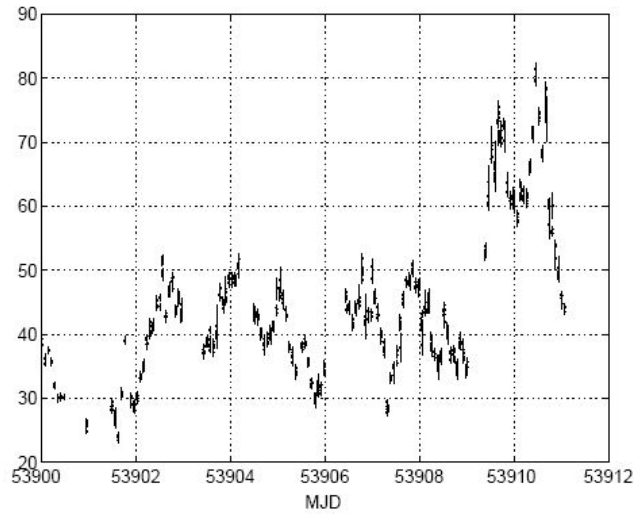


Figure 3. Swift-XRT lightcurve in the energy interval 0.3 - 10 keV. The dotted lines give only the coordinates, not the intervals of the active phases in Figures 4 to 6.

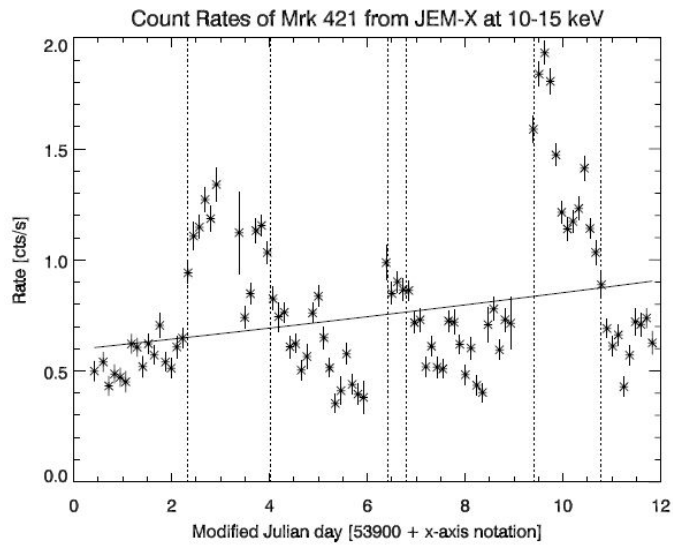


Figure 4. JEM-X lightcurves in the energy interval 10 - 15 keV. The time intervals for the active phases are indicated by dotted lines. A parabola was fitted to all counting rates to guide the eyes.

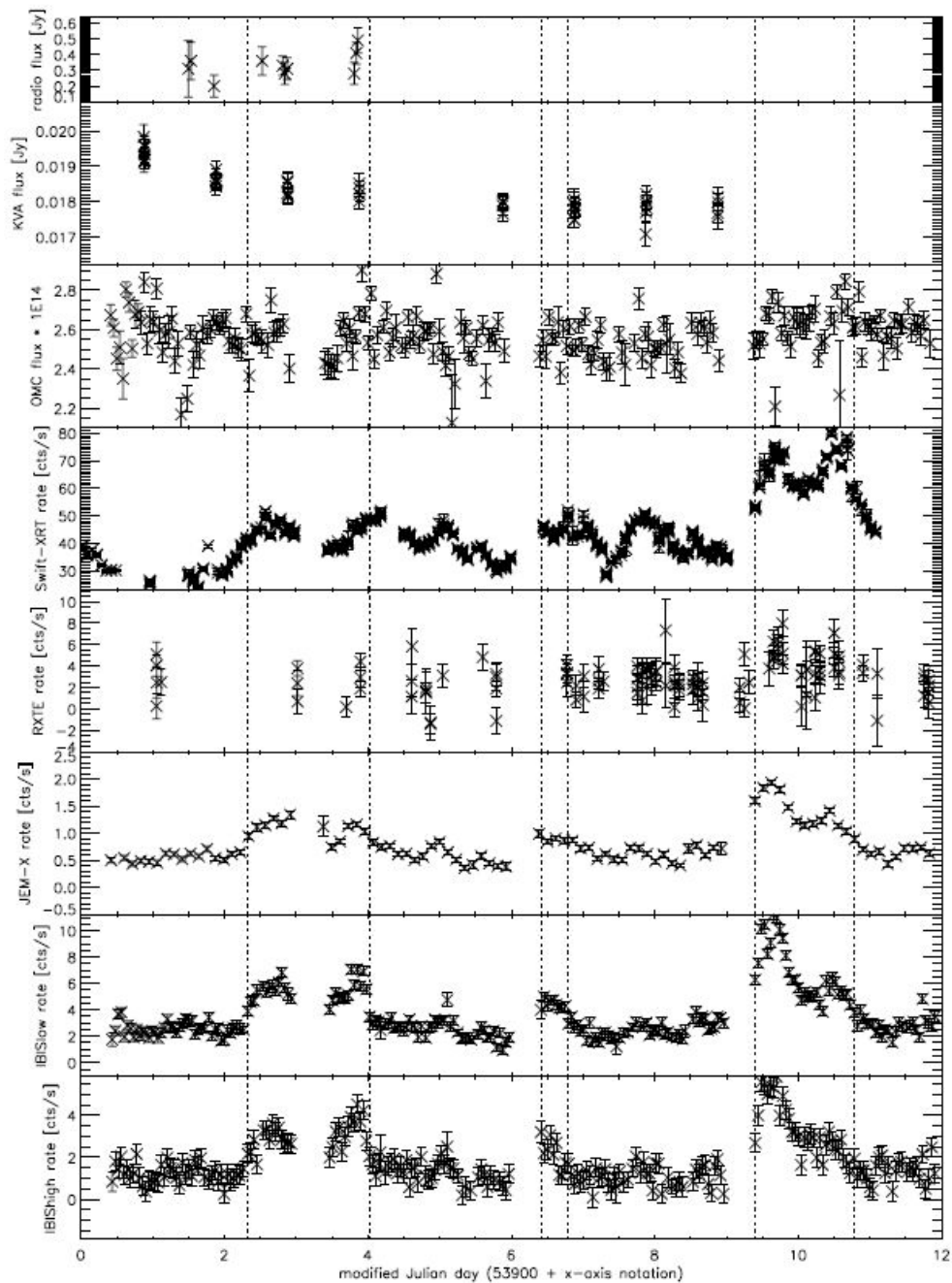


Figure 2. All lightcurves for Mrk 421 at radio, optical, X-ray and gamma-ray wavelengths. The data of the OMC (given in $\text{erg cm}^{-2} \text{s}^{-1} \text{\AA}^{-1}$) and KVA

telescopes were not extinction-corrected, since the extinction E_{B-V} in the direction of Mrk 421 is only 0.03. The time intervals for the active phases are indicated by the dotted lines.

One can now calculate the size of the emission region with the formula:

$$l \leq \frac{c \cdot t_0 \cdot \delta}{1 + z}$$

with c the speed of light, δ the Doppler factor ($= 12$; from Kino et al. 2002) and z the redshift. Inserting the value from above one means that the emission region must be < 234 AU (the Schwarzschild radius of Mrk 421 is between 4 and 16 AU and the radius of the last stable orbit between 12 and 47 AU). From the shortest time scale measured at TeV energies an extension was derived of the emission region of ≤ 2.5 AU (Aharonian et al. 2002). From pure high-resolution radio-interferometric observations Charlot et al. (2006) derived an upper limit on the high-energy emission region of 0.1 pc (≈ 20000 AU). Thus a dependence of the size of the emission region on energy seems to exist: the higher the energy, the smaller the emission region!

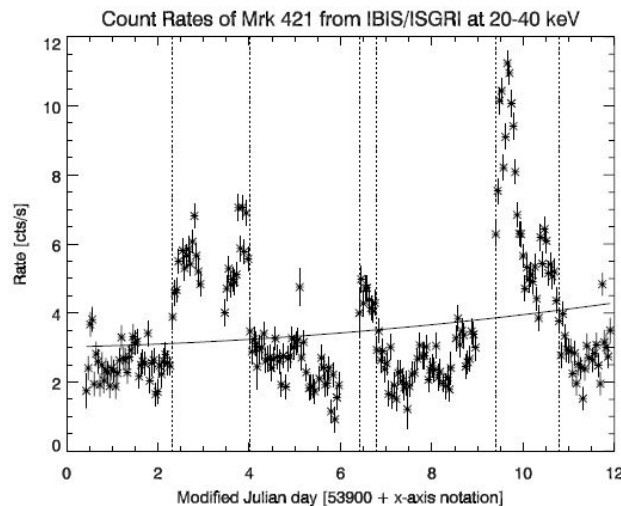


Figure 5. IBIS/ISGRI lightcurve in the energy interval 20 - 40 keV. The time intervals for the active phases are indicated by the dotted lines.

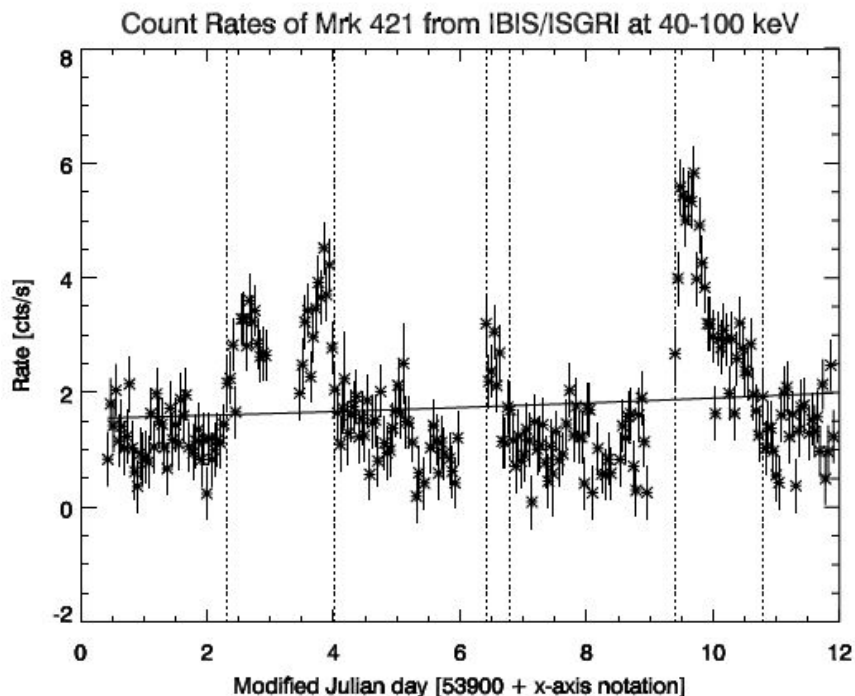


Figure 6. IBIS/ISGRI lightcurve in the energy interval 40 - 100 keV. The time intervals for the active phase are indicated by the dotted lines.

4.3.6 Variability analysis

The fractional variability V (see appendix in Fossati et al. 2000 for the definition) was calculated for all lightcurves. The result is shown in Table 4. The same behaviour as already found by previous authors (e. g. Fossati et al. 2000, Sembay et al. 2002) is confirmed by our observations: the fractional variability increases with energy. This behaviour seems to be common in blazars (Ulrich et al. 1997). If we fit a power law to the data we get $V \propto E^{0.28}$. This is in good agreement with the laws found by Fossati et al. (2000) ($V \propto E^{0.25}$) and by Giebels et al. (2007) ($V \propto E^{0.24}$). This reflects that the higher energies are emitted from regions closer to the central black hole, which are smaller in extension than regions farther away. Since the emission from small regions can vary faster than the ones from larger regions the observed trend can be understood qualitatively.

intstrument	low-energy bound [eV]	high-energy bound [eV]	V
Metsähovi	-	-	Undefined
KVA	1.85	2.04	0.0314
OMC	2.14	2.39	0.0393
Swift-XRT	300	10000	0.266
RXTE	2000	10000	0.4258
JEM-X	10000	15000	0.4266
IBIS/ISGRI	20000	40000	0.5146
IBIS/ISGRI	40000	100000	0.5723

Table 4. The fractional variability measure V for the different lightcurves.

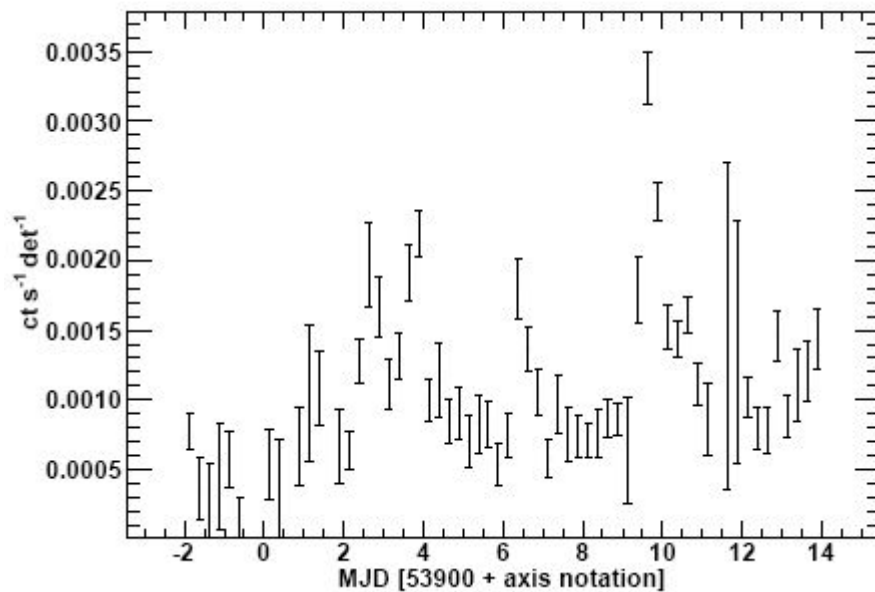


Figure 7. Swift-BAT lightcurve in the energy range 15 - 200 keV is shown.

4.3.7 Time-lag analysis

The time lag between the two ISGR1 lightcurves of the energy intervals 20-40 keV and 40-100 keV was calculated with the Z-transformed discrete-correlation function (ZDCF; Edelson & Krolik 1988, Tal 2007). The value of the ZDCF as a function of the time lag τ is shown in Figure 8. Five maxima with ZDF values around 0.5 are seen, two at $\tau \approx \pm 3.4$ days, two at $\tau \approx \pm 7$ days, and one at $\tau \approx 0$ day. The shifts at ± 3.4 days and ± 7 days correspond to the time difference between the flares seen in Figures 5 and 6 and thus do not reveal new information. Important, however, is the question whether the central peak has its maximum really at $\tau \approx 0$ days. To find this out, a Gaussian and a linear background were fitted to the data from $\tau = -1$ day to $\tau = +1$ day. The data can be described well with a Gaussian ($\chi^2_{\text{red}} = 0.114$). The fit to the data reveals that, with a significance of 1.8σ , the maximum is not at a time lag of zero, but at $\tau = (-40.8 \pm 23.3)$ minutes. The negative sign indicates that the variations at lower energies lag behind those at the high energies.

The same time-lag analysis was performed for the IBIS (20 - 40 keV) / JEM-X (10-15 keV) and the JEM-X (10-15 keV) / Swift-XRT (0.3-10 keV) lightcurves. In the first case the time lag is consistent with a lag of zero minutes (actually -4.25 ± 30.4 minutes), and in the second case the time lag is positive and has a value of (102.6 ± 59) minutes. Similar time lags (35 - 47 minutes) were found by Fossati et al. (2000) for the energy ranges 0.1 - 1.5 keV and 3.5 - 10 keV using BeppoSAX data and by Takahashi et al. (1996) as a function of energy for the energy range 0.5 - 7.5 keV using ASCA data. Especially Takahashi et al. (1996) found that the time lags decrease with increasing energy, consistent with our results. But their time lags were all negative, while we also find positive timelags. Positive time lags were also measured by Ravasio et al. (2004) and by Brinkmann et al. (2005) in the energy range 0.6-10 keV using XMM data. But the statistical significance of our time lags is marginal, so one can question their reality. The importance of this question and the ample number of lightcurves at different energies measured during our multiwavelength campaign would deserve a more detailed analysis, which is, however, not the scope of this paper.

The time lags must be produced by energy-dependent mechanisms, for instance, particle cooling, and acceleration. The higher-energy particles cool faster and accelerate slower than the lower-energy particles, therefore the negative timelag can be used to estimate the magnetic-field strength from the measured negative time lag. The theory of this process was developed by Kazanas

et al. 1998. Based on the results of this theory Chiapetti et al. (1999) derived the equation (6) which provides an estimate of the magnetic field B:

$$B = 300 \cdot \left(\frac{1+z}{\nu_1 \cdot \delta} \right)^{\frac{1}{3}} \cdot \left(\frac{1 - \sqrt{\frac{\nu_1}{\nu_0}}}{\tau} \right)^{\frac{2}{3}} \approx \left(\frac{300^3}{\nu_1 \cdot \delta} \right)^{\frac{1}{3}} \cdot \tau^{-\frac{2}{3}}$$

where δ is the Doppler factor, z the redshift, and ν_0 and ν_1 are the frequencies of the corresponding energy intervals (in units of 10^{17} Hz) at which the time lag τ (τ in s) has been measured.

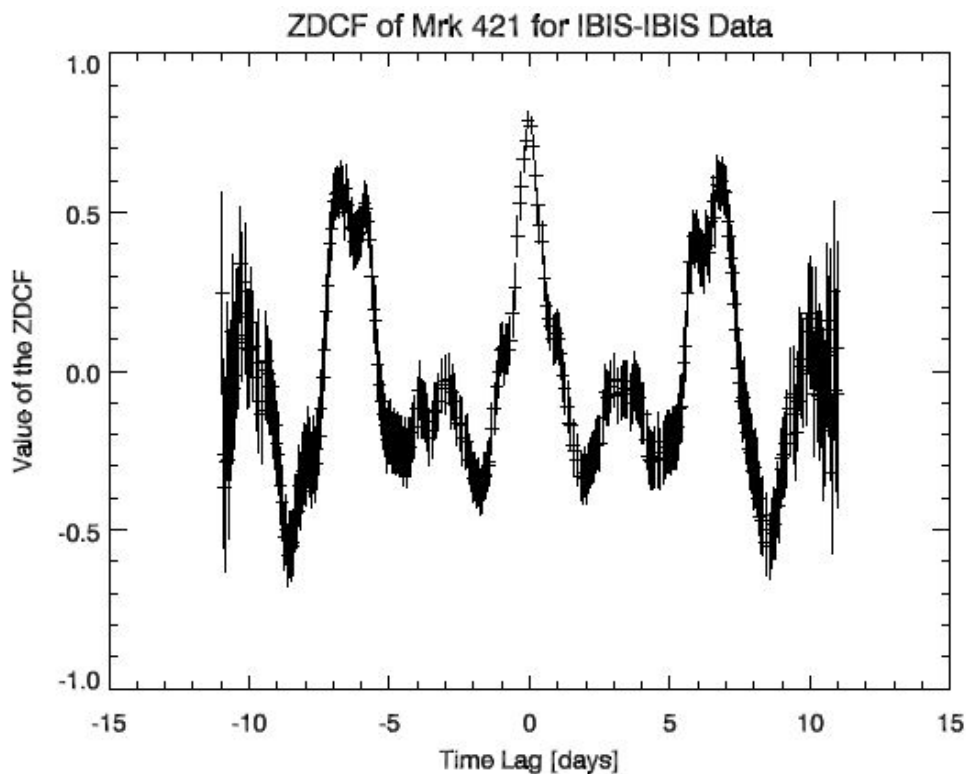


Figure 8. The Z-discrete correlation function of the IBIS data is shown.

For determining the frequencies ν_0 and ν_1 the mean energy for the energy intervals given above were calculated using the power laws derived from the fit to the data (see Tables 5 and 6). Inserting those, together with the other parameters from above, one gets a magnetic-field strength of (0.08 ± 0.03) G. Similar values (0.12 G) were found by Kino et al. (2002) using the observables of Mrk 421 from Kataoka (2000), by Konopelko et al. (2003) (0.1 G) and by Giebels et al. (2007) (~ 0.1 G).

But the value of the Doppler factor is highly uncertain. Rebillot et al. (2006) investigated two models with $\delta = 50$ and 1000 (in their model a higher Doppler factor corresponds to a smaller emission region). If we adopt these values, we find values of (0.06 ± 0.02) G and (0.02 ± 0.007) G, respectively, for the magnetic-field strength B. Values of the Doppler factor between 50 and 100 seem to be suggested by the data (see Krawczynski et al. 2001 and Mastichiadis and Kirk 1997). However, such large Doppler factors are not observed with VLBI observations (e.g. Piner and Edwards 2005), so this might indicate a velocity structure in the jet (Georganopoulos and Kazanas 2003; Ghisellini et al. 2005).

4.3.8 Correlation analysis

We investigated whether the X-ray data of ISGRI correlate with the optical data of OMC. For this, investigation time intervals were specified during which the background-subtracted ISGRI count rates of Mrk 421 were lying in well-defined, but arbitrarily-chosen count-rate intervals. The average ISGRI count rates and the average optical fluxes of OMC were calculated for these time intervals. The result of this correlation analysis is shown in Figure 9. Although the scatter of the results is quite large, a slight increase in the optical flux with increasing ISGRI count rate is detected. If one fits a straight line to the data, this dependence becomes more evident. The functional dependence of the OMC flux on the ISGRI rate is:

$$F_{\text{OMC}} = 2.5 \cdot 10^{-14} + 1.96 \cdot 10^{-16} \cdot R_{\text{IBIS}}$$

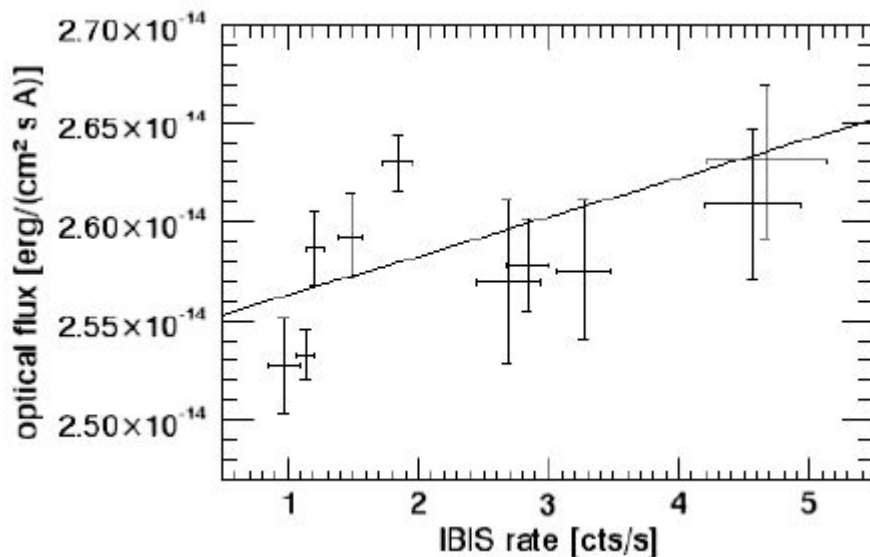


Figure 9. Intensity correlation between OMC and IBIS data. The count-rate range of the ISGRI count rates was split into arbitrary-chosen intervals given by the error bars.

4.4 Results of spectral analysis

The results of a spectral analysis of the data of Mrk 421 at X-rays are presented in this section. First, we investigated how the energy spectrum evolves when going from the quiescent into the active state. Secondly, we calculated hardness ratios and looked for possible correlations. And third, we combined all data across the frequency range and constructed an energy-density spectrum νF_ν .

4.4.1 Spectral fits

The data from JEM-X and IBIS were collected for the quiescent and active states according to the times given in Table 3. Then different spectral models

were fitted to the quiescent and active fluxes using the functions available in XSPEC11. Since ISGRI and JEM-X were excellently cross-calibrated by the two responsible teams, no cross-calibration factor had to be applied. The results of this fitting exercise are given in Tables 5 and 6. In addition, a spectrum with a log-parabolic function was fitted to the data (see Massaro et al. 2004). The results of these fits are shown in Table 7.

It turned out that a broken power law of the form:

$$F(E) = A \cdot \left(\frac{E}{1 \text{ keV}}\right)^{-\alpha} \quad \text{for } E \leq E_b$$

$$F(E) = A \cdot E_b^{\beta-\alpha} \cdot \left(\frac{E}{1 \text{ keV}}\right)^{-\beta} \quad \text{for } E > E_b$$

(with A the normalization constant and with α and β the low- and high-energy spectral indices, respectively) gave the best fit result in both cases. (The joint power law gave an equally good fit, but it leads to an unrealistic high value of 6.5 for the high-energy power-law index β and was therefore discarded.)

state of source	χ^2_{red}	norm.constant [keV ⁻¹ cm ⁻² s ⁻¹]	α
quiescent	0.681	0.53±0.2	2.46±0.11
active	1.42	1.3±0.4	2.49±0.14

Table 8. Results of fits to the Swift-BAT data with a simple power law for both states for a reference energy of 1 keV.

The results of the fits for the quiescent and active states are shown in Figures 10 and 11, respectively. With a reduced χ^2 value of ~ 1.9 , the fits are not excellent, but reasonable. The reason for the imperfect fit is that the fluxes of JEM-X and ISGRI in the overlapping energy intervals differ as is seen from the residuals. The results of the spectral analysis can be summarised as follows:

- a broken power law fits the data best in both cases (quiescent and active)

- the break energy E_b has a value of ~ 43 keV
- the index a is larger than 2
- the spectral parameters do not change significantly with the state (although a slight spectral hardening of the low-energy index a is observed)

The third point indicates that we have only measured the declining part of the X-ray spectrum and can therefore not determine the maximum or minimum of the energy-density spectrum νF_ν . We can only say that the maximum is below the low-energy limit of JEM-X of 3 keV. It should be noted here that peak values up to 5.5 keV were measured with BeppoSAX (Massaro et al. 2004). The spectrum also falls off continuously to the upper energy limit of 200 keV, so a possible minimum of the νF_ν spectrum must lie at an energy greater than 200 keV.

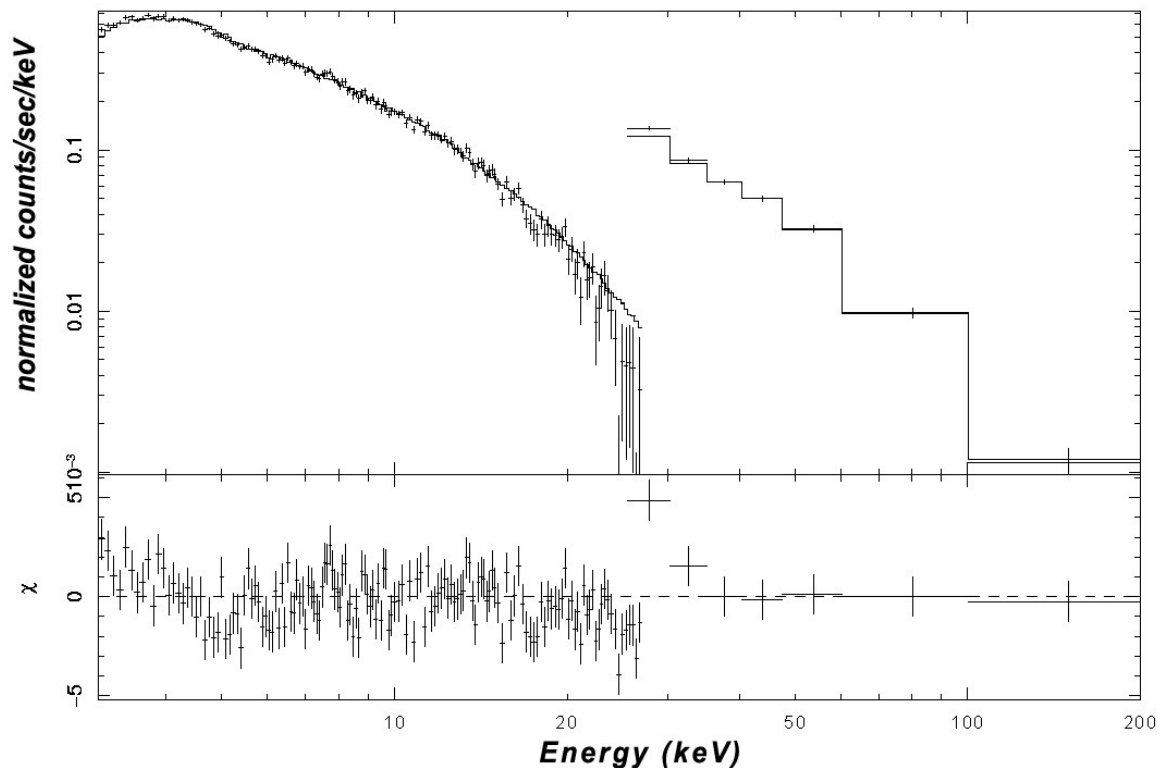


Figure 10. Result of the fit of a broken power law to the JEM-X and ISGRI data in the quiescent state. The top panel shows the spectral data with the fit function, the bottom panel the residuals of the fit.

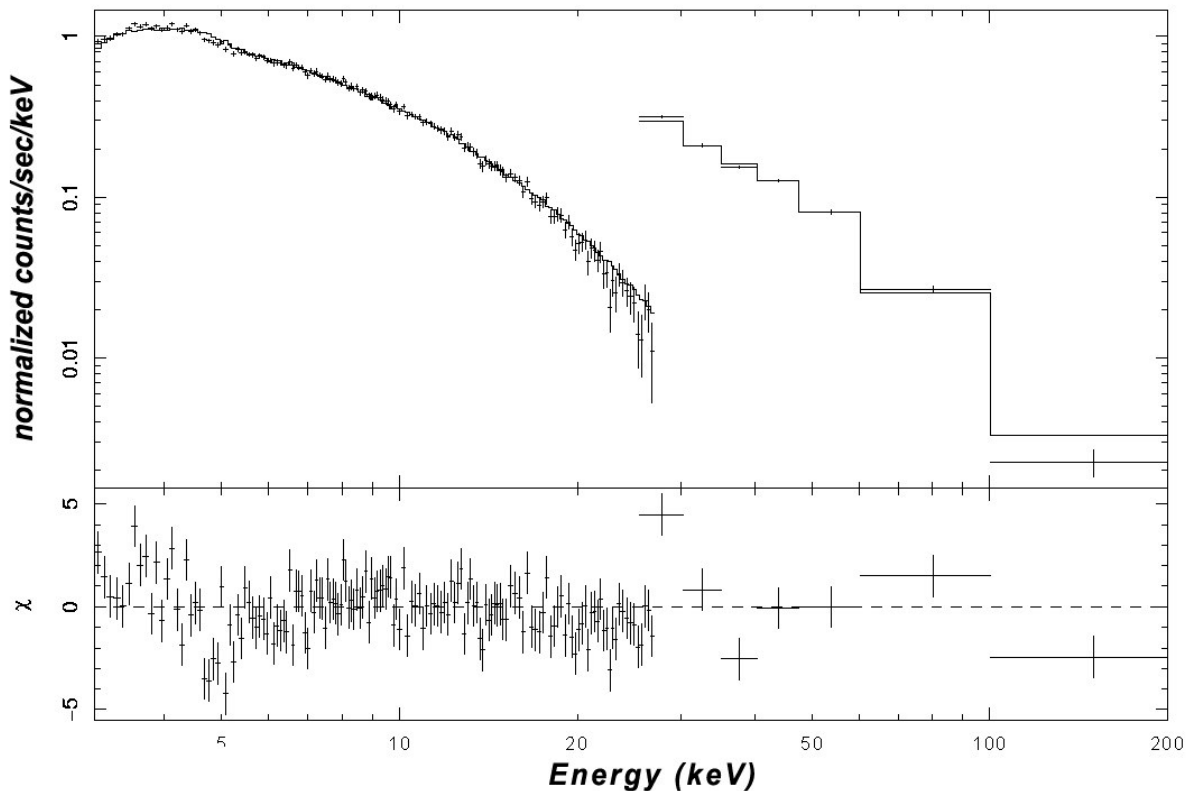


Figure 11. Result of the fit of a broken power law to the JEM-X and ISGRI data in the active state. The top panel shows the spectral data with the fit function, the bottom panel shows the residuals of the fit.

The data from Swift-BAT were also spectrally analysed for the quiescent and the active state. They could be best fit with a simple power law. The results are summarised in Table 8. Within the errors, the spectral indices are identical for the quiescent and active states. This is consistent with the results of the data of Tables 5 and 6 for the joint power law where the spectral index also does not change with intensity. However, the spectral index obtained from the Swift-BAT data is with ~ 2.5 somewhat larger than the one obtained from the JEM-X and IBIS/ISGRI data (~ 2.3) but consistent with our result within 3σ .

The intensity of the Swift-BAT data between the quiescent and active states changes by a factor of 2.45 ± 1.2 . This is a bit higher than the values derived from the results of Tables 5 and 6 but still compatible within the error.

4.4.2 X-ray luminosity

By integrating the broken power-law spectrum over the energies 3-200 keV and multiplying with the surface of a sphere one obtains the isotropic X-ray luminosity in this energy range. Using the parameters of Tables 5 and 6 one finds luminosities of $1.75 \cdot 10^{45}$ erg/s and $3.73 \cdot 10^{45}$ erg/s for the quiet and active states, respectively. This is much lower than the Eddington limit, which is in the range of $(2.4 - 9.6) \cdot 10^{46}$ erg/s. But it should be noted that the emission is actually beamed and that the luminosity is thus lower than given above.

4.4.3 Hardness ratios

We calculated the hardness ratio (HR) of the two IBIS/ISGRI energy bands 20 - 40 keV (L-band) and 40 - 100 keV (H-band) $HR = \text{H-band rate} / \text{L-band rate}$. It is plotted in Figure 12 as a function of the time and in Figures 13 and 14 as functions of the Lband and the H-band intensities. The hardness ratio in Figure 12 is fairly constant in time and does not follow the lightcurves of Figures 5 and 6, so we do not observe an evolution in the hardness ratio with intensity. When inspecting Figures 13 - 14, one notes a remarkable difference: whereas no correlation is obvious when one plots the ratios as a function of the L-band count rate (Figure 13), a correlation for intensities up to ~ 2 counts/s seems to be present when the plot is done as a function of the H-band count rate (Figure 14). But this might be because there are no events with < 1 counts/s in Figure 13.

In Figure 15 the hardness ratio is shown for two energy bands [(1-10 keV)/(0.3-1 keV)] of the Swift-XRT. A comparison with the lightcurve of Figure 3 shows that the hardness ratio follows the lightcurve closely. This means that we have observed an intensity-hardness-ratio correlation; i. e., the brighter the source the harder the spectrum. But this is obviously not valid at all times. The last peak in Figure 3 (at MJD ≈ 53910.5) is only marginally visible in Figure 15. One would expect a hardness ratio of ~ 2 (similar to the hardness ratio observed at MJD ≈ 53909.5), but actually it is only about 1.5. This means that the emission process

must have changed significantly on a time scale of <1 day. We obviously observed a clear hard-to-soft evolution.

The overall hardness-ratio correlation is also visible when one plots the Swift-XRT hardness ratio as a function of the Swift-XRT count rate as in Figure 16. Although the positive correlation with the rate is not striking it is clearly recognisable. The large scatter around this correlation is probably due to a shorttime scale and overlapping variability.

Model ^a	χ^2_{red}	norm.constant [keV ⁻¹ cm ⁻² s ⁻¹]	α ^b	B ^c	E _b [keV] ^d
PL	2.17	(0.378±0.004)	2.318±0.006	-	-
Joint PL	1.85	(9.3±3)·10 ⁻⁶	2.298±0.007	6.5±1.0	149±11
BrokenPL	1.83	(0.365±0.005)	2.300±0.006	3.0±0.2	45±4
Band	2.2	(2.8±5)·10 ⁻⁵	2.0±0.2	2.32±0.01	13±2
PL exp cut-off	2.17	(0.355±0.006)	2.27±0.01	-	311±77

Table 5. Model fits to the JEM-X and ISGRI data of the quiescent state. The reference energy is at 1 keV.

Model ^a	χ^2_{red}	norm.constant [keV ⁻¹ cm ⁻² s ⁻¹]	α ^b	B ^c	E _b [keV] ^d
PL	3.67	(0.530±0.005)	2.164±0.004	-	-
Joint PL	1.85	(9.9±3)·10 ⁻⁶	2.298±0.007	6.65±1.1	145±10
BrokenPL	1.89	(0.490±0.005)	2.12±0.05	2.90±0.08	41±2
Band	3.85	(9±7)·10 ⁻⁵	1.8±0.09	2.20±0.02	23±3
PL exp cut-off	2.36	(0.530±0.005)	2.04±0.01	-	132.0±0.3

Table 6. Model fits to the JEM-X and ISGRI data of the active state. The reference energy is at 1 keV. The parameters and functions are explained here below.

^a the definitions of the mathematical forms of the used functions are contained in the XSPEC11 manual [with the exception of the joint PL which has the form

$$\left(\frac{E}{E_b}\right)^{-\alpha} / \left[1 + \left(\frac{E}{E_b}\right)^{\beta-\alpha}\right]$$

^b α is the spectral index at energies below E_b

^c β is the spectral index at energies above E_b

^d E_b is the break energy

state of source	χ^2_{red}	norm.constant [keV ⁻¹ cm ⁻² s ⁻¹]	a	b
quiescent	2.23	$(7.21.9 \pm 0.2) \cdot 10^{-5}$	2.35 ± 0.02	$(1.1 \pm 0.6) \cdot 10^{-2}$
active	2.91	$(1.77 \pm 0.03) \cdot 10^{-4}$	2.28 ± 0.01	$(5.0 \pm 0.5) \cdot 10^{-2}$

Table 7. Results of fits to the JEM-X and ISGRI data with a log - parabolic function [= $K \cdot (E/E_1)^{-a-b \cdot \log(E/E_1)}$] for both states for a reference energy of $E_1 = 40$ keV.

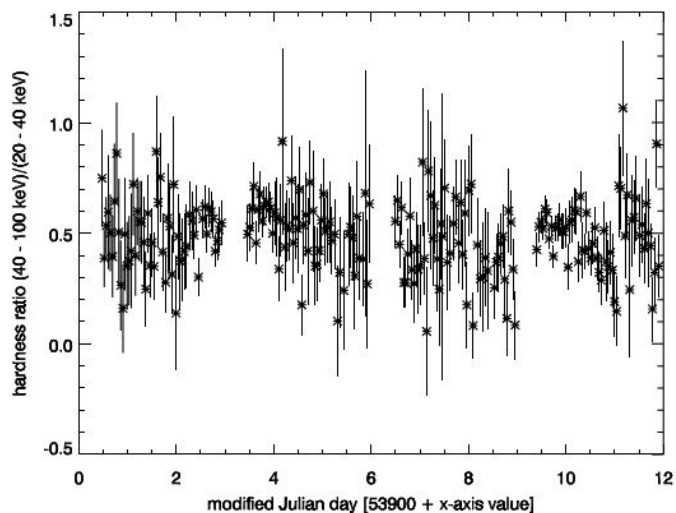
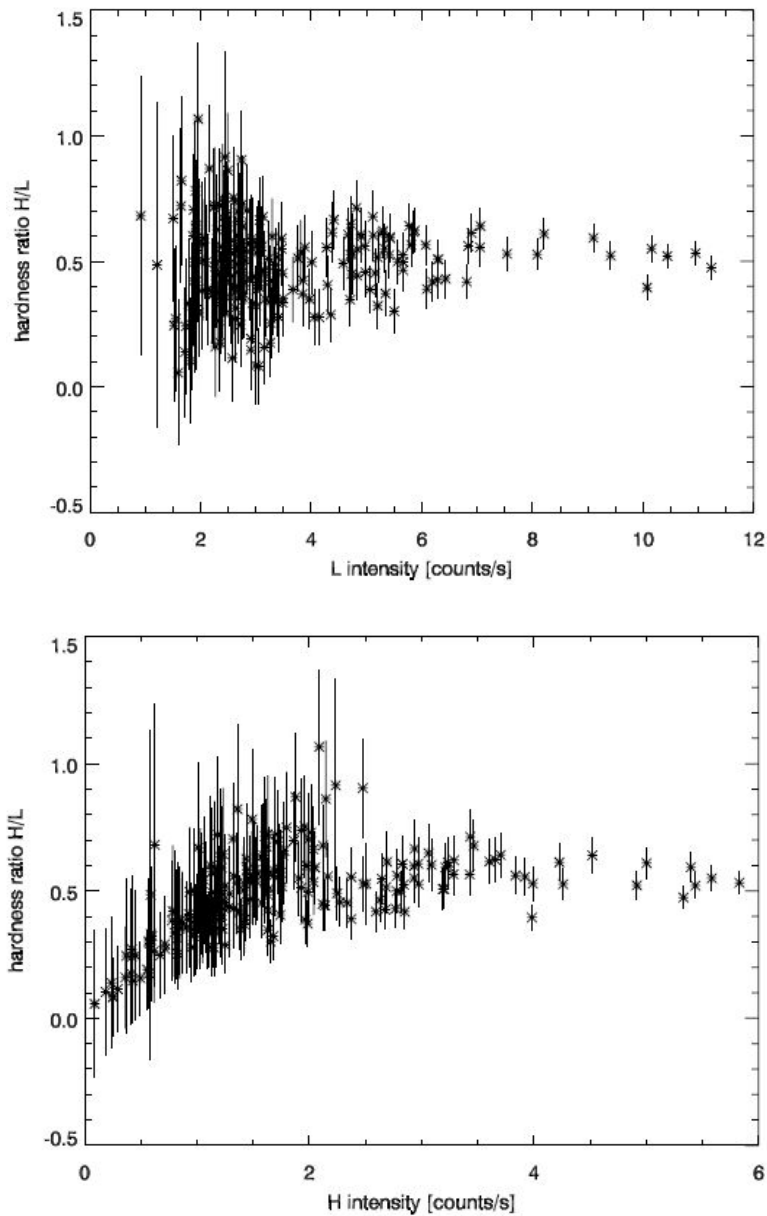
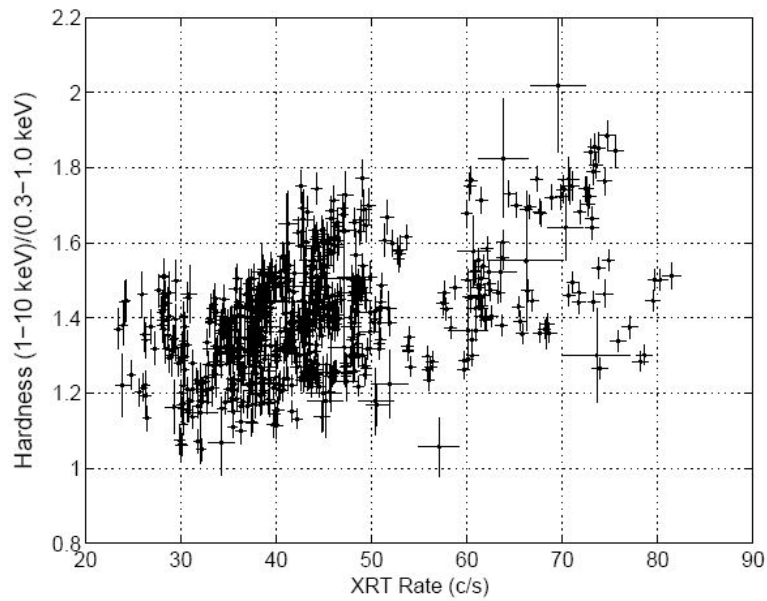
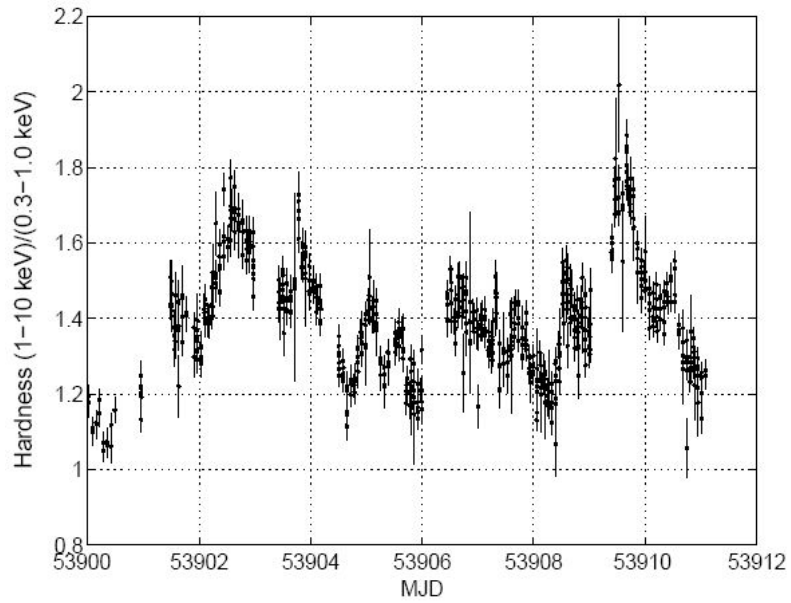


Figure 12. Hardness ratio H/L as function of time for the IBIS/ISGRI data.



Figures 13 and 14. The upper panel (fig. 13) shows the hardness ratio H/L as a function of the L-band (20 - 40 keV) intensity of the IBIS/ISGRI data. The lower panel (fig. 14) represents the hardness ratio H/L as function of the H-band (40 - 100 keV) intensity for the same instruments data.



Figures 15 and 16. Hardness ratios of Swift-XRT data as function of time (upper panel fig. 15) and as function of XRT intensity (lower panel fig. 16).

4.4.4 Multiwavelength spectrum νF_ν

The data from all observations (with the exception of the JEM-X and ISGRI data) were averaged over the observation time span, corrected for extinction at optical wavelengths using the extinction value $E_{B-V} = 0.03$ of Burstein and Heiles (1982) and the formalism of Seaton (1979), converted to the same unit [$\text{erg}/(\text{cm}^2 \text{ s})$], and then plotted in an energy-density spectrum (νF_ν spectrum). This multiwavelength spectrum is shown in Figure 17. Unfortunately the number of data points is sparse, especially at energies above ~ 500 keV where only two data points (measured at different times) at TeV energies exist. It should also be noted that the data used to create the average high state and low state SED data points shown in Figure 17 were extracted from the same time windows for all instruments; however, the data are not strictly simultaneous. Due to this non-simultaneous data, it is possible that small time-scale flaring could cause a systematic offset of the SED from one energy band to another. This could explain the discrepancy between the Swift-XRT data and the JEM-X and IBIS data.

The data are compared with the theoretical models of Maraschi et al. (1999), Kino et al. (2002) and Blazejowski et al. (2005). The models of Maraschi et al. (1999) and Blazejowski et al. (2005) were adjusted to the flux measured by IBIS in the quiescent state by applying a factor of 3.2. Both models predict the actual flux measured by Whipple at TeV energies quite well, but seem to fail to fit the optical data and the radio flux. On the other hand, the model of Kino et al. (2002) fits the radio data quite well, but has problems fitting the X-ray and TeV data, together with the radio data. It is remarkable that the JEM-X spectrum is flatter than predicted by the models, even though their shape differs significantly. The three models also do not predict the break at an energy of 43 keV.

The best agreement between data and models is found for the model of Blazejowski et al. (2005). However, it should be noted here that the models were fitted to data measured at different times, so it is not surprising that they do not fit our data well. In contrast, they show that not only the intensity, but also the spectral shape of Mrk 421 is extremely variable.

4.4.5 Model fits

We also tried to fit a theoretical emission model to the data of the energy-density spectrum of Figure 17. The model curves fitting the data shown in Figure 18 best were obtained using a one-zone synchrotron self-Compton model (SSC)

including the full Klein-Nishina cross section for inverse Compton scattering (Jones et al. 1968, Blumenthal et al. 1970). The model assumes a spherical blob with constant injection of non-thermal electrons and a constant escape rate for electrons and photons. The model details are described in R uger et al. (2008).

In this calculation the electron distribution is assumed to be constant (stationary) and is represented by a smoothed broken power law combined with an exponential cut-off as given in Tavecchio et al. (2001):

$$n_{el}(\gamma) = K \cdot \gamma^{S_1} \cdot \left(1 + \frac{\gamma}{\gamma_{Br}}\right)^{S_1 - S_2} \cdot e^{\left(-\frac{\gamma}{\gamma_{Max}}\right)}$$

with the differential electron number density N , Lorentz factor γ , break energy $E_b = \gamma_b mc^2$, spectral indices S_1 and S_2 , normalization factor K , and cut-off energy γ_{max} . This phenomenological Ansatz for the spectrum is justified by self-consistent simulations (see R uger et al. 2008).

With this electron distribution, the radiative transfer equation was solved numerically in the comoving frame and the observed spectrum obtained by applying the beaming effect using the Doppler-factor δ . Specifically, the transformation for the intensity is:

$$I_{\nu, beamed} = \delta^3 \cdot I_{\nu, comoving \ frame}$$

In addition, one can show that, for dominating synchrotron losses, the second spectral index can be rewritten as $S_2 = S_1 + 1$, so one less parameter has to be determined. A first estimation of the parameter set is obtained by using the equations given in Kataoka et al. (2000). Small variations lead to the best-fit parameter set presented in Table 9.

From this table one can see that both parameter sets differ only in the break energy γ_b and the cut-off energy γ_{max} . The latter energy represents the efficiency of the acceleration mechanism.

Since γ_b results from the emerging balance between cooling and acceleration of the electrons, a more efficient acceleration mechanism leads to both a higher γ_{max} and a higher γ_b . Therefore we conclude that the variability of the emission can be due to varying efficiency of the acceleration.

It should be noted, however, that a change in the spectrum of the injected electrons without changing the environmental parameters like the magnetic fields and/or the Doppler factor is difficult to understand. But the acceleration of particles can be influenced without changing the environmental parameters by taking turbulence into account which can have a dramatic influence on the particle acceleration; on the one hand, enhanced turbulence can change the spectral indices (Vainio & Schlickeiser 1998 and Vainio & Spanier 2005), and on the other, the decay length of turbulence can change the maximum energy (Vainio & Schlickeiser 1998 and Vainio & Spanier 2005). However these effects are not covered in our model, just like the geometry of the shock and the shock thickness.

The fit presented here is not unique (see discussion in Tavecchio et al. 1998) and the observed change in spectral energy distribution can also be modelled by slightly varying the magnetic field strength and Doppler factor. The changes in these parameters would lead to change in electron spectrum, and such detailed modelling is beyond the scope of this paper. The Doppler factor and magnetic-field strength modeled here are similar to those derived for other TeV-emitting blazars. However, very long baseline interferometric observations show that such high Doppler factors would require very extreme assumptions for the viewing angle (0.015 degrees) and the Lorentz factor (25) (Piner and Edwards 2005). Therefore adopting models where the jet has a velocity structure (Georganopoulos and Kazanas 2003, Ghisellini et al. 2005) might be more feasible, but such modelling is beyond the scope of the paper.

Parameters	High-state	Low-state
γ_b	$4 \cdot 10^5$	$3 \cdot 10^5$
γ_{\max}	$1.2 \cdot 10^6$	$7 \cdot 10^5$
S_1	2.2	2.2
S_2	3.2	3.2
$B[G]$	0.1	0.1
$K[cm^{-3}]$	$1.6 \cdot 10^4$	$1.6 \cdot 10^5$
δ	15	15

Table 9. Best-fit parameters for high-state and low-state intensity when a one-zone synchrotron self-Compton model is fit to the spectrum.

4.5 Discussion and conclusions

The blazar Mrk 421 underwent an active phase in May/June 2006. INTEGRAL was therefore reoriented to observe this source for 12 days with the instruments OMC, JEM-X, and IBIS. Simultaneously the source was also observed by the Metsähovi and VLBA radiotelescopes, by the KVA telescope in the optical waveband, by RXTE and SWIFT at X-rays, and by Whipple at TeV energies. In X-rays, several strong flares were observed not seen at lower energies. Unfortunately the data at TeV energies are too sparse to allow such a conclusion for the high energies. In this context it is especially striking that the flares are not visible in the optical lightcurves, since it is thought that the X-rays and optical photons are produced by the same electron population via synchrotron emission. One would therefore expect similar lightcurves; but when fitting a theoretical one-zone synchrotron self-Compton model to the data, it is found that flares seen in X-rays may not necessarily be visible at lower frequencies.

However, other possibilities also exist for explaining the observed behaviour, rather than varying the efficiency of the acceleration. For example, it could be that the optical photons originate in larger emission regions and that the flares are thus occurring on longer time scales and are therefore smeared out. It could also be that the intensity fluctuations seen in X-ray are damped in the optical band. This view could be supported by the observed intensity correlation between OMC and IBIS in Figure 9. Whereas the IBIS rate varies by a factor of ~ 5 , the variation in the optical flux is only a few percent, so the high variations seen in X-rays are strongly damped in the optical range, hence barely visible. This could be achieved, for example, if the optical photons were obscured by some intervening clouds of matter that are transparent for the X-rays but not for the optical photons.

The spectral analysis of the JEM-X and IBIS/ISGRI data gave a surprising result: the spectral index α of the power law for the two states does not change much (from 2.12 to 2.3) at energies below 40 keV, although the intensity changes by factors up to 5. In the energy range 2-10 keV, Takahashi et al. (1996) found a clockwise evolution of the spectral index as a function of the intensity. But in their case the range of the change of the spectral index is nearly the same as reported by us (from 2.3 to 2.52), although the intensity only changes by a factor of 2. This shows that the observed slight hardening occurs predominantly at low intensities. This "saturation effect" is clearly seen in Figure 14.

Another remarkable result is that the hardness ratio of the Swift-XRT data is strongly varying with intensity (see Figure 15), whereas the hardness ratio of the IBIS/ISGRI data is more or less constant (see Figure 12). This again shows that there is a conspicuous difference in the emission processes of the low- and high-energy X-rays. At energies <10 keV, the spectrum becomes harder with increasing intensity. This is not the case for X-rays with energies >20 keV. In the standard model in which the X-rays are produced by synchrotron radiation from the same electron population, this different behaviour is difficult to explain.

The picture becomes even more complex when one compares the lightcurves of Figure 3 to Figure 6. The two flares at the end of the observation interval (around MJD 53910) show a noticeable spectral difference: the first peak is much harder than the second one! If one assumes that each flare is produced by a relativistically-moving blob of electrons, the physical characteristics of each electron population and their environment (i. e. magnetic fields etc.) must be different, so the picture of jet emission is very complex and the extraction of the relevant information from the data requires a detailed and profound modelling of the emission processes.

As can be seen from figure 17 and 18 we simulated the SED for both states of the source. The parameters of the results are shown in table 9. We simulated the SED for the blazar's active and quiescent state. The differences between the 2 datasets regard the parameter γ_{\max} and γ_{br} . During active state the SED is shifted to higher energy output and frequencies with respect to the low state. This is translated to higher values of γ_{\max} and γ_{br} in the simulation. The physical interpretation of the increased values of γ_{\max} and γ_{br} tells us that more electrons of the initial electron density are at higher energies. Thus, we can conclude that the simulation of our measured data confirm the emission scenario in a pure leptonic SSC-model framework, where the collision interaction of two outward moving blobs, change the number of emitting particles at different energies, resulting in a blazar outburst.

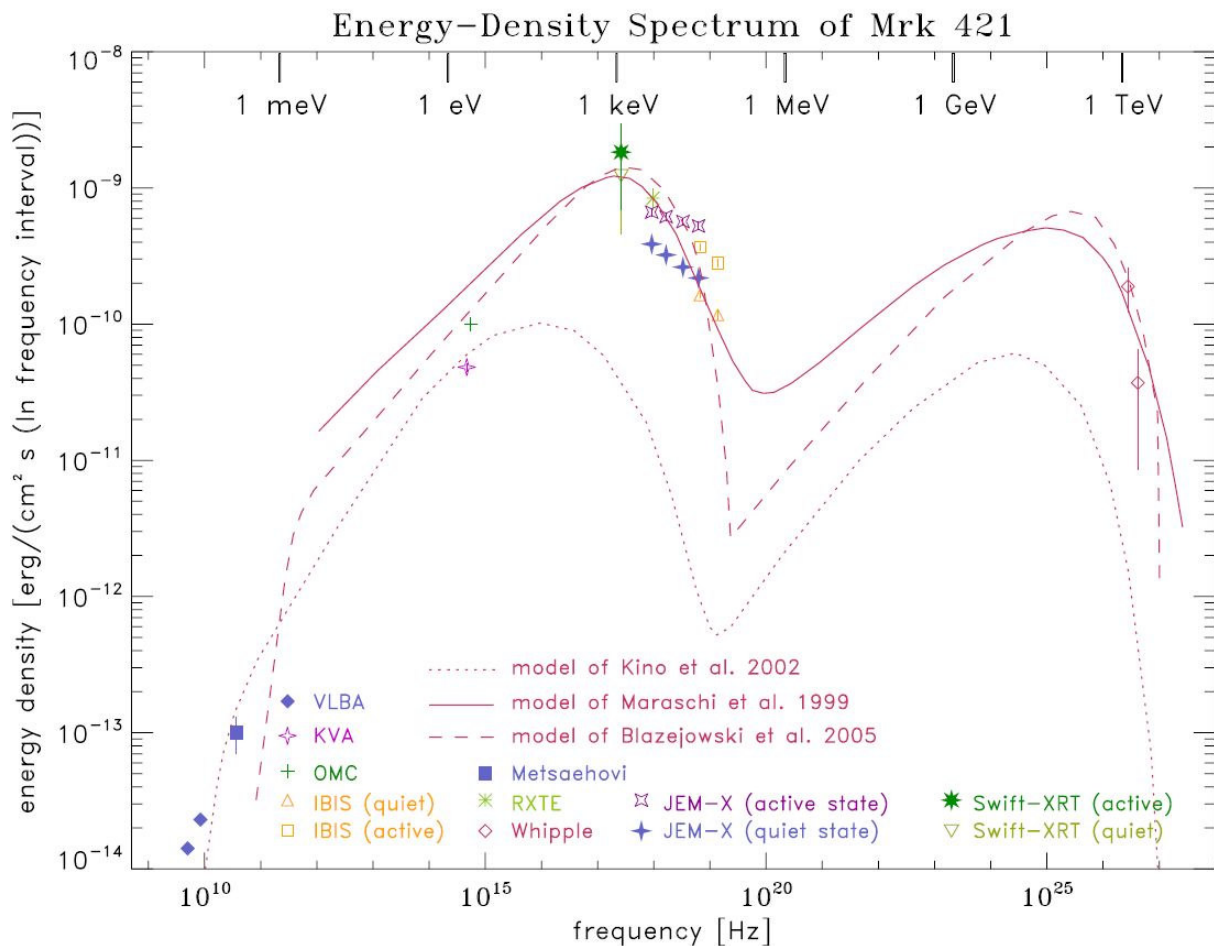


Figure 17. The measured energy-density spectrum of Mrk 421 is compared with the three theoretical models of Maraschi et al. (1999), Kino et al. (2002), and Blazejowski et al. (2005). Please note that the data and the three models represent the source in different states and therefore reflect its spectral variability.

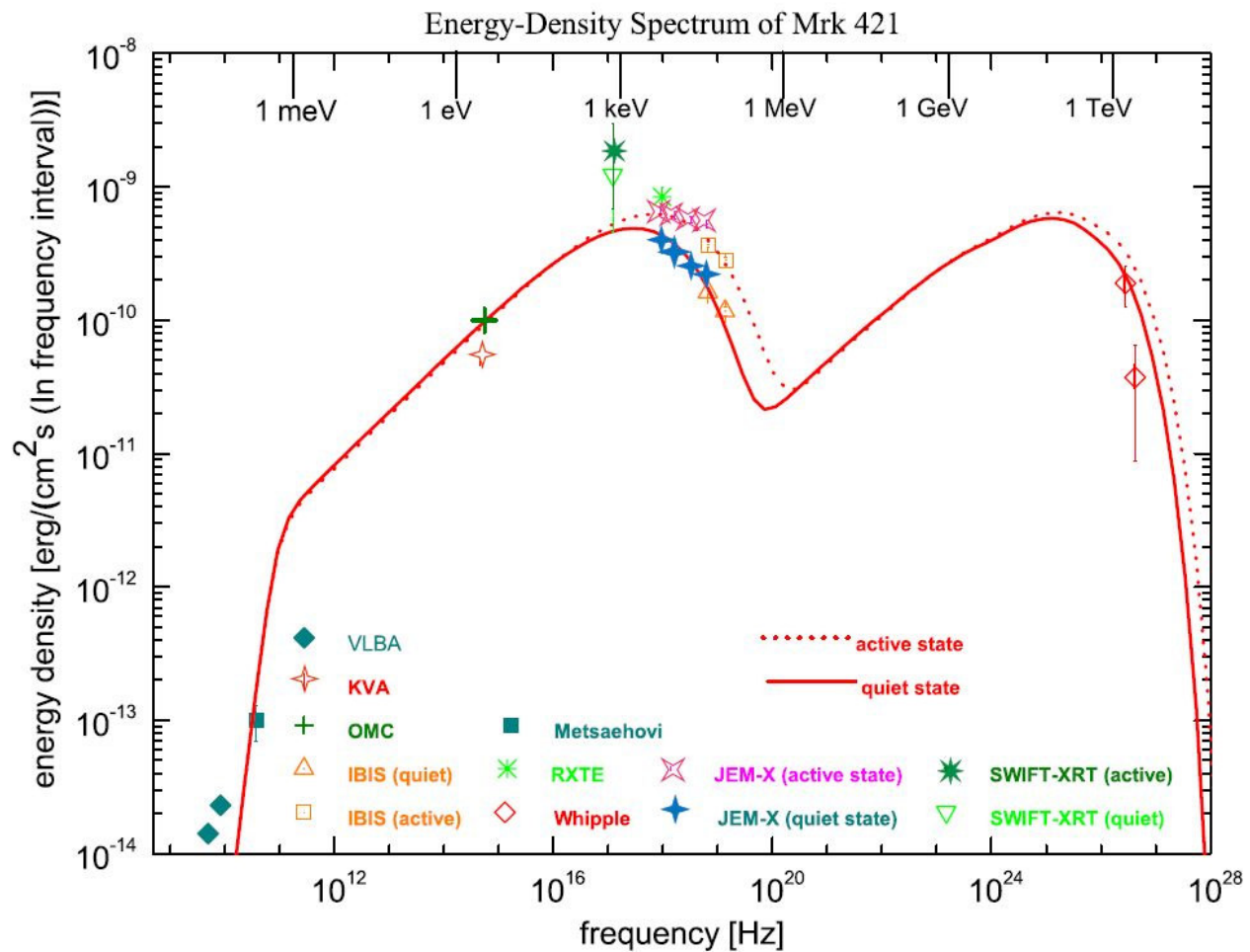


Figure 18: The result of the model fits to the measured energy-density spectrum of Mrk 421.

REFERENCES:

- Aharonian, F. A. et. al., 1999, A&A 350, 757
 Aharonian, F. A., 2000, New Astronomy 5, 377
 Aharonian, F. A. et al. 2002, A&A 393, 89

- Aharonian, F. A. et al. 2003, A&A 410, 813
- Aharonian, F. A. et al. 2005, A&A 437, 95
- Ajello, M., A. Rau, Greiner, J., Kanbach, A., Salvato, M., Strong, A. W.,
Barthelmy, S. D., Gehrels, N., Markwardt, C. B., and Tueller, J. 2008,
ApJ, 673, 96
- Barth A. J., Ho L. C., and Sargent W. L. W., 2003, Ap. J. 583, 134-144
- Barthelmy, S. D. et al. 2005 SSRv 120, 143
- Bessell, M. S. 1979, PASP 91, 589
- Blandford, R. D. and M. J. Rees 1978, in Pittsburgh Conference on BL Lac
Objects, ed. A. M. Wolfe, 328
- Blazejowski, M. et al. 2005, Ap. J. 630, 130
- Bloom, S. D. and A. P. Marscher 1996, Ap. J. 630, 130
- Blumenthal G. R., Gould R. J., 1970, Reviews of Modern Physics 42, 237
- Brinkmann, W. et al. 2005, A&A 443, 397
- Buckley, J. H. et al. 1996, Ap. J. 472, L9
- Burrows, D.N., Hill, J.E., Nousek, J.A., et al. 2005a, Space Sci. Rev., 120, 165
- Burstein, D. and C. Heiles 1982, A. J. 87, 1165
- Catanese, M. et al. 1997, Ap. J. 487, L143
- Charlot, P. et al. 2006, A&A 457, 455
- Chiapetti, L. et al. 1999, Ap. J. 521, 552
- Collmar, W. et al. 1999, Proc. of the 26th Int. Cosmic-Ray Conf. (Vol. 3), 374
- Cortina, J. et al. 2002, Proc. of the workshop "The Universe Viewed in Gamma
Rays", Frontier Science Ser. 39, 261
- Dermer, C. D. et al. 1992, Ap. J. 630, 130
- Edelson, R. A. and J. H. Krolik 1988, Ap. J. 333, 646
- Falomo R. et al. 2002, Ap. J. 569, L35
- Fossati, G. et al. 2000, Ap. J. 541, 153
- Fossati, G. et al. 2008, Ap. J. (in press) <http://fr.arxiv.org/abs/0710.4138>
- Gaidos, J. A. et al. 1996, Nature 383, 319
- Gehrels, N., Chincarini, G., Giommi, P., et al. 2004, Ap. J. 611, 1005
- Georganopoulos, M. & Kazanas, D. 2003, Ap. J. 594, L27

- Ghisellini, G. and L. Maraschi 1996, ASP Conf. Ser. 110, 436
- Ghisellini, G., L. Maraschi and L. Dondi 1996, A&A Suppl. Ser. 120, 503
- Ghisellini, G., Tavecchio, F. & Chiaberge, M. 2005, A&A 432, 401
- Giebels, B. et al. 2007, A&A 462, 29
- Hartman, R. C. et al. 1999, Ap. J. Suppl. Ser. 123, 79
- Henri, G. and L. Saugé 2006, Ap. J. 640, 185
- Hillas, A. M. et al., 1998 Ap. J. 503, 744
- Horan, D., et al. 2002, Ap. J. 571, 753
- Jones, F.C. et al. 1968, Phys. Rev. 167, 1159
- Kataoka, J. 2000, Ph. D. thesis of University of Tokyo
- Kataoka, J. et al. 2000, Ap.J. 528, 243
- Katarzynski, K. et al. 2003, A&A 410, 101
- Kazanas, D. et al. 1998, Ap. J. 493, 708
- Kerrick, A. D. et al. 1995, Ap. J. 438, L59
- Kildea, J. et al., 2007, Astropart. Phys. (in press) <http://dx.doi.org/10.1016/j.astropartphys.2007.05.004>
- Kino, M. et al. 2002, Ap. J. 564, 97
- Kirsch, M. G. F. et al. 2005, Proc. of the SPIE 5898 (ed. Oswald Siegmund), 22
- Königl, A. 1981, Ap. J. 243, 700
- Konopelko, A. et al. 2003, Ap. J. 597, 851
- Krawczynski, H. et al. 2001, Ap. J. 559, 187
- Krawczynski, H. et al. 2004, Ap. J. 601, 151
- Krennrich, F. et al. 2003, Proc. of the 28th Int. Cosmic-Ray Conf. (Vol. 5), 2603
- Krennrich, F. et al. 2001, Ap. J. 560, L45
- Levine, A. M. et al. 1996, Ap. J. 469, L33
- Lichti, G. G. et al. 2007, Proc. of the 1st GLAST Symposium, AIP 921, 371
- Mannheim, K. et al. 1993, A&A 269, 67
- Maraschi, L. et al. 1999, Ap. J. 526, L81
- Massaro, E. et al. 2004, A&A 413, 489
- Mastichiadis, A. and J. G. Kirk 1997, A&A 320, 19
- Mücke, A. and R. J. Protheroe 2000, Astroparticle Physics 15, 121

- Mücke, A. et al. 2003, *Astroparticle Physics* 18, 593
- Nilsson, K., Pasanen, M., Takalo, L. O., Lindfors, E., Berdyugin, A., Ciprini, S., and Pforr, J. 2007, *A&A* 475, 199
- Padovani, P. et al. 2007, *Proc. of the 1st GLAST Symp.* [arXiv: 0704.0184v (astro-ph)]
- Piner, B. G. and P. G. Edwards 2005, *Ap. J.* 622, 168
- Punch, M. et al. 1992, *Nature* 358, 477
- Ravasio, M., et al. 2004, *A&A* 424, 841
- Rebillot, P. F., H. M. Badran et al. 2006, *Ap. J.* 641, 740
- Rüger M., Spanier F., Mannheim K., 2008, in preparation
- Sambruna, R. M. et al. 2000, *Ap. J.* 538, 127
- Seaton, M. J. 1979, *MNRAS* 187, 73P
- Sembay, S. et al. 2002, *Ap. J.* 574, 634
- Sikora, M. et al. 1994, *Ap. J.* 421, 153
- Takahashi, T. et al. 1996, *Ap. J.* 470, L89
- Tal Alexander 2007, to be published
- Tavecchio, F., Maraschi, L. & Ghisellini, G. 1998, *Ap.J.* 509, 608
- Tavecchio F. et al. 2001, *Ap.J.* 554, 725
- Tavecchio, F. 2005, *Proc. of 10th Marcel Grossmann Meeting (MG10)*, ed. Novello, Perez-Bergliaffa, Ruffini, World Scientific 2005
- Teräsanta, H., Tornikoski, M., Mujunen, A. et al. 1998, *A&AS* 132, 305
- Treves A. et al. 2003, *ASP Conf. Ser.* 290, 621
- Ulrich, M.-H., L. Maraschi and C. M. Urry 1997, *ARA&A* 35, 445
- Vainio, R. and R. Schlickeiser 1998, *A&A* 331, 793
- Vainio, R. and F. Spanier 2005, *A&A* 437, 1
- Villata, M., Raiteri, C. M., Lanteri, L., Sobrito, G., and Cavallone, M. 1998, *A&AS* 130, 305
- Wagner R. <http://www.mppmu.mpg.de/~rwagner/sources/>
- Wamsteker, W. 1981, *A&A* 97, 329

Chapter 5

5 CONCLUSIONS

5.1 Conclusions and outlook

The INTEGRAL satellite with its instruments was designed aiming multiwavelength studies on pointed objects. According to this philosophy, I here present blazar multifrequency campaigns that were triggered by proposals, carried out with INTEGRAL, other satellites and ground base telescopes, and finally analyzed. But within the last INTEGRAL AOs, also deep pointings, having the aim to detect weak sources were approved. To this end, a proper background modeling of ISGRI imager on board INTEGRAL was studied and applied in order to gain better sensitivity.

Regarding this latter issue, in the first part of the thesis a proper data screening and data selection method were developed, allowing the data to be

inspected for goodness and consistency. Dedicated software was developed, using IDL programming language and providing a graphical user interface, which allows browsing for observations, retrieve the information for each SCWs (like the number of bad or dead pixels of the detector, image rms, etc.) and represent them graphically. Coded mask detectors, like ISGRI, are background dominated. The sensitivity determination of such experiments is based on several assumptions not always fulfilled (Skinner, 2008). Thus it is necessary to account for all possible detector effects contributing to the background. The ISGRI standard analysis software does a good job, however several artifacts can be seen in the obtained mosaic images and in the statistics derived from them. My background modeling avoids these problems leading to better image statistics and thus, a better sensitivity. Moreover the INTEGRAL pointing strategy leads to observations where the objects to be detected are known in advance. This effect is not easy to account for in surveys (Sazonov, S.; et al., 2007) and it also contributes in the detector as background. To this end I account also for this background component with a source-model contribution for each source. This overall sensitivity improvement will find its application in probing a highly-obscured source population (Worsley, M.A.; et al., 2005), contributing to the CXB peaking at 30 keV (Ajello, M.; et al., 2008). The number density of these sources is still unknown and the only way to understand their contribution to the CXB is to detect them. This will be done in the accepted INTEGRAL Key Program Proposal for the North Ecliptic Pole campaign which will be carried out for the next two years to come. The aim is to detect a large sample of faint sources (at $\sim 10^{-12}$ erg cm⁻² s⁻¹ sensitivity) and thus study the relation between highly-absorbed and un-absorbed sources. Furthermore, this method shows promising results where hard X-ray sources populate crowded fields like the Galactic plane. Our very good source removal algorithm together with ISGRI's characteristics (good angular resolution and long exposure on the Galactic plane) can give a unique contribution in identifying at hard X-rays the recently discovered and unidentified Galactic TeV source population (Aharonian, F.; et al., 2008). This sky region is of interest also for the recently found asymmetric distribution of positrons revealed by gamma-rays (Weidenspointer, G.; et al., 2008). This asymmetry resembles the one observed in the distribution of low mass X-ray binaries (LMXB) above 20 keV on the Galactic plane. Our method can give a significant contribution in order to confirm or reject the positron-LMXBs association.

INTEGRAL carries ideal instruments for multiwavelength campaigns. Indeed, in the second part of the thesis several multiwavelength campaigns are presented. Mrk 421 observations were performed, covering the spectrum from radio to TeV

energies. The synchrotron component was completely constrained by INTEGRAL's optical, X-ray and hard X-ray bands. The flaring activity allowed deriving several physical parameters. We have studied the jet activity in Mrk 421 through the variability at all wavelengths and compiling two SEDs respectively for the quiescent and active state. The comparison between both simulated SEDs showed an increase of the number of electrons of the initial electron density at higher energies during the active state. This confirms for Mrk 421 the internal shock scenario. The jet is ejected intermittently from the central engine. When a fast ejecta catches up a slower one, a shock is formed. This is where electrons are accelerated to, giving rise to the synchrotron and inverse-Compton radiation.

A slightly different variability was observed for the prominent gamma-ray blazar 3C 279. Simultaneous observations in optical and hard X-ray bands over several epochs in its quiescent state showed large variations in the former energy band despite a constant flux level at the latter one. Variability changes between 14.3 and 17.2 mag correspond to a flux changes of a factor 14.5. Even though time lags in variability studies of this source showed the synchrotron emission leading the inverse-Compton of the order of ~ 2.5 days (Hartman, R.C.; et al., 1999), the long integration time of INTEGRAL observations should avoid this effect. None of the two competing jet models (SSC and EC) can account for this behavior which is still escaping our understanding.

In the case of PKS 0537-286, a FSRQ at $z = 3.1$, just little variability was observed during the multifrequency campaigns carried out at five different epochs. I have submitted ToOs in order to perform this campaign. For the source, observed by several instruments on board Swift, INTEGRAL and RXTE, the soft X-ray absorption excess and a hard spectral index was confirmed according to the trend seen in a number of FSRQ studies at high redshift (Fiore, F.; et al., 1998) (Reeves & Turner, 2000). We explain this feature, also referred to as spectral flattening, in terms of bulk Comptonization by cold leptons within the jet and predicted by Celotti (Celotti, A.; et al., 2007). Due to the very good sampled spectra from 0.3 - 150 keV, I am able to fit, for the first time, a self consistent bulk Comptonization model (BMC) (Titarchuk, L. et al., 1997) to a blazar spectrum which is able to mimic the flattening towards longer wavelengths. Thus I can affirm that this emission model is at work in this FSRQ jet. Furthermore, I identified PKS 0537-286 as 3 EG J0531-2940 counterpart due to a viable emission model. This led to the best ever sampled simultaneous SED of the source which allowed the derivation of precise parameter through the simulations.

Extrapolating the EGRET Log N - Log S (Dermer C. , 2007), FSRQs like PKS 0537-286 and 3C 279 are predicted to dominate the AGN source population as will be seen by the recently launched FERMI mission. Thus, our precisely sampled X-ray and hard X-ray spectra anticipate the features that can be seen with FERMI multifrequency campaigns. Our results will contribute to the understanding of the jet emission mechanism for the overall class of blazars. Once these global properties of the blazar class are fully understood, the evolutionary properties of FSRQ and BL Lac sub-classes can be investigated. Indeed, there are hints that BL Lac objects could represent the final stage of the evolution of FSRQ. Boettcher and Dermer (Boettcher & Dermer, 2002) proposed that in BL Lacs all the material has already been accreted and no gas or dust are left for the external Compton-scattered component. These features are observed within the here presented studies. The apparent lack of evolution in BL Lacs (Padovani, P.; et al., 2007) confirms this evolutionary scenario. If so, FERMI will observe a decrease in number density of FSRQs at lower red-shift and a larger accretion rate for this latter sub-class of blazars with respect to BL Lacs.

6 BIBLIOGRAPHY

- Aharonian, F.; et al. (2007). Detection of extended very-high-energy γ -ray emission towards the young stellar cluster Westerlund 2. *A&A* , 567, 1075.
- Aharonian, F.; et al. (2005). Discovery of very high energy gamma rays associated with an X-ray binary. *Science* , 309, 746.
- Aharonian, F.; et al. (2008). HESS very-high-energy gamma-ray sources without identified counterparts. *A&A* , 477, 353.
- Ajello, M.; et al. (2008). Cosmic X-ray background and Earth albedo spectra with Swift/BAT. *astro-ph* , arXiv:0808.3377v1.
- Ajello, M.; et al. (2008). The Swift BAT X-Ray Survey. III. X-Ray spectra and statistical properties. *ApJ* , 673, 96.
- Albert, J.; et al. (2006). Variable very-high energy gamma-ray emission from the Microquasar LS I +61 303. *Science* , 312, 1771.
- Angel, J. (1979). The lobster-eye telescope. *ApJ* , 233, 264.
- Aschenbach, B. (1985). X-ray telescopes. *Rep. Proc. Phys.* , 48, 579.
- Baliyan, K. (2001). Multiwavelength study of the variability in blazars. *Bull.Astr.Soc. India* , 29, 397.
- Bennert, N. (2002). Size and Structure of the Narrow-Line Region of Quasars. *ApJ* , 574, L105.
- Blanch, O., & Martinez, M. (2005). Exploring the gamma-ray horizon with the next generation of gamma-ray telescopes. Part 2: Extracting cosmological parameters from the observation of gamma-ray sources. *Aph* , 23, 598.
- Blandford, R. D., & Payne, D. G. (1982). Hydromagnetic flows from accretion discs and the production of radio jets. *MNRAS* , 199, 883-903.
- Blandford, R. D., & Znajek, R. L. (1977). Electromagnetic extraction of energy from Kerr black Holes. *MNRAS* , 179, 433-456.
- Bloom, S. D., & Marscher, A. P. (1996). An analysis of the synchrotron self-Compton model for the multi-wave band spectra of Blazars. *ApJ* , 461, 657.
- Boettcher, M., & Dermer, C. (2002). An evolutionary scenario for blazar unification. *ApJ* , 564, 86.
- Bottacini, E., Beckmann, V., Ishibashi, W., Ajello, M., & Greiner, J. (2007). Blazar 1ES 1959+650 shows high and hard X-ray state. *The Astronomer's Telegram* , 1315.
- Caroli, E.; et al. (1987). Coded aperture imaging in X- and gamma-ray astronomy. *SSRv* , 45, 349.
- Celotti, A.; et al. (2007). Bulk Comptonization spectra in blazars. *MNRAS* , 375, 417.

- Chernyakova, M.; et al. (2006). INTEGRAL and XMM-Newton observations of LSI +61 303. *MNRAS* , 372, 1585.
- Cocconi, G. (1960). An Air Shower Telescope and the Detection of 10^{12} eV Photon Sources. *Proc. Moscow Cosmic Ray Conf. 2* (ed. V.I. Zatsepin, Moscow), (p. 309).
- Comastri, A. (2004). Compton-thick AGN: the dark side of the X-ray background. *Astr.Space Sci. Lib.* , 308, 245.
- Courvoisier, T.J.-L. et al. (2003). The INTEGRAL Science Data Centre (ISDC). *A&A* , 411, 53.
- Dempster, A.P.; et al. (1977). Maximum likelihood estimation from incomplete data via the EM algorithm. *J. Royal Stat. Soc.* , 39, 1.
- Dermer, C. D., Schlickeiser, R., & Mastichiadis, A. (1992). High-energy gamma radiation from extragalactic radio sources. *A&A* , 256, 27.
- Dermer, C. (2007). Statistics of cosmological black hole jet sources: blazar predictions for the Gamma-Ray Large Area Space Telescope. *ApJ* , 659, 975.
- Eckart, A., Genzel, R., & Schoedel, R. (2004). *PThPS* , 159, 155.
- Edge, D. (1959). A survey of radio sources at a frequency of 159 Mc/s. *Mem. R. Astron. Soc.*, 68 , 37-60.
- Efstathiou, A., & Rowan-Robinson, M. (1995). Dusty discs in active galactic nuclei. *MNRAS* , 273, 649-661.
- Fanaroff, B. a. (1974). The Morphology of Extragalactic Radio Sources of High and Low Luminosity. *MNRAS* , 167, 31.
- Fenimore, E., & Cannon, T. (1978). Coded aperture imaging with uniformly redundant arrays (ET). *Appl. Opt.* , 17, 337.
- Fiore, F.; et al. (1998). X-ray spectral survey of WGACAT quasars. I. Spectral evolution and low-energy cutoffs. *ApJ* , 492, 79.
- Forot, M.; et al. (2007). Compton telescope with a coded aperture mask: imaging with the INTEGRAL/IBIS compton mode. *ApJ* , 668, 1259.
- Fossati, G. et al. (1998). A unifying view of the spectral energy distribution of blazars. *MNRAS* , 299, 433.
- Funk, S.; et al. (2007). XMM-Newton observations reveal the X-ray counterpart of the very high energy gamma-ray source HESS J1640-465. *ApJ* , 662, 517.
- Gehrels, N. (1997). Use of νF_{ν} spectral energy distributions for multiwavelength astronomy. *Il nuovo cimento* , 112B, 11.
- Ghisellini, G. a. (2001). The dividing line between FR I and FR II radio galaxies. *A&A* , 379, L1.
- Ghisellini, G., & Madau, P. (1996). On the origin of gamma-ray emission in Blazars. *MNRAS* , 299, 433.

- Ghisellini, G., Celotti, A., Fossati, G., Maraschi, L., & Comastri, A. (1998). A theoretical unifying scheme for gamma-ray bright Blazars. *MNRAS* , 301, 451.
- Giacconi, R., Gursky, H., Paolini, F., & Rossi, B. B. (1962, December 1). Evidence for X-Rays From Source Outside the Solar System. *Physical Review Letters* , 9, pp. 439-443.
- Giacconi, R.; et al. (1969). Grazing-incidence telescopes for X-ray astronomy. *Space Science Reviews* , 9, 3.
- Giommi, F.; et al. (2007). ROXA J081009.9+384757.0: a 10^{47} erg s^{-1} blazar with hard X-ray synchrotron peak or a new type of radio loud AGN? *A&A* , 468, 97.
- Gopal-Kirshna and Wiita, P. (1988). The Ranaroff-Riley Transition and the Optical Luminosity of the Host Elliptical Galaxy. *Natur* , 33, 49.
- Hartman, R. C. (1999). The third EGRET Catalog of high-energy gamma ray sources. *ApJS* , 1213, 79.
- Hartman, R. C.;. (2001). Day-scale variability of 3C 279 and searches for correlations in gamma-ray, X-ray, and optical bands. *ApJ* , 558, 583.
- Hartman, R. C.;. (1992). Detection of high-energy gamma-ray radiation from quasar 3C 279 by the EGRET telescope on the Compton Gamma Ray Observatory. *ApJ* , 385, 1.
- Hartman, R.C.; et al. (1999). *ApJ* , 558, 583.
- Hermsen, W. (2007). A deep INTEGRAL observation of the peculiar radio/X-ray/gamma-ray/TeV source LS I + 61 303. *API Conf. Proc.* , 921.
- in 't Zand, J. (1994). The optimum open fraction of coded apertures. With application to the Wide Field X-Ray cameras of SAX. *A&A* , 665.
- Koenigl, A. (1981). Relativistic jets as X-ray and gamma-ray sources. *ApJ* , 243, 700.
- Krawczynski, H., Hughes, S. B., Horan, D., Aller, M. F., & Aller, H. (2004). Multiwavelength observations of strong flares from the TeV Blazar 1ES 1959+650. *ApJ* , 601, 151.
- Labanti, C.; Di Cocco, G.; Ferro, G.; et al. (2003). The Ibis-Picst detector onboard Integral. *A&A* , 411, 149.
- Laing, R. (1994). Decelerating relativistic jets in FRI radio sources. *ASPC* , 54, 227L.
- Lebrun, F.; Leray, J.P.; Lavocat, P.; et al. (2003). ISGRI: The INTEGRAL Soft Gamma Ray Imager. *A&A* , 411, 141.
- Lott, B., Carson, J., Ciprini, S., Dermer, C. D., Giommi, P., Madejski, G., et al. (2007). Studying gamma-ray Blazars with the GLAST-LAT. *AIP Conf. Proc.* , 921, 347.

- Lumsden, S. L., Heisler, C. A., Bailey, J. A., Hough, J. H., & Young, S. (2001). Spectropolarimetry of a complete infrared-selected sample of Seyfert 2. *MNRAS* , 327, 459-474.
- Lund, N.; et al. (2003). JEM-X: The X-ray monitor aboard INTEGRAL. *A&A* , 411, 23.
- Mannheim, K. (1993). The proton Blazar. *A&A* , 269, 67.
- Mas-Hesse, J.M.; Gimenez, A.; et al. (2003). OMC: An Optical Monitoring Camera for INTEGRAL. Instrument description and performance. *A&A* , 411, 26.
- Morrison, P. (1958). On Gamma-Ray Astronomy. *Il Nuovo Cimento* , 7, 858-66.
- Muecke, A., & Pohl, M. (2000). The contribution of unresolved radio-loud AGN to the extragalactic diffuse gamma-ray background. *MNRAS* , 312, 177.
- Padovani, P. (1997). Unified schemes for radio loud AGNs: recent results. *Memorie della Societa' Astronomia Italiana* , 68, 47.
- Padovani, P., & Giommi, P. (1995). The connection between X-ray- and radio-selected BL Lacertae Objects. *ApJ* , 444, 567.
- Padovani, P., & Urry, C. (1992). Luminosity functions, relativistic beaming, and Unified theories of High-Luminosity Radio Sources. *ApJ* , 387, 449.
- Padovani, P., Costamanete, L., Ghisellini, G., Giommi, P., Perlman, & E. (2002). BeppoSAX observations of synchrotron X-ray emission from radio Quasars. *ApJ* , 581, 895.
- Padovani, P., Perlman, E. S., & Landt, H. (2003). What types of jets does Nature make? A new population of radio Quasars. *ApJ* , 588, 128.
- Padovani, P.; et al. (2007). The deep X-ray radio blazar survey. III. Radio number counts, evolutionary properties, and luminosity function of blazars. *ApJ* , 662, 182.
- Pian, E. (2002). X-ray variability of Blazars. *PASA* , 19, 49.
- Piner, B. G., & Edwards, P. G. (2005). VLBA polarization observation of Markarian 421 after a gamma-ray high state. *ApJ* , 622, 168.
- Rau, A.; Kienlin, A. V.; et al. (2005). The 1 st INTEGRAL SPI-ACS gamma-ray burst catalogue. *A&A* , 438, 1175.
- Rees, M. (1966). Appearance of relativistically expanding radio sources. *Nature* , 211, 468.
- Reeves, J., & Turner, M. (2000). X-ray spectra of a large sample of quasars with ASCA. *MNRAS* , 316, 234.
- Reimer, A. (2007). The Redshift Dependence of Gamma-Ray Absorption in the Environments of Strong-Line AGNs. *ApJ* , 665, 1023.
- Risaliti, G.; et al. (1999). The distribution of absorbing column densities among Seyfert 2 galaxies. *ApJ* , 522, 157.

- Sazonov, S.; et al. (2007). Hard X-ray luminosity function and absorption distribution of nearby AGN: INTEGRAL all-sky survey. *A&A* , 462, 57.
- Schmidt, M. (1963). A Star-Like Object with a larg Redshift. *Nature* , 1040, 197.
- Schmitt, J. H. (1991). A soft x-ray image of the moon. *Nature* , 349, 583-587.
- Seyfert, C. K. (1943). Nuclear Emission in Spiral Nebulea. *ApJ* , 28, 97.
- Shields, G. A. (1999). A Brief History of AGN. *PASP* , 111, 611S.
- Skinner, G. (2004). Coded mask imagers when to use them - and when not. *New Astronomy Reviews* , 48, 205.
- Skinner, G. (2008). The sensitivity of coded mask telescopes. *arXiv0804.10895* .
- Skinner, G., & Ponman, T. (1994). On the propertiess of images from coded-mask telescopes. *MNRAS* , 267, 518.
- Stecker, F. W. (2006). Intergalactic photon spectra from the far-IR to the UV Lyman limit for $0 < z < 6$ and the optical depth of the Universe to high-energy gamma-rays. *ApJ* , 648, 774.
- Titarchuk, L. et al. (1997). X-Ray Spectral Formation in a Converging Fluid Flow: Spherical Accretion into Black Holes. *ApJ* , 487, 834.
- Turriziani, S.; et al. (2007). ROXA: a new multirequency large sample of blazars selected with SDSS and 2dF optical spectroscopy. *A&A* , 472, 699.
- Ubertini, P.; Lebrun, F.; Di Cocco, G.; et al. (2003). IBIS: The Imager on-board INTEGRAL. *A&A* , 411, 131.
- Urry, C. M. (1998). BL Lac objects and Blazars: past, present and future. *ASP* , 3.
- Urry, C., & Padovani, P. (1995). Unified Schemes for Radio-Loud Acrive Galactic Nuclei. *PASO* , 107, 803.
- Vassilie, V. V. (1999). Extragalactic backgorund light absorption signal in the TeV-ray spectra of Blazars. *astro-ph/9908088* .
- Vedrenne, G.; Roques, J.-P.; Schoenfelder, V.; et al. (2003). SPI: The spectrometer aboard INTEGRAL. *A&A* , 411, 63.
- von Montigny, C. (1995). High-energy gamma-ray emission from active galaxies: EGRET observations and their implications. *ApJ* , 440, 525.
- Weidenspointer, G.; et al. (2008). An asymmetric distribution of positrions in the Galactic disk revealed by gamma-rays. *Nature* , 451, 159.
- Winkler, C.; Courvoisier, T.J.-L.; Di Cocco, G.; Gehrels, N.; et al. (2003). The INTEGRAL mission. *A&A* , 411, 1.
- Wold, M. e. (2000). Clustering of Galaxies around Radio Quasars at $0.5 < z < 0.8$. *MNRAS* , 316, 267.

- Worsley, M.A.; et al. (2005). The unresolved hard X-ray background: the missing source population implied by the Chandra and XMM-Newton deep fields. *MNRAS* , 357, 1281.
- Wurtz, R. (1996). The Canada-France-Hawaii Telescope Imaging Survey of BL Lacertae Objects. I. Properties of the Host Galaxies. *ApJS* , 103, 109.

Acknowledgements

Without the help of the whole gamma group this work would not have been possible.

I'm grateful to my supervisor Jochen Greiner who supported the independent research and pushed me to write proposals. I thank Giselher Lichti who always was ready for any type of questions and support. Thank you to Werner Collmar for having made possible this PhD.

I acknowledge the suggestions received from Mara Salvato and I thank Arne Rau for conscientiously reading the proposals.

Thanks to Sandra Savaglio for the "small tools" for the great conversion problems.

Special thanks to Betta, Nico and Elena for their friendship.

I am also grateful to Marco Ajello for the time spent together, for all his research ideas and the long discussions on coded masks. Grazie Ciccio!

I cite here also my sister Renata who "concretely" supported my work and took care of what I left home.